INTERSEISMIC BEHAVIOR ALONG THE NORTH ANATOLIAN FAULT IN THE MARMARA REGION USING 3D STRUCTURE

by

Zeynep Yılmaz

B.S., Geophysical Engineering, İstanbul University, 2008

M.S., Geophysics, Boğaziçi University, 2013

Submitted to the Kandilli Observatory and
Earthquake Research Institute in partial fulfillment of
the requirements for the degree of
Doctor of Philosophy

Graduate Program in Geophysics

Boğaziçi University

2022

Dedicated to

my beloved mother Gülseren Yılmaz

ACKNOWLEDGEMENTS

First of all, I would like to express my sincere gratitude to my thesis supervisor, Associate Professor Ali Özgün Konca, for his academic support and guidance throughout these years. As my thesis supervisor, he was always eager to provide keen scientific insights and excellent suggestions. I feel fortunate to have a chance to work with him on my Ph.D. thesis research.

I would like to express my gratitude to the members of my thesis committee, Professor Mehmet Sinan Özeren and Associate Professor Çağrı Diner, for their constructive comments and for sharing their invaluable insights. I would like to thank Professor Semih Ergintav, who gave me invaluable suggestions about my thesis and was on my thesis committee. I also would like to thank my committee member, Assistant Professor Gülsen Uçarkuş, for her time and consideration.

I am truly indebted to Yasin Türk for his generous IT support and patience during the numerical calculations of this study.

I would like to thank Professor Nurcan Meral Özel for her support and contributions. I would also like to thank Professor Hayrullah Karabulut, Professor Cemil Gürbüz, and Professor Mustafa Aktar, as I have learned a lot from their lectures. I would also like to thank all my colleagues and the faculty members in the Department of Geophysics who supported me. I thank Metin Zobu, Uğur Mustafa Teoman, Öcal Necmioğlu, Didem Samut Cambaz, and Ayşegül Köseoğlu for their encouragement. I would like to thank Boğaziçi University Research Fund for their financial support with Grant Number 15022.

I would like to express my eternal gratitude to my family: my dear mother Gülseren Yılmaz, my father Ali Yılmaz, and my brothers Engin Yılmaz and Adnan Yılmaz. I would like to thank my dearest friend Nilay Başarır Baştürk, and my cousins, Selin Koca, Semih Sakarya and Burak Sakarya, who always provided me with their moral support and friendship. My other special thanks are to my dear friends Gülten Polat, Yasemin Korkusuz Öztürk, Fatma Ekiz Sonay, Fatma Sinem Çakır, Hale Kaplan and Servet Yılmaz.

ABSTRACT

INTERSEISMIC BEHAVIOR ALONG THE NORTH ANATOLIAN FAULT IN THE MARMARA REGION USING 3D STRUCTURE

A series of earthquakes occurred along the North Anatolian Fault (NAF) during the 20th century, primarily migrating from east to west. The only part of the NAF that has not broken is under the Marmara Sea. The Main Marmara Fault (MMF), the NAF's northern branch, is the most active one, with the highest slip rate amongst the several branches of the NAF. Since the seismic gap of ~150 km is beneath the sea, the geodetic data is not sufficient to constrain the full fault coupling, particularly in the Central Marmara. Nevertheless, the current data does imply that the GNSS vectors along the northern coast of the Marmara Sea are smaller than expected. One interpretation is that the MMF has heterogeneous interseismic coupling with creeping and locked segments. Another explanation is that the fault is locked, but the strain is asymmetrically localized around the MMF as a result of the deep basins. In this study, the competing effects of weak interseismic locking of the MMF and deep basins around the fault are studied by developing a 3-D finite element model for the Marmara Region, which includes a realistic topography, the 3-D geometry of the main fault, and basins, and using the geodetic data as a constraint. Our findings show that the deep basins confine the interseismic strain in the fault vicinity, and using a homogeneous half-space model leads to a slight underestimation of the locking depth. Our 3-D model shows that while the basins have some effects on strain localization, the heterogeneity of interseismic coupling is necessary to explain the observed GNSS data. We infer a change in the locking depth at the Ganos Bend between the strongly coupled Ganos and the weakly coupled Western Marmara. Seismic studies also indicate that these two segments vary considerably in background seismicity. The 50 km creeping segment coincides well with repeating earthquakes and higher rates of diffuse seismicity. Variations in regional stresses and earthquake focal mechanisms, including the 2019 Silivri earthquake sequence, are compatible with the dilatational quadrants in the region due to the loading caused by the interseismic creep of the Western Marmara.

ÖZET

3 BOYUTLU YAPI KULLANILARAK KUZEY ANADOLU FAYI'NIN MARMARA BÖLGESİ'NDEKİ İNTERSİSMİK DAVRANIŞININ İNCELENMESİ

20. yüzyılda Kuzey Anadolu Fayı (KAF) boyunca, çoğunlukla doğudan batıya göç eden bir dizi deprem meydana gelmiştir. KAF'ın kırılmayan tek bölümü Marmara Denizi'nin altındaki kısmıdır. KAF'ın kuzey kolu olan Ana Marmara Fayı (AMF), KAF'ın çeşitli kolları arasında en yüksek kayma oranına sahip en aktif koludur. ~150 km'lik sismik boşluk denizin altında olduğundan, jeodezik veriler, fay kilitlenme oranını anlamada özellikle Orta Marmara'da yetersizdir. Yine de mevcut veriler Marmara Denizi'nin kuzey kıyısı boyunca GNSS verilerinin beklenenden küçük olduğunu göstermiştir. Bir yorumlama, AMF'nin krip eden ve kilitli segmentlerle heterojen bir intersismik kilitlenmeye sahip olduğu yönündedir. Diğer yorumlama ise, fayın kilitli olduğu, ancak gerilmenin derin basenlerin bir sonucu olarak AMF çevresinde asimetrik olarak lokalize olduğu yönündedir. Bu çalışmada, Marmara Bölgesi'nin gerçekçi bir topoğrafyasını, ana fay ve basenlerin 3-B geometrisini içeren 3-B bir sonlu eleman modeli geliştirilerek ve jeodezik veri kullanarak, AMF'nin zayıf intersismik kilitlenmesi ve fay çevresindeki derin basen etkileri incelenmiştir. Bulgularımız, derin basenlerin intersismik gerilimi fay civarında sınırladığını ve homojen yarı-uzay model kullanılmasının, kilitleme derinliğinde daha sığ bir kilitlenme değerlendirmesine yol açtığını göstermiştir. 3-B modelimiz, basenlerin gerinim lokalizasyonu üzerinde bazı etkileri olsa da, GNSS verisini açıklamada intersismik kilitlenme heterojenliğinin gerekli olduğunu göstermiştir. Kuvvetli eşleşmiş Ganos ve zayıf eşleşmiş Batı Marmara arasında Ganos Bükümünde kilitleme derinliğinde bir farklılık olduğu görülmüştür. Sismik çalışmalar da, bu iki segmentin depremselliğinde önemli ölçüde farklılık olduğunu göstermektedir. 50 km'lik krip segmenti, tekrarlayan depremler ve daha büyük yaygın depremsellik oranı ile iyi bir şekilde örtüşmektedir. 2019 Silivri deprem serisi dahil bölgesel gerilme ve odak mekanizma değişimleri, Batı Marmara intersismik kripinin yüklemesiyle oluşan bölgedeki dilatasyon kadranları ile de uyumludur.

TABLE OF CONTENTS

ACKNOWLEDGEMENTS iv

ABSTRACT v

ÖZET vi

TABLE OF CONTENTS vii

LIST OF FIGURES ix

LIST OF TABLES xv

LIST OF SYMBOLS xvii

LIST OF ACRONYMS/ABBREVIATIONS xix

1. INTRODUCTION 1

1.1. The Structure of the Thesis 2

2. TECTONICS OF TURKEY AND THE MARMARA REGION 4

2.1. Tectonics of Turkey 4

2.2. The Geometry of the Main Marmara Fault 5

2.3. Studies of Fault Behavior Using Geodetic Data 9

2.4. Studies of Seismicity and Repeating Earthquakes Along the MMF 11

2.5. Historical Earthquake Studies 12

3. GOVERNING EQUATIONS FOR DEFORMATION ANALYSIS 14

3.1. The Derivation of the Elasticity Equation in Index Notation 14

3.2. Governing Equations for Linear Elastic Materials 16

4. THE FINITE ELEMENT METHOD 19

4.1. Advantages of the Finite Element Method 20

4.2. Derivation of the Elasticity Equation with Finite Element Formulation in Index Notation 21

5. APPLICATION OF FINITE ELEMENT MODELING TO THE MARMARA REGION 26
5.1. Faults as Dislocation Sources 26
5.2. Interseismic Locking Behavior of the MMF in the Marmara Region 29
5.3. Data Set 30
5.4. 3-D Marmara Model Setup and Method 31
5.5. Fault Slip Rates and Boundary Conditions of the Model Domain 34
5.6. The Elastic Properties of the Model Domain 36
5.7. The Measure of the Misfit 37
6. FORWARD MODELING RESULTS FOR MARMARA GROUND DEFORMATION 39
6.1. A Constant Locking Depth Grid Search for the Main Marmara Fault 39
6.2. Models with Varying Locking Depths and the Best-Fitting Model 40
6.3. The Effect of the Sedimentary Basins and Fault Coupling on the Strain Rate Distribution 50
6.4. A Comparison of Different Proposed Elastic Properties and Interseismic Locking Depths with the Best-Fitting Interseismic Model 53
7. DISCUSSION 57
7.1. Interseismic Behavior and Structural Heterogeneity Along the Main Marmara Fault 57
7.2. Interseismic Coupling, Distribution of Seismicity, and Repeating Earthquakes along the MMF 59
7.3. Interseismic Behavior and Focal Mechanisms Along the MMF 60
8. CONCLUSIONS 65
REFERENCES 67
APPENDIX A: LIST OF GNSS STATIONS 80
APPENDIX B: LIST OF GNSS STATIONS USED IN PROFILES 84
APPENDIX C: A COMPARISON OF χ_r^2 MISFITS 85

LIST OF FIGURES

Figure 2.1. Anatolia plate tectonics, with black arrows and green arrowheads showing GNSS velocities of Reilinger *et al*. (2006) relative to Eurasia and light orange lines showing plate boundaries (Bird, 2003) of the EAFZ, NAFZ, etc. The same color represents right-lateral offsets and earthquake surface ruptures along the NAF since 1939 (Barka *et al*., 2002; Emre *et al*., 2013; Hori *et al*., 2017; Stein *et al*., 1997). The red frame indicates the study area. The red circles represent the M > 6 earthquakes from 1900 reported by the USGS.....5

Figure 2.2 . NAF branches in Western Turkey, as well as earthquake surface ruptures along the NAF (Armijo *et al*., 2002; Emre *et al*., 2013; Uçarkuş *et al*., 2011) and Marmara study area (red frame).....6

Figure 2.3. (a) Seismicity distribution including the 2007-2015 M≥2 seismic events (black circles with white fillings; Schmittbuhl *et al*., 2016b), the 2019 Silivri earthquake series (purple circles; Karabulut *et al*., 2021) and clusters of repeating earthquakes (red circles; Schmittbuhl *et al*., 2016a; Uchida *et al*., 2019), as well as two hydroacoustic arrays (black triangles; Lange *et al*., 2019; Sakic *et al*.,2016; Yamamoto *et al*., 2019) and GNSS velocities (black vectors with white arrowheads; Ergintav *et al*., 2014). MMF's geometrical bends are also shown. The surface trace is shown by a light orange line, while the 5 km distance contours are shown by black dashed lines. (b) A cross-section taken from the seismicity distribution shown in a) using the identical colors. The locking distribution of MMF suggested by Schmittbuhl *et al*. (2016b) is shown by a blue curve. 8

Figure 4.1. Illustrations of hexagonal and tetrahedral FEM meshes. 20

Figure 4.2. Schematic of a fault surface with continuous traction and a jump in displacement due to fault slip, adapted from Aagaard *et al*. (2013). 23

Figure 5.1. Schematic diagram of the contact surface of a real surface where the dotted areas show the real contact area, i.e., the asperity contact (A_r) within an apparent contact surface (A). (b) An illustration of a fault with heterogeneous locking behavior. 27

Figure 5.2. A schematic representation of a finite element model for a locked fault and a freely sliding unlocked fault below. 29

Figure 5.3. (a) A 3-D model of the Marmara made with real topography-bathymetry from Olson *et al*. (2014) separated by the MMF. The layers of the 3-D model are made up of blocks of sediment, the upper and lower crusts, and the mantle. (b) Model boundaries and the base of the sedimentary layer. (c) The MMF fault surface with slip rates comprising east-west lettered 6 segments. 32

Figure 5.4. A comparison between the blue vectors of the model with 18 million elements and the orange vectors of the model with 22 million elements. All vectors are computed at GNSS stations from the models with a 10 km fixed locking depth in a homogeneous medium. 33

Figure 5.5. Bottom boundary conditions represented with orange vectors and side boundary conditions with blue vectors interpolated from Eurasia fixed GNSS data (Ergintav *et al*., 2014) shown with black vectors. 34

Figure 5.6. Fault slip sign conventions of PyLith, where left-lateral, reverse, and fault-opening movements have positive values. 35

Figure 6.1. Model estimations at GNSS sites for fixed locking depths between 0 and 20 km in an elastic homogeneous medium, tested against GNSS velocities for (a) over the whole Marmara, (b) Central Marmara (the zoom-in on the green frame in (a)), and (c) Western Marmara (the zoom-in on the brown frame in (a)). 41

Figure 6.2. Model estimations at GNSS sites for fixed locking depths between 0 and 20 km in an elastic 3-D heterogeneous medium, tested against GNSS velocities for (a) over the whole Marmara, (b) Central Marmara (the zoom-in on the

navy frame in (a)), and (c) Western Marmara (the zoom-in on the purple frame in (a)).....42

Figure 6.3. (a) Observed GNSS velocities shown by black arrows, profile boundaries indicated in a variety of colors for each segment, and GNSS stations that are in these profile zones, which are also listed in Table B.1 in Appendix B. (b) Fault-parallel GNSS velocities shown as black circles with error bars and model estimates along the profiles shown as solid lines for locking depths between 0 and 20 km in a homogeneous elastic medium and (c) in a 3-D heterogeneous elastic medium. (d) The weighted RMS misfits calculated within each profile zone using Equation (5.1), shown with the identical profile colors in (a) employing locking depths using a grid space of 2.5 km in a homogeneous structure and (d) in a 3-D heterogeneous structure. 43

Figure 6.4. (a) Histogram distribution of χ_r^2 misfits from the locking depth grid search for the Marmara Sea segments B to E in Figure 5.3c based on 21 GNSS sites near the MMF. (b) The distribution of locking depths for 27 accepted $\chi_r^2 \leq 5.1$ models, represented by bars of the same color as the relevant segments, and the best-fitting locking depth for each section, shown by a thick navy line. 44

Figure 6.5. Optimization for the transition location between the fully creeping section E of the Western Marmara segment and the fully locked, extending down to a depth of 7.5 km, section F of the Ganos segment by comparing GNSS velocities displayed as black arrows against model estimates at neighboring GNSS stations, with the arrows of the same color as the relevant transition points, and the best-fitting transition point shown by a bigger cyan circle. The $M \geq 2$ earthquake epicenters (Schmittbuhl *et al*., 2016b) are shown with purple circles. The black lines are the fault lines (Emre *et al*., 2013), whereas the bold black line is our model's MMF surface trace. 46

Figure 6.6. The 3-D Marmara Region model and MMF, along with the best-fitting locking depth distribution and interseismic slip rates. In our 3-D heterogeneous best-fitting model, the locked parts of the fault are shown in black, while the white lines show the base of the shallower locking depth

estimations made with a homogeneous model. The pink line is where the bottom layer of sediments cuts through the MMF. Seismicity located within 5 km of the MMF is shown as purple circles (Schmittbuhl *et al*., 2016b), the 2019 Silivri earthquake series as green circles (Karabulut *et al*., 2021), and repeating earthquakes as cyan circles (Schmittbuhl *et al*., 2016a; Uchida *et al*., 2019). 47

Figure 6.7. (a) Observed GNSS velocities (black arrows with error ellipses of 95%) in comparison to estimates made in heterogeneous media with the HT_S_VB best-fitting model (red arrows), HT_S_C10 fixed to a 10 km locking depth model (green arrows), and HT_S_C15 fixed to a 15 km locking depth model (blue arrows). The error ellipses in purple represent continuous stations with uncertainties multiplied by a factor of 2.5, while the error ellipse in orange represents a station with uncertainties multiplied by a factor of 5.....48

Figure 6.8. Zoom-in on the İstanbul region (a) observed GNSS velocities (black arrows with error ellipses of 95%) in comparison to estimates made in heterogeneous media with the HT_S_VB best-fitting model (red arrows), HT_S_C10 fixed to a 10 km locking depth model (green arrows), and HT_S_C15 fixed to a 15 km locking depth model (blue arrows). The error ellipses in purple represent continuous stations with uncertainties multiplied by a factor of 2.5, while the error ellipse in orange represents a station with uncertainties multiplied by a factor of 5. (b) Residuals calculated by subtracting model estimates made with best-fitting locking (red), fixed at a 10 km locking (green), and a 15 km locking (blue) from GNSS velocities shown with 1-σ error ellipses. 49

Figure 6.9. Ground surface maximum shear strain rate fields for (a) a homogeneous model with a fixed locking depth of 10 km (HM_C10), (b) a heterogeneous model with a fixed locking depth of 10 km (HT_S_C10), and (c) the heterogeneous best-fitting model (HT_S_VB). 51

Figure 6.10. The ground surface velocities for the 3-D heterogeneous model with (a) the best-fitting locking depth (HT_S_VB) and (b) a fixed locking depth of 10 km (HT_S_C10). The colors and vectors show the magnitudes and

directions, respectively. (c) The differences between these two models, HT_S_VB and HT_S_C10, with a saturation rate of 5 mm/yr. 52

Figure 6.11. Geodetic misfits based on 21 GNSS sites near the MMF for the models (a) with different elastic properties of materials and locking depths and (b) with different sedimentary layer material properties (for model descriptions see Table 6.1). 54

Figure 6.12. Geodetic misfits based on all 76 GNSS sites in the Marmara region for models (a) with different elastic properties of materials and locking depths and (b) with different sedimentary layer material properties (for model descriptions see Table 6.1). 56

Figure 7.1. Ground surface dilatation rate fields for (a) a homogeneous model with a fixed locking depth of 10 km (HM_C10), (b) a heterogeneous model with a fixed locking depth of 10 km (HT_S_C10), and (c) the heterogeneous best-fitting model (HT_S_VB). Dark gray focal mechanisms indicate off-fault $M_w > 2.5$ earthquakes, whereas black ones suggest double-couple moment tensors that are best fitted for each region. Each zone's principal stress directions are also displayed. 63

Figure 7.2. Dilatation rate fields for the 3-D heterogeneous best-fitting elastic model (HT_S_VB) at (a) 5 km and (b) 10 km depths..... 64

Figure C.1. (a) Histogram distribution of χ_r^2 misfits from the locking depth grid search for the Marmara Sea segments B to E in Figure 5.3c based on all 76 GNSS sites in the Marmara region with covariance matrices multiplied by 2.45 for continuous ones. (b) The distribution of locking depths for 29 accepted $\chi_r^2 \leq$ 5.5 models, represented by bars of the same color as the relevant segments, and the best-fitting locking depth for each section, shown by a thick navy line. 90

Figure C.2. (a) Histogram distribution of χ_r^2 misfits from the locking depth grid search for the Marmara Sea segments B to E in Figure 5.3c based on all 76 GNSS sites in the Marmara region. (b) The distribution of locking depths for 29

accepted $\chi_r^2 \leq 20$ models, represented by bars of the same color as the relevant segments, and the best-fitting locking depth for each section, shown by a thick navy line. 91

LIST OF TABLES

Table 5.1. The coordinates of the ground surface vertices used for the 3-D Marmara model. 31

Table 5.2. MMF segment slip rates and boundary locations employed for this study. .. 35

Table 5.3. The elastic properties of the materials employed in the homogeneous model and heterogeneous model layers (Bassin *et al*., 2000; Hergert *et al*., 2011; Rodriguez-Suarez, 2005). 36

Table 6.1. Tested models named based on material compositions and locking depths (Yılmaz *et al*., 2022). 53

Table 7.1. Principal stress axes for each Marmara seismotectonic zone obtained by stress inversion of the M > 2.5 earthquake focal mechanisms. 61

Table A.1. Initial dataset of GNSS stations within the study area (Ergintav *et al*., 2014), where t_1 and t_2 denote the first and end data usage periods, F denotes the survey or continuous site with horizontal velocities, 1−σ uncertainties, and correlation coefficients. 80

Table B.1. GNSS stations used in the profiles of the 6 MMF segments. 84

Table C.1. The comparison of χ_r^2 misfits from the 0, 5 and 10 km locking depth grid search for the Marmara Sea segments B to E in Figure 5.3c using all available 76 GNSS sites with the modified covariance matrices ($\chi_r^2{}_1$), originally reported covariance matrices ($\chi_r^2{}_2$) and using 21 GNSS close to the MMF with the modified covariance matrices ($\chi_r^2{}_3$). 85

Table C.2. The comparison of χ_r^2 misfits for the 7 best models from the grid search of locking depths of Marmara Sea segments B to E in Figure 5.3c and 36 additional models with a 2.5 km grid size for segments C to E around the best-fitting models using all available 76 GNSS stations with the modified covariance matrices ($\chi_r^2{}_1$), originally reported covariance matrices ($\chi_r^2{}_2$) and

using 21 GNSS close to the MMF with the modified covariance matrices ($\chi_r^2{}_3$). 88

LIST OF SYMBOLS

A	Apparent Contact Surface
A_r	Asperity Contact
c	Continuous Site
C_d	Data Covariance Matrix
C_{ijkl}	4th Order Elastic Tensor
CX	X-km Constant Locking Depth Model
d^i	Horizontal Velocity Data at the ith Station
d_i	Fault Slip Vector Field
$d_P{}^i$	Fault-parallel Velocity Data at the ith Station
e	East Component
E_{RMS}	Weighted Root Mean Square Misfit
f_i	Body Force Vector Field
F	Site Type
M	Magnitude
M_w	Moment Magnitude
n	North Component
n_i	Normal Vector Field
nsta	Number of Stations
R_{ki}	Coordinate Transformation Rotation Matrix
s	Survey Site
S	Surface
t_1	First Epoch of Data Usage
t_2	Last Epoch of Data Usage
T_D	Rise Time
T_i	Traction Vector Field
u_i	Displacement Vector Field
V_E	East Component of Horizontal Velocity
V_N	North Component of Horizontal Velocity
V_P	Primary Wave Velocity
V_R	Rupture Velocity

V_S	Secondary Wave Velocity
δ	Kronecker Delta
ε_{ij}	Strain Tensor Field
E	Young's Modulus
λ	Lame's First Parameter
μ	Rigidity (Shear Modulus)
ν	Poisson's Ratio
σ_{ij}	Stress Tensor Field
σ_E	East Component of One-sigma Uncertainty
σ_N	North Component of One-sigma Uncertainty
σ_P^i	Fault-parallel 1-σ Data Uncertainty at the ith Station
χ_r^2	Chi Squared Error
p^i	Predicted Horizontal Velocity at the ith Station
p_i	Mass Density Scalar Field
p_P^i	Fault-parallel Model Predictions at the ith Station
p_{EN}	Correlation Coefficient

LIST OF ACRONYMS/ABBREVIATIONS

1-D	One-dimensional
2-D	Two-dimensional
3-D	Three-dimensional
CB	Central Basin
CH	Central High
ÇB	Çınarcık Basin
EAF	East Anatolian Fault
EAFZ	East Anatolian Fault Zone
FEM	Finite Element Method
GMT	Greenwich Mean Time
GNSS	Global Navigation Satellite System
HM	Homogeneous
HS	Hard Sediments
HT	Heterogeneous
KB	Kumburgaz Basin
Lat	Latitude
Lon	Longitude
MIT	Massachusetts Institute of Technology
MMF	Main Marmara Fault
MTA	General Directorate of Mineral Research and Exploration of Turkey
NAF	North Anatolian Fault
NAFZ	North Anatolian Fault Zone
O	Overburden
PyLith	Finite Element Code for Quasi-static Simulations
S	Sediments
SS	Soft Sediments
TB	Tekirdağ Basin
USGS	The United States Geological Survey
UTM	Universal Transverse Mercator

VB	Best-fitting model
WH	Western High

1. INTRODUCTION

Long-term movement of the tectonic plates results in stress build-up around the faults until the fault's frictional strength is overcome. This frictional stick-slip instability of existing faults causes earthquakes in the Earth's brittle crust. The seismic activity is accompanied by a stress state caused by faulting due to the highly heterogeneous inner earth structure. Nevertheless, seismic numerical simulations have predominantly been carried out with various simplified features such as homogeneous half-space, elastic rheology, flat earth surface, etc. These simplifications do not take into account the effects of topography and medium heterogeneity, which may have a significant effect on the inferences about fault behavior.

Defining the optimal source parameters that justify observed variations requires numerical models and algorithms of seismic processes. Natural features of seismic regions, such as topography or rheological properties, can be applied with various numerical methods. The finite element method (FEM) is one of the most effective methods for calculating stress, strain, etc., in complexities of this nature. Thus, we use the finite element method in this work, which enables us to insert real topography in the computational domain and medium heterogeneities obtained from previous studies. A forward modeling technique is used in order to get estimates of ground deformation predicted throughout the interseismic phase, and the results are compared with geodetic data.

Our case study for the application of FEM is the Main Marmara Fault, the northern branch of the North Anatolian Fault in the Marmara Region. The only section of the NAF that has not been broken by a major earthquake in the past century is the western stretch under the Marmara Sea. Considering this seismic gap of ~150 km under the Marmara Sea, understanding the interseismic behavior of the MMF is crucial in order to assess earthquake hazards in the region, which hosts a population of more than 20 million. In that regard, two critical factors are the locking distribution and the slip rate of the fault since they provide an insight into the seismic moment deficit that can be released during an upcoming earthquake.

According to the most recent findings, the interseismic coupling or locking, which is defined as the proportion of the interseismic slip rate deficit to the long-term plate velocity, varies throughout the MMF. There is also the theory that the MMF is completely locked and that the deep basins surrounding the fault cause asymmetrical strain to accumulate and become localized near the fault. Within the scope of our study, we take into account the conflicting impacts caused by the heterogeneous structure and interseismic behavior across the MMF.

The goal of this study is to achieve the application of more realistic characteristics to the fault geometry, the elastic medium heterogeneities, and the topographic and basin geometries for the forward problem, starting with the application of realistic geometries for the sources in a homogeneous elastic medium and then continuing with the application in a heterogeneous elastic medium to retrieve ground deformation. The kinematic model is based on a realistic 3-D fault geometry in which a fault slip rate below a given locking depth ranging from 0 to 20 kilometers is restricted in every section of the MMF. The fits to GNSS velocity data are optimized by changing each segment's interseismic locking depth. In this study, our goal is mainly to construct a three-dimensional model of the area to get an understanding of the impacts of fault locking and basins on the region's deformation.

1.1. The Structure of the Thesis

This study is divided into the following sections:

Chapter 2. Tectonics of Turkey and the Marmara Region

This chapter outlines the tectonics of Turkey and its surroundings, as well as the geological overview of the Marmara Region.

Chapter 3. Governing Equations for Deformation Analysis

In this chapter, the governing equations that characterize deformation analysis are formed. The derivation of Elasticity is discussed here, and mathematically, the fundamental laws of continuum mechanics are presented.

Chapter 4. The Finite Element Method

In this chapter, we will describe the numerical approach known as the Finite Element Method (FEM). With regard to this method, we will go over some particular benefits and drawbacks.

Chapter 5. Application of Finite Element Modeling to the Marmara Region

At the beginning of this chapter, we will go over some of the more basic seismology principles. After that, we will show how the procedure is implemented while developing a 3-D model of the Main Marmara Fault in the Marmara Region to understand the deformation in the interseismic phase.

Chapter 6. Forward Modeling Results for Marmara Ground Deformation

In this chapter, we perform numerical simulations to conduct an analysis of the long-term ground deformation that has been observed in the Marmara Region over the course of about 20 years. We use a forward modeling technique employing FEM calculations both in 3-D homogeneous and heterogeneous models. This allows us to take topographic effects into consideration in addition to a complex distribution of material features. A variety of different tests are developed, and the misfits are calculated to compare the models in order to estimate the best-fitting interseismic locking model of the MMF.

Chapter 7. Discussion

A number of different numerical models are discussed in order to get an understanding of how the complicated distribution of elastic media characteristics and the locking depths cause the numerical findings to vary from those obtained with a homogeneous medium. In order to more accurately define the interseismic behavior of the MMF, we evaluate its seismicity distribution, focal mechanisms, and repeaters.

Chapter 8. Conclusions

The final chapter highlights the unique and essential contributions made by this thesis and provides a summary of the results. Furthermore, it outlines suggestions for additional research in order to better comprehend the fault's behavior.

2. TECTONICS OF TURKEY AND THE MARMARA REGION

2.1. Tectonics of Turkey

Turkey's tectonics are mostly controlled by the collision of the Eurasia and Arabia plates in the east (McKenzie, 1972) and by the back-arc extension caused by the rollback of the 700 km wide old subducting plate along the Hellenic trench in the west (Le Pichon and Angelier, 1979), leading Anatolia to rotate in a counterclockwise direction relative to Eurasia (McClusky *et al*., 2000; Reilinger *et al*., 2006; Figure 2.1). Consequently, this led to the construction of two major transform fault zones encircling Anatolia: the East Anatolian Fault Zone (EAFZ) in the east, which is a left-lateral strike-slip fault, and the North Anatolian Fault Zone (NAFZ) in the north, which is a right-lateral strike-slip fault (Şengör *et al*., 2005).

The NAF, which is a right-lateral east-west oriented transform fault that runs over 1200 km and accommodates Anatolia's relative motion with respect to Eurasia, creates a connection between the East Anatolian convergence zone and the Hellenic Trench (Şengör *et al*., 2005, 2014). Since the early twentieth century, the NAF has generated a number of earthquakes with $M_w > 7$. The first of these was the M_w 7.8 Erzincan earthquake that occurred in 1939 and moved primarily in a westerly direction, as shown in Figure 2.1 (Barka, 1996; Barka *et al*., 2002; Stein *et al*., 1997). The most recent of the large earthquakes east of the Marmara occurred in 1999 with the M_w 7.4 İzmit and M_w 7.2 Düzce earthquakes (Delouis *et al*., 2002; Konca *et al*., 2010; Reilinger *et al*., 2000). The rupture of the 1999 M_w 7.4 İzmit earthquake ended before it reached the Princes' Islands section after propagating to the west of the İzmit Bay, according to Gasperini *et al*. (2011a). In 1912, the M_w 7.4 Mürefte earthquake broke the Ganos section in the west of the Marmara. The M_w 6.9 earthquake that occurred farther to the west in 2014 broke the North Aegean Trough, a section of the NAF (Konca *et al*., 2018). This means that the MMF beneath the Marmara Sea is the only part of the fault that has remained unbroken during this seismic cycle since the beginning of the 20th century. This seismic gap under the Marmara Sea is about 150 kilometers in length. The NAF's northern branch MMF, which has been the most active segment in this area (Meade *et al*., 2002; Reilinger *et al*.,

2006), accommodates almost as much as 20–22 mm/yr of the region's approximate 25 mm/yr of relative motion. The unruptured sections of MMF pose significant seismic risks due to their closeness to major metropolitan areas, particularly İstanbul.

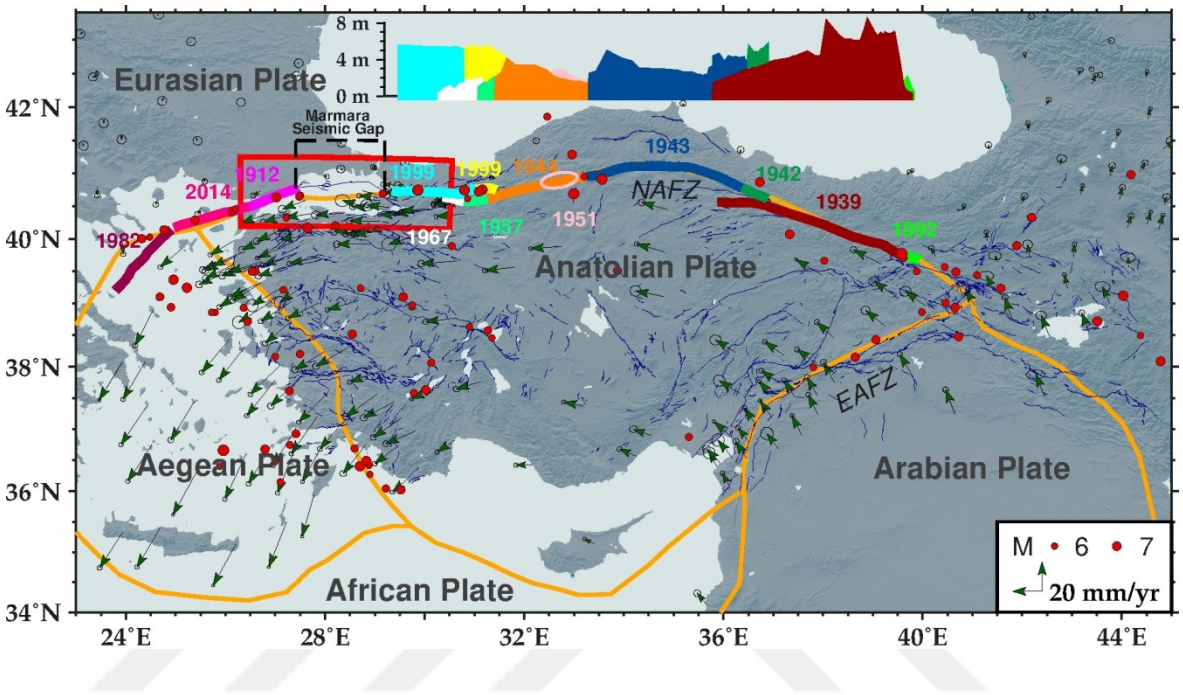

Figure 2.1. Anatolia plate tectonics, with black arrows and green arrowheads showing GNSS velocities of Reilinger *et al*. (2006) relative to Eurasia and light orange lines showing plate boundaries (Bird, 2003) of the EAFZ, NAFZ, etc. The same color represents right-lateral offsets and earthquake surface ruptures along the NAF since 1939 (Barka *et al*., 2002; Emre *et al*., 2013; Hori *et al*., 2017; Stein *et al*., 1997). The red frame indicates the study area. The red circles represent the M > 6 earthquakes from 1900 reported by the USGS.

2.2. The Geometry of the Main Marmara Fault

The NAF accommodates Anatolia's westward relative motion with respect to Eurasia at a rate of about 25 mm/yr (Reilinger *et al*., 2006). Between the Karliova Triple Junction and east of Bolu, most of the NAF is predominantly characterized by a single fault zone, which is a boundary between the Eurasian and Anatolian plates. However, it separates into two main branches just before it enters the Sea of Marmara (Armijo et al. 1999, 2002; Figure 2.2). The northern branch, which goes into the Marmara Sea from the İzmit Bay

(Alpar and Yaltırak, 2002; Cormier *et al*., 2006), travels across the Sea of Marmara by following the northern shelves of various basins (Le Pichon *et a*l., 2001, 2003), exits the Marmara Sea in the west at the Gelibolu Peninsula, where it is known as the Ganos Fault, and finally reaches the Aegean Sea from the Saros Bay (Yaltırak and Alpar 2002a). The southern branch, often termed the middle branch in studies that suggest three branches, after passing through İznik Lake, runs along the southern shores of the Sea of Marmara between Gemlik Bay and the Kapıdağ Peninsula, and then it turns toward the southwest (Kurtuluş and Canbay, 2007; Yaltırak and Alpar, 2002b). After forming the southern margin of the Bursa Graben, the faults farther south go through the Biga Peninsula and reach into the Aegean Sea (Hergert *et a*l., 2011). The majority of the plate movement, which is estimated to be between 20 and 22 mm/yr (Ergintav *et al*., 2014), is now accommodated by the northern branch, which is known as the Main Marmara Fault (MMF; Le Pichon et al., 2001). The remainder of the plate movement, which is around 3-5 mm/yr, is most likely divided along right-lateral faults farther south and the southern İznik-Gemlik branch (Hergert and Heidbach, 2010).

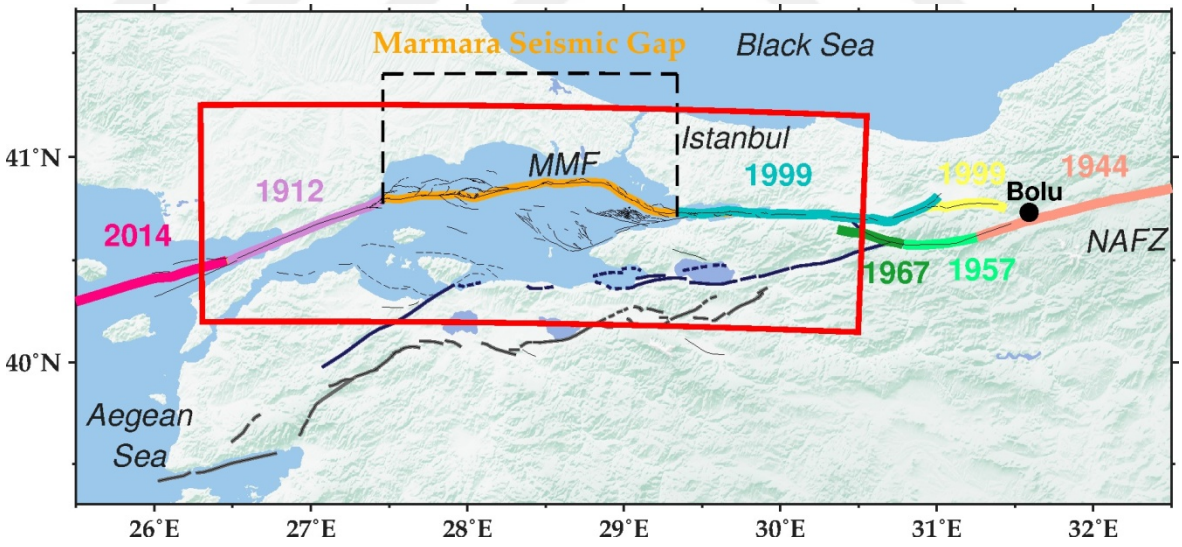

Figure 2.2. NAF branches in Western Turkey, as well as earthquake surface ruptures along the NAF (Armijo *et al*., 2002; Emre *et al*., 2013; Uçarkuş *et al*., 2011) and Marmara study area (red frame).

Many marine geological surveys were conducted following the M_w 7.4 İzmit earthquake in 1999, which ruptured about 50 km of the NAF beneath the İzmit Bay in the eastern Marmara Sea (Gasperini *et al*., 2011a; Uçarkuş *et al*., 2011), to map the active fault strands (e.g., Armijo *et al*., 2005; Le Pichon *et al*., 2001; Şengör *et al*., 2014), assess the influence of significant earthquakes on the sedimentary basins (e.g., McHugh *et al*., 2006), and estimate fault slip rates over seismic cycles (e.g., Gasperini *et a*l., 2011b). Also, fault offset is reported for the İzmit earthquake rupture based on high-resolution seafloor bathymetry (e.g., Gasperini *et al*., 2011b; Uçarkuş *et al*., 2011). In addition, studies involving paleoseismology, GPS, gas emission along fault ruptures, seafloor geodesy, topography, etc., have all been conducted to map the fault zones under the Marmara Sea (e.g., Laigle *et al*., 2008; Le Pichon *et al*., 2003; Reilinger *et al*., 2006; Meghraoui *et al*., 2012).

The presence of a fault segment can be identified by the location of a major earthquake and a related coseismic surface rupture, but these elements may not entirely represent the size of the fault and hence the seismic gap. Geometrical complexities such as fault bends, step-overs, and pull-apart basins can be used to identify the size and limits of these fault segments (Wesnousky, 2006). From this point of view, the geometry of the MMF is rather complicated and has three main bends beneath the Marmara Sea. These bends are called the Ganos, İstanbul, and Tuzla Bends, as depicted in Figure 2.3a (Hergert *et al*., 2011). The right-lateral strike-slip domain that characterizes the NAF system exhibits three forms of deformation in the Marmara Sea. These are mostly E–W directed, almost entirely pure strike-slip faults; others are NE–SW aligned transpressive structures and NW–SE aligned transtensional depressions along the restraining and releasing bends, respectively. Tekirdağ segment's extensional component along the basin's westernmost margin represents an exception to this general pattern (Gasperini et al., 2021). MMF fragmentation occurred on a variety of scales, but nevertheless, the primary segments formed over 3 main right-lateral oversteps that separated primary fault branches beneath the Marmara Sea. These are the transtensive Çınarcık section, the east-west central sections, and the westernmost Tekirdağ section, from east to west (Gasperini *et al*., 2021). The Çınarcık Segment, located near İstanbul in the Marmara Sea, displays transtensive deformations at the NAF's western extremity (Barka, 1992), where a releasing bend in the strike-slip system generates a pull-apart basin (e.g., Armijo *et al*. 2002, 2005). Following

that, the existence of an oblique segmented shear zone linking the İzmit segment to the Ganos Fault is suggested (e.g., Armijo *et al*., 2002; Meghraoui *et al*., 2012; Parke *et al*., 2002). According to other studies, MMF is a single major strike-slip fault (e.g., Le Pichon *et al*., 2001).

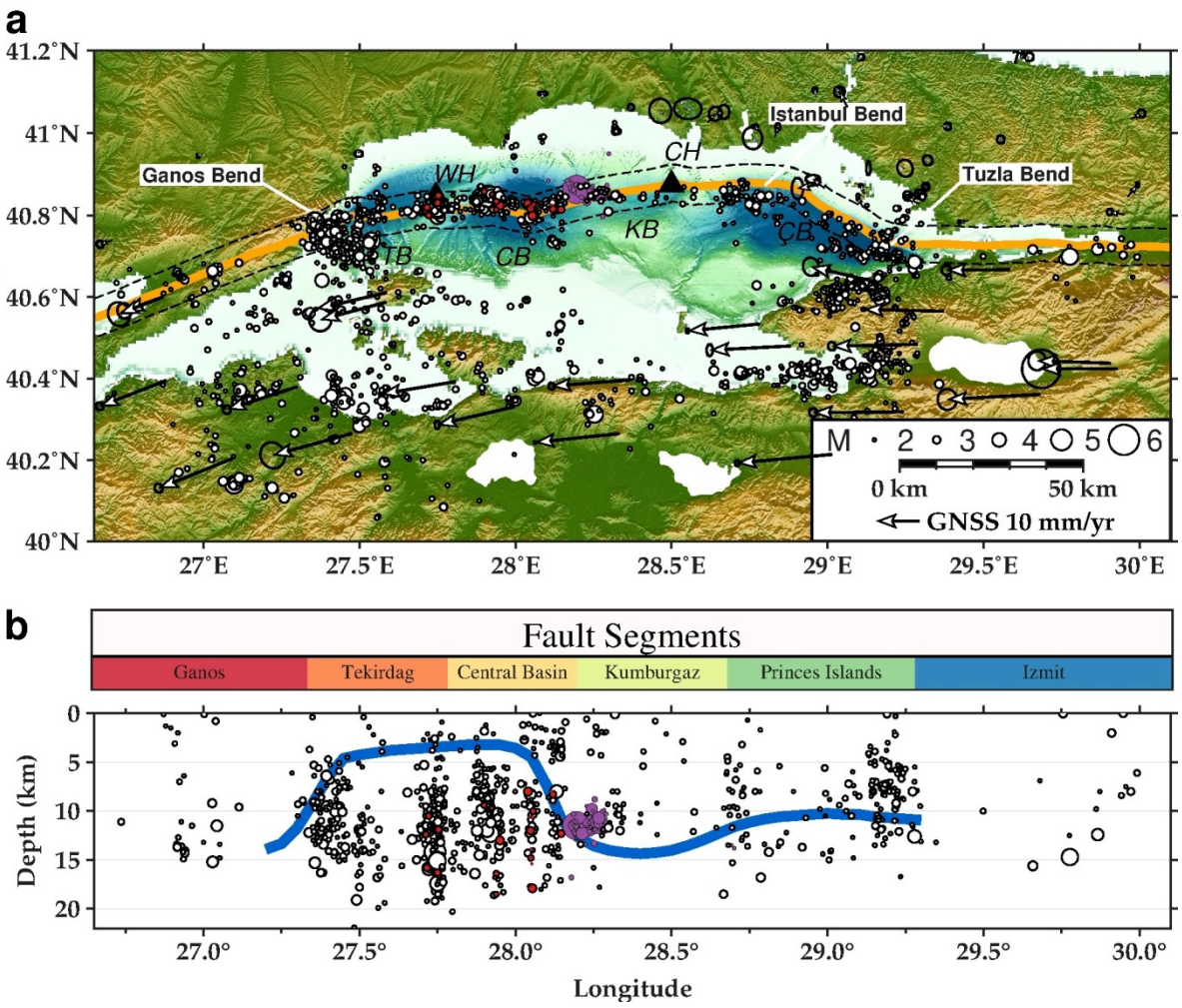

Figure 2.3. (a) Seismicity distribution including the 2007–2015 M≥2 seismic events (black circles with white fillings; Schmittbuhl *et al*., 2016b), the 2019 Silivri earthquake series (purple circles; Karabulut *et al*., 2021), and clusters of repeating earthquakes (red circles; Schmittbuhl *et al*., 2016a; Uchida *et al*., 2019), as well as two hydroacoustic arrays (black triangles; Lange *et al*., 2019; Sakic *et al*., 2016; Yamamoto *et al*., 2019) and GNSS velocities (black vectors with white arrowheads; Ergintav *et al*., 2014). MMF's geometrical bends are also shown. The surface trace is shown by a light orange line, while the 5 km distance contours are shown by black dashed lines. (b) A cross-section taken from the seismicity distribution shown in a) using the identical colors. The locking distribution of MMF suggested by Schmittbuhl *et al*. (2016b) is shown by a blue curve.

According to the geometrical complexity that connects them, the entire main fault is split into six segments from west to east: the Ganos, Tekirdağ, Central Basin, Kumburgaz, Princes' Islands, and İzmit segments (Figures 2.3a and 2.3b). The majority of these segments were formed along oversteps or bendings and were named according to the corresponding sedimentary basins. In the east of İstanbul, between Tuzla and İstanbul Bends, the Princes' Islands section forms a releasing bend which dips towards the southwest at an angle of approximately 79° until it reaches 15 km below sea level (Hergert and Heidbach, 2010). The Tekirdağ Segment links the Central Basin to the Ganos Segment on the western shore of the Marmara Sea at the Ganos Bend, which forms a restraining bend.

2.3. Studies of Fault Behavior Using Geodetic Data

The morphology of the Marmara Sea is complicated, comprising deep basins and steep slopes divided by topographic highs, and the MMF traverses four deep sedimentary basins: the Tekirdağ (TB), Central (CB), Kumburgaz (KB), and Çınarcık Basins (ÇB) from west to east, as shown in Figure 2.3a. The MMF cuts across the southern portion of the Tekirdağ and Central Basins as well as the northern shelf of the Kumburgaz and Çınarcık Basins. Asymmetry is also evident due to the location of MMF in relation to the depositional center of the basins. According to Bécel *et al*. (2009, 2010), in addition to all of these bathymetric structures, there is a large amount of sediment all along the MMF in the Sea of Marmara, with depths down to the basement rock ranging from 3 to 6 km.

The observed geodetic fault parallel velocities on the northern coast are overestimated for a locked fault down to 15 km. Several explanations were brought forward to remedy this situation. For example, Meade *et al*. (2002) employed a shallow locking depth of about 6.5 kilometers and shifted the mapped fault southward, far from the Marmara's northern shore, to explain and match the measured long-term GNSS velocities over the northern shore. The primary fault under the Sea of Marmara, on the other hand, is quite accurately mapped, and it is located towards the northern shores (Le Pichon *et al*., 2001). This suggests that the absence of strain buildup on the northern side of the MMF is due to other factors.

The MMF's interseismic strain does seem to be heterogeneous, with some portions that are locked interlaced with portions that are fully or partially creeping, according to prior geodetic and seismological research (e.g., Bohnhoff *et al*., 2013; Ergintav *et al*., 2014; Schmittbuhl *et al*., 2016b; Klein *et al*., 2017; Bulut *et al*., 2019; Özbey *et al*., 2021; Yılmaz *et al*., 2022). A 1-D approach of infinitely deep vertical strike-slip faults (Savage and Burford, 1973) and GNSS velocity data collected on land were used by Ergintav *et al*. (2014) in order to determine the depth of locking between earthquakes. According to their findings, there is no indication of strain buildup along the segments of the fault zone that are located in the Tekirdağ, Central, and Kumburgaz Basin regions. However, the strain could be building up along the Princes' Islands section of the fault zone. Both the Ganos and İzmit segments, in the west and east of the Marmara Sea, respectively, are considered to be completely locked down to a depth of 7.5 kilometers.

One of the problems with this 1-D vertical strike-slip fault method is that it assumes an elastic half-space embedded by a semi-infinite fault (Savage and Burford, 1973) and ignores the three-dimensional geometry of the basin structure and fault system. Instead, data is projected onto various profiles that are perpendicular to the fault segments to determine the locking depth. In a subsequent study, Klein *et al*. (2017) utilized a three-dimensional fault embedded in a homogeneous half-space model. The results of this study revealed that analyzing by employing a 2-D fault geometry would be too simple for the area. They further demonstrated that the MMF has heterogeneous interseismic behavior even though the resolution is insufficient to deduce the interseismic locking behavior. Several other studies based on the inversion of GPS data also obtained very similar results in terms of locking distribution (Bulut *et al*., 2019; Özbey *et al*., 2021). The only difference is that, according to Özbey *et al*. (2021), the west of 28.2°E longitude is creeping while the east is locked; Bulut *et al*. (2019) found that this part is substantially locked but both the Western High and Central High are partially creeping.

Le Pichon *et al*. (2005) provided an alternative way of explaining the GNSS data that have been reported. Both the interseismic coupling and the manner in which the strain is distributed across the fault might be influenced by the presence of a thick layer of sediment that extends to a depth of 6.2 kilometers (Bécel *et al*., 2010) under the Marmara Sea (e.g., Fialko, 2006). Despite the fact that the differences in fault coupling can explain rather well

most of the available geodetic data, it is not clear if the observations can be accounted for only just by the elastic structural heterogeneity, given that these models do not take into account the 3-D structure. According to Le Pichon *et al*. (2005), the absence of strain buildup indicated from multiple stations north of the fault could be due to a difference in rigidity across the fault. These findings for the Marmara Region were based on a similar set of GNSS data. Their 1-D profile technique employs a fault that is locked below to a depth of 10.5 km. They then apply a 10-fold difference in stiffness on either side of the fault, with the southern side being more compliant, in order to fit the profiles that are perpendicular to the fault. It is difficult to discern between the two approaches since there is not enough high-resolution geodetic data in the area near the fault.

In light of the limitations of onshore geodetic measurements, research into the near-fault accumulation of strain was carried out with the assistance of two hydroacoustic submarine deployments. The first survey (e.g., Sakic *et al*., 2016; Lange *et al*., 2019) was conducted east of the Kumburgaz Basin on the Central High (CH), and the second survey was carried out on the Western High (WH) in the west of the Central Basin (Yamamoto *et al*., 2019; Figure 2.3a). According to the results of these hydroacoustic range studies, the fault may be locked along the Central High, although there is an estimated surface creep of about 10 mm/yr along the Western High. This value represents approximately half of the predicted fault slip rate. The results of this research provide further proof that the MMF has heterogeneous interseismic behavior.

2.4. Studies of Seismicity and Repeating Earthquakes Along the MMF

The MMF has been observed to have a heterogeneous distribution of seismicity, which is another interesting finding regarding this fault. In order to explain MMF's locking behavior, some seismicity studies depend on the location distribution of the earthquakes that occur in close proximity to the main fault. This method presumes that the parts of the fault that are fully locked do not cause any earthquakes, whereas the parts that are partially or fully creeping do cause earthquakes owing to minor asperities located in the creeping zones.

According to the findings of Bohnhoff *et al*. (2013), the Princes' Islands section of the MMF does not produce any background seismicity in the interseismic period down to a depth of 7-8 km throughout a 40-km length surrounded by complex geometrical boundaries and by a significantly higher rate of seismicity and moment release. The silent zone encompassed by a higher rate of seismicity is considered a seismic gap and interpreted as a 40-km fully locked segment. Schmittbuhl *et al*. (2016b), studying the seismic activity of the entire MMF, inferred that whereas the Kumburgaz and Princes' Islands segments have a low rate of background seismicity and may be locked below a depth of about 10 km relying primarily on seismogenic depth, the Tekirdağ and Central Basin segments exhibit extensive high seismicity zones and are viewed as unlocked (Figures 2.3a and 2.3b).

Nevertheless, it is not quite obvious if the seismic activity that these studies found is a direct sign of the behavior of the fault. There is a possibility that the pattern of seismicity that has been reported could also be affected by other elements, such as the short observation duration of the background seismicity and complex geometries.

Small asperities in creeping zones are frequently understood as repeaters, which have a tendency to rupture in almost the same general places on a regular basis over time (Harris, 2017). The existence of repeating earthquakes is typically interpreted as indirect evidence of creep in a fault zone. Uchida *et al*. (2019) and Schmittbuhl *et al*. (2016a) found seismic repeaters along the Central Marmara with depths ranging between 3.8 and 18.5 km, and they predicted the slip rates in the order of plate rate. The presence of these repeating earthquakes throughout the Central Basin, as shown in Figures 2.3a and 2.3b, also provides additional evidence that the fault is not fully locked in this region.

2.5. Historical Earthquake Studies

The MMF has the potential to produce major earthquakes, according to studies based on historical earthquakes. The most recent major earthquake along the whole MMF with an $M > 7$ occurred in 1766. This earthquake most likely broke the Princes' Islands segment (Ambraseys and Jackson, 2000) and generated a ~M7.1 earthquake (Ambraseys, 2002; Gasperini *et al*., 2021). However, other $M > 7$ earthquake locations are unknown and are

the subject of much controversy. Historical earthquake studies suggest that the last major earthquakes that broke the Kumburgaz and Central Basin segments were an M7.2 earthquake in 989 and an M7 earthquake in 1343, respectively (Ambraseys, 2002; Pondard *et al*., 2007; Şengör *et al*., 2005). It is clear from these estimations that the central parts of the MMF are likely capable of producing major earthquakes, although the recurrence rate is substantially higher than the nearby İzmit segment in the east and Ganos segment in the west of the Marmara Sea, which are estimated to have roughly 250 and 300 years of recurrence rates (Dikbaş *et al*., 2018; Meghraoui *et al*., 2012), and the number of big seismic events under the Sea of Marmara is far lower (Meghraoui *et al*., 2012). Based on the loading that was caused by the earthquakes that occurred in 1999 as well as historical earthquakes, the likelihood of a large seismic event occurring under the Marmara Sea during the next 30 years was estimated by Parsons (2004) to be 44 ± 18 percent following the recent M_w 7.4 İzmit and M_w 7.2 Düzce earthquakes that occurred in 1999.

Furthermore, since the recurrence rates of major earthquakes are much longer, the MMF under the Marmara Sea behaves differently in terms of background seismicity. During the interseismic phase, the majority of the NAF, which includes the Ganos and İzmit sections, does not create a large quantity of seismicity along the major fault zone. On the other hand, as shown in Figures 2.3a and 2.3b, the sections of MMF under the Marmara Sea produce a substantial quantity of seismicity (Schmittbuhl *et al*., 2016b). It is unclear if these earthquakes happen as a result of geometrical complications or interseismic behavior.

According to the seismicity, historical earthquakes, and other possible explanations for GNSS data, the MMF has to be examined in greater depth to understand the link between interseismic fault behavior, background seismicity, and structural complexity in greater detail. Therefore, we focus on the MMF in terms of the relationships between these elements since it has not created any major earthquakes since the last century and poses a hazard risk for the area.

3. GOVERNING EQUATIONS FOR DEFORMATION ANALYSIS

The fundamental laws of continuum mechanics, which is the field concerned with the mechanics and behavior of materials, are mathematically defined by three physical principles: the conservation of mass; the second law of Newton (conservation of linear momentum); and the first law of thermodynamics (conservation of energy). Governing equations can be solved generally easily with the help of certain material idealizations, such as elastic material models, and in continuum mechanics, these materials can also be approximated as continuous over a given period of time and length.

3.1. The Derivation of the Elasticity Equation in Index Notation

The stress equilibrium equations, which are a set of 3 paired partial differential equations, must be solved to identify the displacement and stress state as a consequence of the application of particular boundary displacements or loads. Newton's second law is used to derive these equations. The following equation shows the conservation of linear momentum for a body of any form with a volume V that is bounded by a surface S, where force is the rate of momentum change with respect to time. Mass conservation is one of the most fundamental physics concepts, meaning that the mass stays the same within a given problem domain unless the mass is not created or destroyed, and if mass m is constant, then the force is F=dp/dt=m*dv/dt=ma. The second law of Newton states that a body's overall force equals its mass multiplied by its acceleration. The overall force exerted on the body can be found by adding up all the internal body forces and all of the forces that come from the surface traction exerted on the body's outside border.

When we equate the total inertia to the overall force, we get the expression of Newton's law of motion,

$$\frac{\partial}{\partial t}\int_V \rho\frac{\partial u_i}{\partial t}dV = \int_V f_i dV + \int_S T_i dS, \tag{3.1}$$

which can be found in Equation (3.1). On the right side of Equation (3.1), f_i stands for the body force density, which is also known as the force per unit volume, whereas T_i stands for the surface traction per unit area (Aagaard *et al*., 2017b). On the left side of the equation,

the mass density per unit volume is denoted by ρ, and the displacement field is denoted by u_i.

In cases when the rock is in static equilibrium or displacements are extremely slow, the left side of the equation may be omitted, and this simplifies the equation of motion to an equilibrium equation. We first convert the surface integral into the volume integral over the whole body. Then, we derive the most useful differential form of the equation by invoking the divergence theorem. In this regard, to use the divergence theorem with the surface integral, first we write the traction

$$T_i = \sigma_{ij} n_j, \tag{3.2}$$

in Equation (3.2) in terms of stress components. When Equation (3.2) is substituted into Equation (3.1), we get the following:

$$\frac{\partial}{\partial t}\int_V \rho \frac{\partial u_i}{\partial t} dV = \int_V f_i dV + \int_S \sigma_{ij} n_j dS. \tag{3.3}$$

The application of the divergence theorem gives

$$\int_V a_{i,j} dV = \int_S a_i n_j dS, \tag{3.4}$$

as shown in Equation (3.4). Substituting this equation into the surface integral yields

$$\frac{\partial}{\partial t}\int_V \rho \frac{\partial u_i}{\partial t} dV = \int_V f_i dV + \int_V \sigma_{ij,j} dV, \tag{3.5}$$

which can be rewritten as shown in Equation (3.6).

$$\int_V \left(\rho \frac{\partial^2 u_i}{\partial t^2} - f_i - \sigma_{ij,j} \right) dV = 0 \tag{3.6}$$

Since Equation (3.6) holds for any form of the body, the integrand must be zero at every point inside the volume V. Thus, the equation at all points can be concluded as follows:

$$\rho \frac{\partial^2 u_i}{\partial t^2} - f_i - \sigma_{ij,j} = 0 \; in \; V, \tag{3.7}$$

where u_i^0 is the displacement on surface S_u, while T_i is the traction on surface S_T, d_k is the slip on surface S_f, and R_{ki} is the global to fault coordinate transformation rotation matrix.

$$\sigma_{ij} n_j = T_i \; on \; S_T, \tag{3.8}$$

$$\sigma_{iJ} = \sigma_{ji} \; (symmetric), \tag{3.9}$$

$$u_i = u_i^0 \; on \; S_u, \tag{3.10}$$

$$d_k - R_{ki}(u_i^+ - u_i^-) = 0 \; on \; S_f. \tag{3.11}$$

To sum up, the governing equations that describe the rock deformation show that there are three unknown displacements and six unknown stress components. This means that the equations are not adequate to find out displacements and stresses. For a mathematically well-defined problem, the number of equations and unknowns must be equal. The six new equations are given by the strain-displacement relationships, which also introduce six further unknowns. Six more equations, which can take any form, such as linearly elastic, viscoelastic, etc., are also introduced using stress-strain relations. The equation of motion, stress-strain, and strain-displacement relations are a set of equations in which the quantity of unknowns is the same as the quantity of equations. In continuum mechanics, this is needed but not enough to have a well-defined math problem.

3.2. Governing Equations for Linear Elastic Materials

One of the most important rheological mediums is elasticity, in which the stress is linearly proportional to the strain and the elasticity can be fully recovered. At low temperatures and pressures and with small deformations, the rocks are almost elastic. The strain is the spatial gradients of the displacement field, which means the relative changes in the displacement field as a result of the material's deformations or changes in the form rather than any position changes. Most of the structural metals are approximately linear elastic at low strains.

The strain-displacement relationship for elasticity is as follows in index notation (Equation 3.12).

$$\varepsilon_{ij} = \frac{1}{2}\left(u_{i,j} + u_{j,i}\right) \tag{3.12}$$

Hooke's law is presented in the following equation, which shows how stress and strain relate to each other elastically.

$$\sigma_{iJ} = C_{ijkl}\varepsilon_{kl} \tag{3.13}$$

The C_{ijkl} 4th order elastic tensor, also known as stiffness, has a total of 81 components. However, only 21 of these components are independent due to the symmetry of the stress and strain tensors and the laws of thermodynamics. These components are needed to define the stress-strain relationship for an elastic solid. If the material is supposed to be isotropic, i.e., that the solids have identical characteristics in all directions, then it reduces the number of parameters to two, in which the first Lame parameter (λ) and shear modulus (μ, the material's resistance to shearing) are known as the Lame parameters.

$$C_{ijkl} = \lambda\delta_{ij}\delta_{kl} + \mu\left(\delta_{ik}\delta_{jl} + \delta_{il}\delta_{jk}\right) \tag{3.14}$$

$$\underline{C} = \begin{bmatrix} \lambda+2\mu & \lambda & \lambda & 0 & 0 & 0 \\ \lambda & \lambda+2\mu & \lambda & 0 & 0 & 0 \\ \lambda & \lambda & \lambda+2\mu & 0 & 0 & 0 \\ 0 & 0 & 0 & \mu & 0 & 0 \\ 0 & 0 & 0 & 0 & \mu & 0 \\ 0 & 0 & 0 & 0 & 0 & \mu \end{bmatrix} \tag{3.15}$$

Thus, the elastic stress-strain relationship for an isotropic material becomes

$$\begin{aligned} \sigma_{ij} &= \left[\lambda\delta_{ij}\delta_{kl} + \mu\left(\delta_{ik}\delta_{jl} + \delta_{il}\delta_{jk}\right)\right]\varepsilon_{kl} = \lambda\delta_{ij}\varepsilon_{kk} + 2\mu\varepsilon_{ij} \\ &= \lambda\delta_{ij}u_{k,k} + \mu\left(u_{i,j} + u_{j,i}\right) \end{aligned} \tag{3.16}$$

$$\begin{bmatrix} \sigma_{11} \\ \sigma_{22} \\ \sigma_{33} \\ \sigma_{23} \\ \sigma_{13} \\ \sigma_{12} \end{bmatrix} = \begin{bmatrix} \lambda+2\mu & \lambda & \lambda & 0 & 0 & 0 \\ \lambda & \lambda+2\mu & \lambda & 0 & 0 & 0 \\ \lambda & \lambda & \lambda+2\mu & 0 & 0 & 0 \\ 0 & 0 & 0 & \mu & 0 & 0 \\ 0 & 0 & 0 & 0 & \mu & 0 \\ 0 & 0 & 0 & 0 & 0 & \mu \end{bmatrix} \cdot \begin{bmatrix} \varepsilon_{11} \\ \varepsilon_{22} \\ \varepsilon_{33} \\ 2\varepsilon_{23} \\ 2\varepsilon_{13} \\ 2\varepsilon_{12} \end{bmatrix} \tag{3.17}$$

By substituting Equation (3.16) into Equation (3.7), we get

$$\rho\frac{\partial^2 u_i}{\partial t^2} - f_i - \left[\lambda\delta_{ij}u_{k,k} + \mu\left(u_{i,j} + u_{j,i}\right)\right]_{,j} = 0 \tag{3.18}$$

$$\begin{aligned} \rho\frac{\partial^2 u_i}{\partial t^2} &= f_i + \partial_j\left[\lambda\delta_{ij}\partial_k u_k + \mu\left(\partial_j u_i + \partial_i u_j\right)\right] \\ &= f_i + \partial_i\lambda\partial_k u_k + \lambda\partial_i\partial_k u_k + \partial_j\mu\left(\partial_j u_i + \partial_i u_j\right) \\ &+ \mu\partial_j\partial_j u_i + \mu\partial_j\partial_i u_j \\ &= f_i + \partial_i\lambda\partial_k u_k + \partial_j\mu\left(\partial_j u_i + \partial_i u_j\right) + \lambda\partial_i\partial_k u_k \\ &+ \mu\partial_i\partial_j u_j + \mu\partial_j\partial_j u_i \end{aligned} \tag{3.19}$$

If we define the first Lame parameter (λ) and shear modulus (μ) in terms of Young's modulus (E) and Poisson's ratio (ν),

$$\lambda = \frac{E\upsilon}{(1+\upsilon)(1-2\upsilon)}, \tag{3.20}$$

$$\mu = G = \frac{E}{2(1+\upsilon)}, \tag{3.21}$$

as shown in Equations (3.20) and (3.21), and substitute these equations into Equation (3.16), it yields

$$\sigma_{ij} = \frac{E}{(1+\upsilon)}\left(\frac{\upsilon}{(1-2\upsilon)}\delta_{ij}\varepsilon_{kk} + \varepsilon_{ij}\right). \tag{3.22}$$

If we define strain in terms of stress, then the equation can be written

$$\varepsilon_{ij} = \frac{1}{E}\left[(1+\upsilon)\sigma_{ij} - \upsilon\delta_{ij}\sigma_{kk}\right] \tag{3.23}$$

$$\begin{bmatrix}\varepsilon_{11}\\ \varepsilon_{22}\\ \varepsilon_{33}\\ 2\varepsilon_{23}\\ 2\varepsilon_{13}\\ 2\varepsilon_{12}\end{bmatrix} = \frac{1}{E}\begin{bmatrix}1 & -\upsilon & -\upsilon & 0 & 0 & 0\\ -\upsilon & 1 & -\upsilon & 0 & 0 & 0\\ -\upsilon & -\upsilon & 1 & 0 & 0 & 0\\ 0 & 0 & 0 & 2(1+\upsilon) & 0 & 0\\ 0 & 0 & 0 & 0 & 2(1+\upsilon) & 0\\ 0 & 0 & 0 & 0 & 0 & 2(1+\upsilon)\end{bmatrix}\cdot\begin{bmatrix}\sigma_{11}\\ \sigma_{22}\\ \sigma_{33}\\ \sigma_{23}\\ \sigma_{13}\\ \sigma_{12}\end{bmatrix} \tag{3.24}$$

as shown in Equations (3.23) and (3.24).

4. THE FINITE ELEMENT METHOD

Differential equations represent a wide range of real-world phenomena, providing mathematical models. For example, mechanical deformations can be modeled with differential equations. Analytical solutions to differential equations, which are used to explain physical processes, are only possible for a very small subset of problems, and even then, only for problems with relatively simple geometries. Numerical approaches are necessary for complex tasks, depending on the purpose of the study. FEM is one of these numerical methods, providing approximate solutions for differential equations.

The following five essential steps comprise the FEM:

1. Preprocessing: separation of the problem domain into finite elements
2. Formulation of elements: formation of element equations
3. Assembly: obtaining the system-wide equations from each element's equations
4. Solving the system-wide equations
5. Post Processing: Quantity of interest determination and response visualization

The FEM needs to divide the geometric domain or space representing the problem into a limited number of small regions called "meshes" (Figure 4.1). Known functions, such as linear or higher-order polynomials, can be used to estimate unknown parameters for all finite elements. This depends on the geometric positions, or nodes, that are used to set the shape of the finite element. In FEM, the governing equations are integrated over every finite element, and the solutions for the whole problem space are added up. Thus, in relation to a set of unknown parameters over whole elements, a finite linear equation set is generated that can be solved with linear algebra.

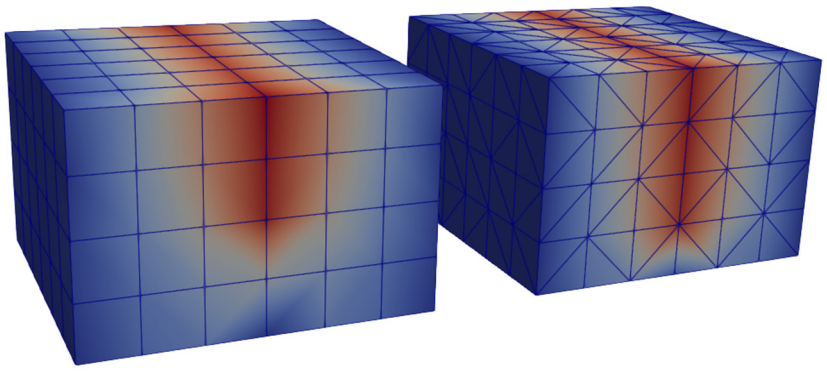

Figure 4.1. Illustrations of hexagonal and tetrahedral FEM meshes.

4.1. Advantages of the Finite Element Method

For all types of structural mechanics analysis, such as deformation and stress resolution in solid bodies or structural dynamics, the FEM is the discretization method of choice. The solution and its degree of approximation to the real answer are dependent on the number and size of the elements as well as interpolation functions. The FEM is built on a variational formulation that can be used to solve both discrete and continuous problems. Its ability to develop solutions for individual elements before assembling them to represent the entire problem is what distinguishes it from a number of other numerical approaches. In stress analysis, for example, we find the force-displacement or stiffness of any element and then put them all together to estimate the stiffness of the entire structure.

The FEM's most attractive features are its capacity for handling complex geometry and borders, with which it is easy to incorporate inhomogeneities and nonlinearities, as well as the reduction of a complicated problem to a number of simpler problems. The FEM is the most appropriate method for calculating stress and strain and, consequently, deriving changes in the geophysical signals in a given material. Therefore, when we describe the ground deformation in seismogenic areas, we use FEM to model heterogeneous media and for irregular topography, complex loading, and various rheologies.

4.2. Derivation of the Elasticity Equation with Finite Element Formulation in Index Notation

The FEM is made from the variational or weak formulation that is derived through multiplication of the original equation by an arbitrary function called the test function, also called the weight function. Since these "shape" functions are used as test functions for the discrete variational formulation, which is sometimes referred to as a "Galerkin expansion," they can be combined linearly to get an approximation for the continuous variable. The final solution is found by integrating the resultant equation over the whole domain. This section shows how the elasticity equation is found by implementing FEM in index notation (Aagaard *et al*., 2013, 2017b).

In the previous section 3.1, it was shown how to get the wave equation in its strong form as follows:

$$\sigma_{ij,j} + f_i = \rho\, \ddot{u}_\iota \text{ in V}, \tag{4.1}$$

$$\sigma_{ij} n_j = T_i \; on \; S_T, \tag{4.2}$$

$$\sigma_{ij} = \sigma_{ji}(\text{symmetric}), \tag{4.3}$$

$$u_i = u_i^0 \; on \; S_u, \tag{4.4}$$

$$d_k - R_{ki}(u_i^+ - u_i^-) = 0 \; on \; S_f, \tag{4.5}$$

where u_i^0 is the displacement on surface S_u, T_i is the traction on surface S_T, and d_k is the slip on surface S_f. Although the surfaces S_u and S_T may have some spatial overlap; at any location, a degree of freedom cannot be linked with both prescribed Neumann (traction) and Dirichlet (displacement) boundary conditions at the same time.

We get the weak form through the multiplication of the wave equation with a weighting function and setting the domain integral to zero, while the fault surface is ignored for now.

$$\int_V \left(\sigma_{ij,j} + f_i - \rho \ddot{u}_\iota\right) \varphi_i dV = 0 \tag{4.6}$$

$$\int_V \sigma_{ij,j}\varphi_i dV + \int_V f_i\varphi_i dV - \int_V \rho\ddot{u}_i\varphi_i dV = 0 \tag{4.7}$$

In Equation (4.8), the divergence theorem is applied to the multiplication of the Cauchy stress tensor with the weight function. Then, in Equations (4.9) and (4.10), the left side of the equation is expanded as follows:

$$\int_V \left(\sigma_{ij}\varphi_i\right)_{,j} dV = \int_S \left(\sigma_{ij}\varphi_i\right) n_j dS \tag{4.8}$$

$$\int_V \sigma_{ij,j}\varphi_i dV + \int_V \sigma_{ij}\varphi_{i,j} dV = \int_S \sigma_{ij}\varphi_i n_j dS \tag{4.9}$$

$$\int_V \sigma_{ij,j}\varphi_i dV = -\int_V \sigma_{ij}\varphi_{i,j} dV + \int_S \sigma_{ij}\varphi_i n_j dS \tag{4.10}$$

When Equation (4.10) is put into Equation (4.7) in its weak form, it yields

$$-\int_V \sigma_{ij}\varphi_{i,j} dV + \int_S \sigma_{ij}\varphi_i n_j dS + \int_V f_i\varphi_i dV - \int_V \rho\ddot{u}_i\varphi_i dV = 0 \tag{4.11}$$

Integration over S is split into S_T and S_u.

$$-\int_V \sigma_{ij}\varphi_{i,j} dV + \int_{S_T} \sigma_{ij}\varphi_i n_j dS + \int_{S_u} \sigma_{ij}\varphi_i n_j dS + \int_V f_i\varphi_i dV - \int_V \rho\ddot{u}_i\varphi_i dV = 0 \tag{4.12}$$

$$\sigma_{ij} n_j = T_i \; on \; S_T, \tag{4.13}$$

$$\varphi_i = 0 \; on \; S_u. \tag{4.14}$$

The weighting function φ_i is 0 on S_u. Substituting Equations (4.13) and (4.14) into Equation (4.12) gives:

$$-\int_V \sigma_{ij}\varphi_{i,j} dV + \int_{S_T} T_i\varphi_i dS + \int_V f_i\varphi_i dV - \int_V \rho\ddot{u}_i\varphi_i dV = 0. \tag{4.15}$$

Figure 4.2 shows the decomposition of the domain, where the fault surface is an internal boundary that separates the two domains.

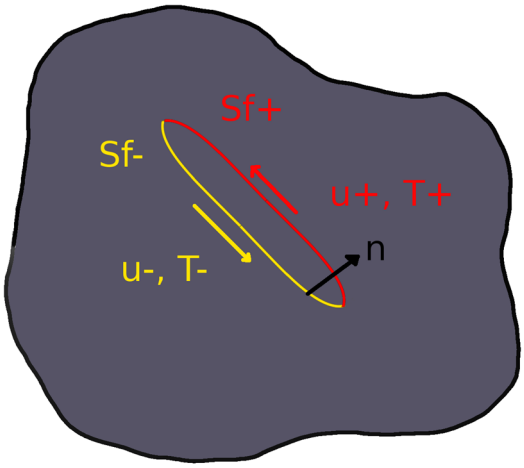

Figure 4.2. Schematic of a fault surface with continuous tractions and a jump in displacement due to fault slip, adapted from Aagaard *et al*. (2013).

Because the tractions on the fault surface are similar to the boundary tractions, we can also add the contributions of the fault surface tractions and then Equation (4.15) becomes:

$$-\int_V \sigma_{ij}\varphi_{i,j}dV + \int_{S_T} T_i\varphi_i dS - \int_{S_{f+}} l_i\varphi_i dS + \int_{S_{f-}} l_i\varphi_i dS + \int_V f_i\varphi_i dV - \int_V \rho\ddot{u}_i\varphi_i dV = 0. \quad (4.16)$$

The trial solution u_i, the weighting function φ_i, the fault slip d_i, and the Lagrange multipliers l_i are all written as linear combinations of basis functions in Equations from (4.17) to (4.20).

$$u_i = \sum_m a_i^m N^m \quad (4.17)$$

$$\varphi_i = \sum_n c_i^n N^n \quad (4.18)$$

$$l_i = \sum_p l_i^p N^p \quad (4.19)$$

$$d_i = \sum_p d_i^p N^p \tag{4.20}$$

After substituting Equations (4.17) to (4.20), Equation (4.16) can be expressed as follows:

$$\begin{aligned} -\int_V \sigma_{ij} \sum_n c_i^n N_{,j}^n \, dV + \int_{S_T} T_i \sum_n c_i^n N^n \, dS - \int_{S_{f+}} \sum_p l_i^p N^p \sum_n c_i^n N^n \, dS \\ + \int_{S_{f-}} \sum_{\mathrm{p}} l_i^p N^p \sum_n c_i^n N^n \, dS + \int_V f_i \sum_n c_i^n N^n \, dV \\ - \int_V \rho \sum_m \ddot{a}_i^m N^m \sum_n c_i^n N^n \, dV = 0 \end{aligned} \tag{4.21}$$

$$\begin{aligned} \sum_n c_i^n \Bigg(-\int_V \sigma_{ij} N_{,j}^n dV + \int_{S_T} T_i N^n dS - \int_{S_{f+}} \sum_p l_i^p N^p N^n \, dS \\ + \int_{S_{f-}} \sum_p l_i^p N^p N^n \, dS + \int_V f_i N^n dV - \int_V \rho \sum_m \ddot{a}_i^m N^m N^n \, dV \Bigg) \\ = 0 \end{aligned} \tag{4.22}$$

Since Equation (4.22) works for any arbitrary weighting function, the value inside the parentheses equals zero for all c_i^n. Then the equation simplifies to its basic form as follows:

$$\begin{aligned} -\int_V \sigma_{ij} N_{,j}^n dV + \int_{S_T} T_i N^n dS - \int_{S_{f+}} \sum_p l_i^p N^p N^n \, dS + \int_{S_{f-}} \sum_p l_i^p N^p N^n \, dS \\ + \int_V f_i N^n dV - \int_V \rho \sum_m \ddot{a}_i^m N^m N^n \, dV = \vec{0} \end{aligned} \tag{4.23}$$

The weak form of the constraint equation can also be obtained using the following algebra:

$$\int_{S_f} (d_i - u_i^+ + u_i^-) \varphi_i dS = 0, \tag{4.24}$$

$$\int_{S_f} \left(\sum_{\mathrm{p}} d_i^p N^p - \sum_m a_i^{m^+} N^{m^+} + \sum_m a_i^{m^-} N^{m^-} \right) \sum_n c_i^n N^n \, dS = 0, \tag{4.25}$$

$$\sum_n c_i^n \int_{S_f} N^n \left(\sum_p d_i^p N^p - \sum_m a_i^{m^+} N^{m^+} + \sum_m a_i^{m^-} N^{m^-} \right) dS = 0. \quad (4.26)$$

This form is obtained by multiplying the constraint equation by the weighting function and setting the integral across the fault surface to zero. Then Equation (4.26) is simplified

$$\int_{S_f} N^n \left(\sum_p d_i^p N^p - \sum_m a_i^{m^+} N^{m^+} + \sum_m a_i^{m^-} N^{m^-} \right) dS = 0 \quad (4.27)$$

as shown in Equation (4.27).

5. APPLICATION OF FINITE ELEMENT MODELING TO THE MARMARA REGION

Geodetic observations are critical for understanding the changes that occur during the interseismic, coseismic, and postseismic phases. The observed data may be affected by structures like topography, basins, or lateral changes in the rheological properties of seismic regions. Therefore, when numerical simulations are used to model this natural phenomenon, it is important to use the correct 3-D elastic structure and fault geometry in addition to boundary conditions.

For all of the calculations in the thesis, the finite element software PyLith is used, which is an open-source program that can be used for crustal deformations and can solve both explicit (i.e., dynamic) and implicit (i.e., quasi-static) problems. In order to solve a finite element problem, it is necessary to define some prior information like meshing, the types of elements, the types of materials, and the boundary conditions. Mesh information can be imported from LaGriT, CUBIT/Trellis, or ASCII files for simple tasks. While the supported cell types in 2-D are triangles and quadrilaterals, in 3-D they are hexahedra and tetrahedra. Different materials and rheologies can be implemented, such as isotropic elastic, linear or generalized Maxwell viscoelastic, Drucker-Prager elastoplastic, or power-law viscoelastic. There are also different boundary conditions, such as Dirichlet (prescribed velocities and displacements), Neumann (traction), and absorbing. Cohesive cells are implemented for the fault interfaces.

5.1. Faults as Dislocation Sources

Understanding the earthquake cycle, which consists of the coseismic rupture, the post-seismic relaxation, and includes the steady-state interseismic stages of strain accumulation, requires studying how the plates in the lithosphere move. Most earthquakes happen along faults, which are weakness zones in the Earth's crust that move relative to each other through differential or shear motion. A fault can accommodate the relative motion in three types of mechanisms, i.e., strike-slip along conservative boundaries, thrust

earthquakes at convergent boundaries, and normal faults accommodate when two blocks are moving away from each other.

An area that is stuck on an active fault surface because of greater friction is known as an asperity (Figure 5.1a). A fault is said to be locked when it does not slide down to a certain depth due to the frictional resistance on the fault being higher than the shear stress across the fault that is being applied by loads due to tectonic forces. Typically, for a crustal fault below 10 to 15 km, the rocks get hot enough that their behavior changes from stick-slip to creep or ductile deformation since their frictional strength increases while their ductile strength decreases. As a result, as the locked portions of the fault are loaded due to the creeping lower crust and relative motion of the plates in the continuum, the strain builds up around the preexisting fault zones. When frictional resistance is overcome during an earthquake, the faults slip, which causes fractures to propagate fast enough to radiate elastic waves. In most cases, the failure of an asperity triggers the rupture and makes it possible for the fault to move. However, in some cases, this relative motion takes place slowly enough so that a silent aseismic slip event occurs. Slow and almost continuous movement on faults is possible when there are no asperities along the boundary of the fault surface that enhance the frictional resistance.

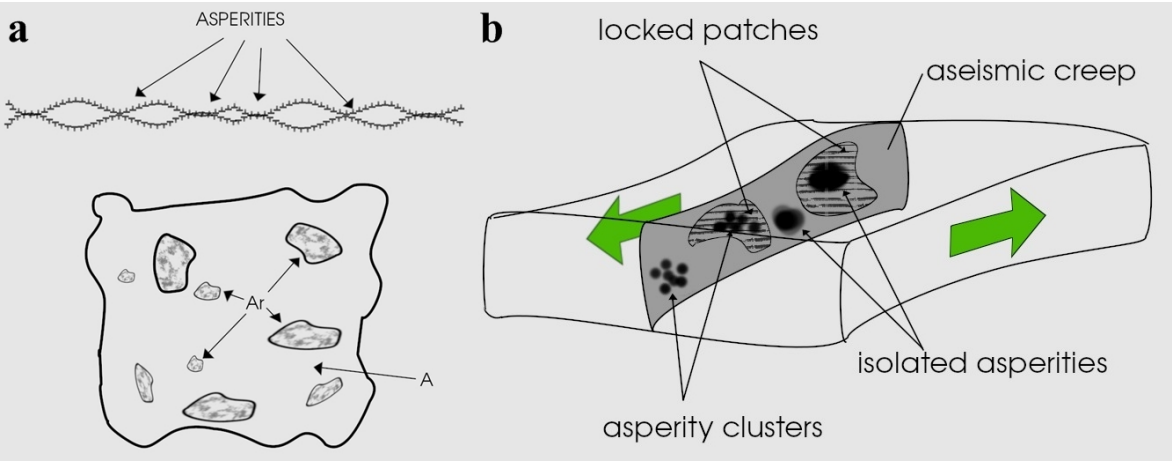

Figure 5.1. Schematic diagram of the contact surface of a real surface where the dotted areas show the real contact area, i.e., the asperity contact (A_r) within an apparent contact surface (A). (b) An illustration of a fault with heterogeneous locking behavior.

Numerous geodetic and seismological studies have shown that large earthquakes and aseismic slow slip events can both happen on the same individual fault, and seismic activity in these active fault zones varies in time and location along the fault. While some fault zones stay silent for decades, others cause earthquakes frequently. In some locations, seismicity is restricted to tiny zones of a few hundred meters; in others, it is spread over tens of kilometers. This change may happen across small distances (Liu *et al*., 2022). Based on these results, the contact surface of faults may have heterogeneous locking behavior (Figure 5.1b). Figure 5.2 shows a fault that is locked down to a certain depth, but below this locked (seismogenic) section of the crust, it transitions to steady sliding with the fault slip rate, as shown in the schematic model.

Fault coupling is characterized by the ratio of the slip rate deficit to the total fault slip rate and shows the capacity to accumulate strain. Low coupling faults have different earthquake patterns than those with high coupling. For example, low coupling faults do not have as many moderate or large earthquakes as the highly coupled segments due to less strain accumulation in the long term. Another line of evidence of creeping faults is the existence of repeating earthquakes. These small multiple fault ruptures on the same asperity may be an indicator of aseismic slip (Nadeau *et al*., 1995; Bürgmann *et al*., 2000). The high rate of background seismicity and the existence of repeaters are typically associated with fault creep (Harris, 2017; Liu *et al*., 2022).

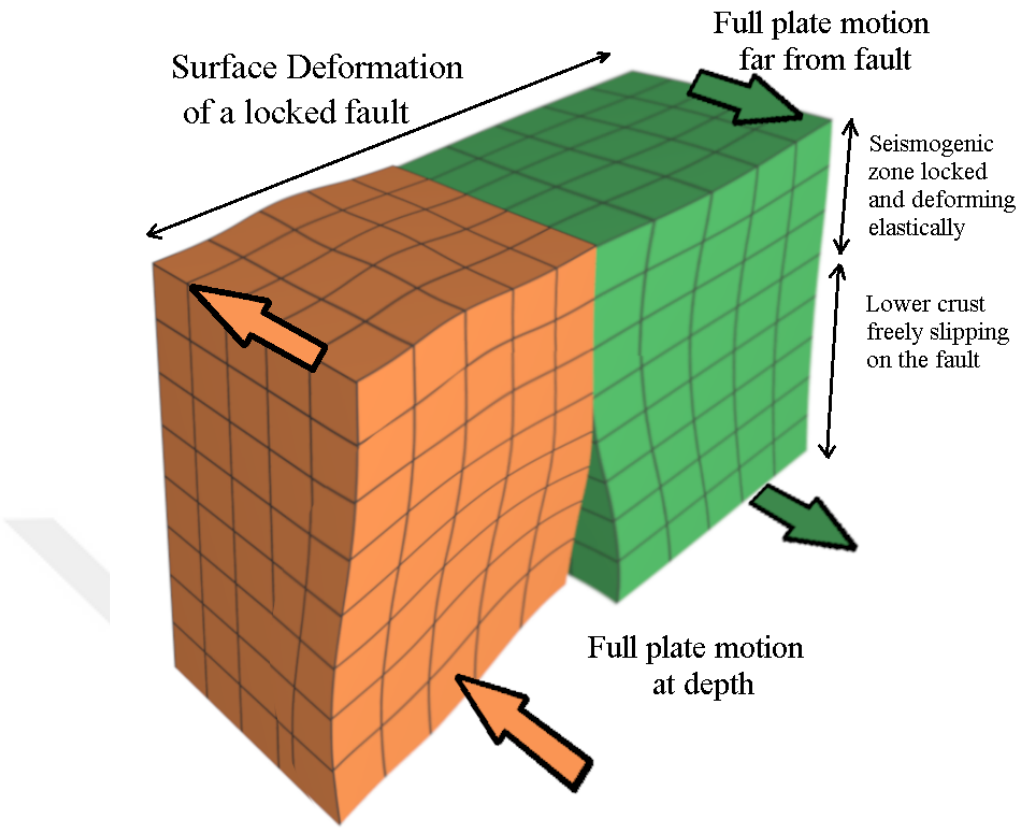

Figure 5.2. A schematic representation of a finite element model for a locked fault and a freely sliding unlocked fault below.

5.2. Interseismic Locking Behavior of the MMF in the Marmara Region

The primary objective of this study is to advance our knowledge of the interseismic locking behavior of the MMF in the Marmara Region by developing a three-dimensional elastic model of the area with the help of the finite element modeling program PyLith 2.2.1 by Aagaard *et al*. (2017a). We especially focus on the influence of deeper basins around the main fault on interseismic strain distribution and how having a homogeneous elastic model biases our predictions about interseismic fault behavior. Another question is whether utilizing seismicity along the main fault as an indication of interseismic behavior is appropriate.

Employing the finite element approach, we build a three-dimensional elastic Marmara model, so that we can conduct an appropriate analysis of the locking behavior of the MMF. Our 3-D models incorporate 3-D geometrical layers of the fault, topography, and basin features, as well as the Moho and upper-lower crustal boundaries. Our goal is to compare GNSS velocity data with the surface velocities derived kinematically in homogeneous and heterogeneous 3-D velocity structures under different scenarios of interseismic locking and the different impacts of interseismic fault coupling and basin structures. Further, we employ off-fault focal mechanisms to examine if changes in their pattern could be linked to interseismic strain heterogeneity caused by changes in interseismic fault coupling.

5.3. Data Set

In this study, we use interseismic GNSS-derived velocity data collected from the campaign and continuous mode stations (black arrows with white arrowheads in Figure 2.3a; Ergintav *et al*., 2014) to estimate the interseismic behavior of MMF. To prevent modeling of local deformation on the fault behavior, we excluded several GNSS sites from this study, particularly those in extremely soft sedimentary zones or landslide areas in İstanbul: N101, N103, N104, N107, N108, AVCT, OLU2, MAER, BGNT, and AVCI. Thus, out of the original data set of 86 GNSS sites within our study area, we utilized a total of 76 of them (Table A.1 in Appendix A). The larger east component's standard deviation ranges from 0.09 to 1.81 mm/yr depending on the duration of the measurements and whether it is a continuous or campaign station.

Compared to the GNSS measurements taken through the GNSS campaigns, the stated continuous GNSS station uncertainties are much lower (Table A.1 in Appendix A). When these data with their formal uncertainties are utilized for misfit computation, a few continuous stations with very low stated uncertainties overwhelm the misfits. To overcome this issue, the continuous stations' data covariance matrices are multiplied by 2.45, which is equivalent to shifting the 96 percent confidence interval to 68 percent. For the Marmara Island continuous station MADT, the reported standard deviation of 0.1 mm/yr is multiplied by 5. Nevertheless, in addition to misfit values with modified uncertainties, we also provide misfits employing the original uncertainties to inspect how much this choice

changes our results and inferences, and we demonstrate that the best-fitting locking models do not change significantly based on the choice of station uncertainties.

5.4. 3-D Marmara Model Setup and Method

For the purpose of developing a realistic and precise three-dimensional model of the Marmara Region research site, we made use of the finite element algorithm PyLith 2.2.1 by Aagaard *et al*. (2013, 2017a,b). The model domain has a depth of 38 km and its east-west length is 357 km, while the north-south width is 117 km, as shown in Figure 5.3. Table 5.1 provides the coordinates for the edges of the model space, which can be seen in Figures 2.1 and 2.2 as the red rectangle. The longitude of these coordinates ranges from about 26.30° to 30.50°E, and the latitude ranges from about 40.20° to 41.20°N.

Table 5.1. The coordinates of the ground surface vertices used for the 3-D Marmara model.

Vertex No	Latitude (°N)	Longitude (°E)	UTM 35 Easting (m)	UTM 35 Northing (m)	Depth (m)
1	40.197921	26.306482	440972.500000	4449955.500000	24.153866
2	41.251069	26.295462	440972.500000	4566868.000000	137.120377
3	41.198385	30.552717	797916.812500	4566868.000000	-90.836754
4	40.147146	30.497283	797916.812500	4449955.500000	792.099853

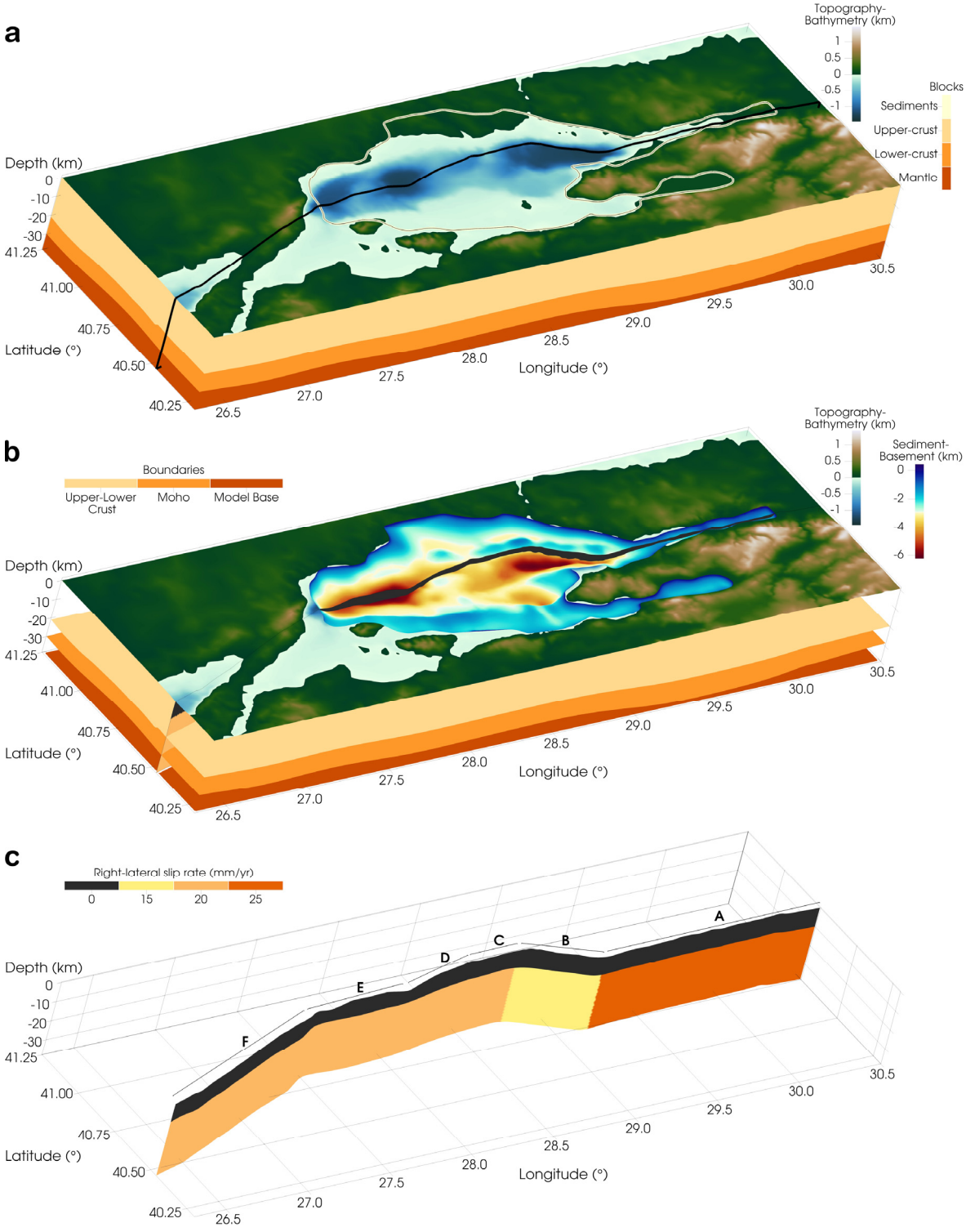

Figure 5.3. (a) A 3-D model of the Marmara made with real topography-bathymetry from Olson *et al*. (2014) separated by the MMF. The layers of the 3-D model are made up of blocks of sediment, the upper and lower crusts, and the mantle. (b) Model boundaries and the base of the sedimentary layer. (c) The MMF fault surface with slip rates comprising east-west lettered 6 segments.

A total of over 22 million tetrahedral elements make up the 3-D heterogeneous layered model of the 3-D research area, while over 18 million elements make up the homogeneous model. The tetrahedral element edge length is around 600 m, although their sizes may change significantly based on how close they are to the topographic complexity and fault zone. The reason for the increase in the total mesh number for the heterogeneous model is that the mesher produces a greater number of meshes as the heterogeneous model has more layers. In order to inspect whether this difference in the element numbers affects the results, we used both meshes to make GNSS model estimates for a homogeneous elastic model with a 10 km locking and compared the estimated velocities at the GNSS sites. The fact that the estimated velocities are nearly exactly the same as given in Figure 5.4 suggests that the 18 million meshes are sufficient to compute the deformations correctly for a completely homogeneous elastic material.

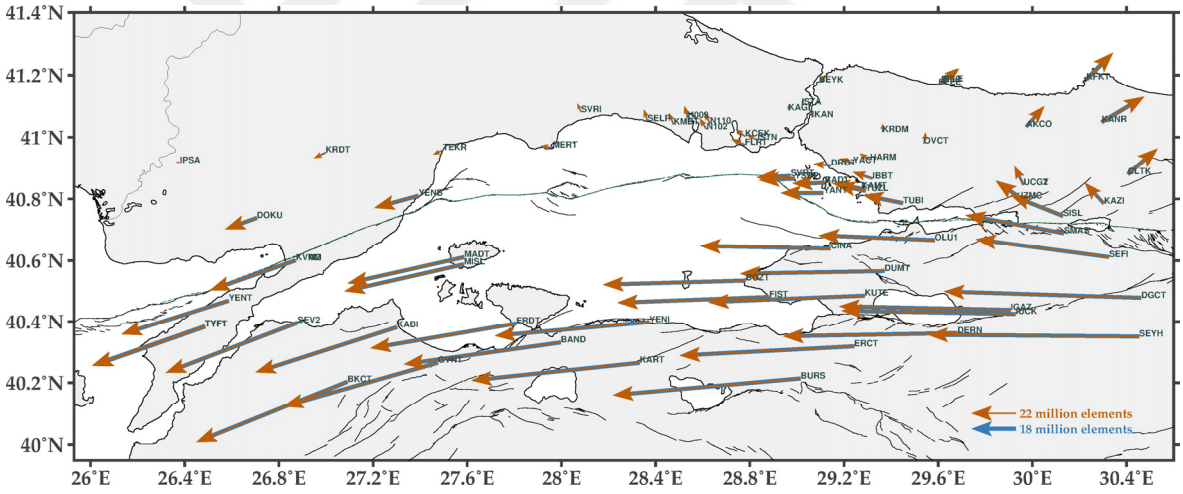

Figure 5.4. A comparison between the blue vectors of the model with 18 million elements and the orange vectors of the model with 22 million elements. All vectors are computed at GNSS stations from the models with a 10 km fixed locking depth in a homogeneous medium.

The MMF's 3-D fault model was adapted from Hergert *et al.* (2011), which describes the region as located between the longitudes of 27.25°E and 30.25°E. Using fault maps from prior research (Armijo *et al.*, 2002; Carton *et al.*, 2007; Cormier *et al.*, 2006) as well as seismic reflection data from previous studies (Bécel *et al.*, 2009; Carton *et al.*, 2007; Laigle *et al.*, 2008; Parke *et al.*, 2002), Hergert *et al.* (2011) made a 3-D model of MMF.

Considering we select a broader model domain dimension than the one Hergert *et al.* (2011) used for the Marmara Region in the direction of east-west, we extend the on-land part of the fault model further to the east and west from Turkey's official active fault map prepared by the Mining Research and Exploration Agency (Emre *et al.*, 2013).

5.5. Fault Slip Rates and Boundary Conditions of the Model Domain

We utilize a kinematic method in order to compute the surface velocity vectors and apply velocity boundary conditions to all of the side surfaces and the base of the model space by interpolating GNSS velocities relative to the Eurasian fixed reference frame illustrated in Figure 5.5.

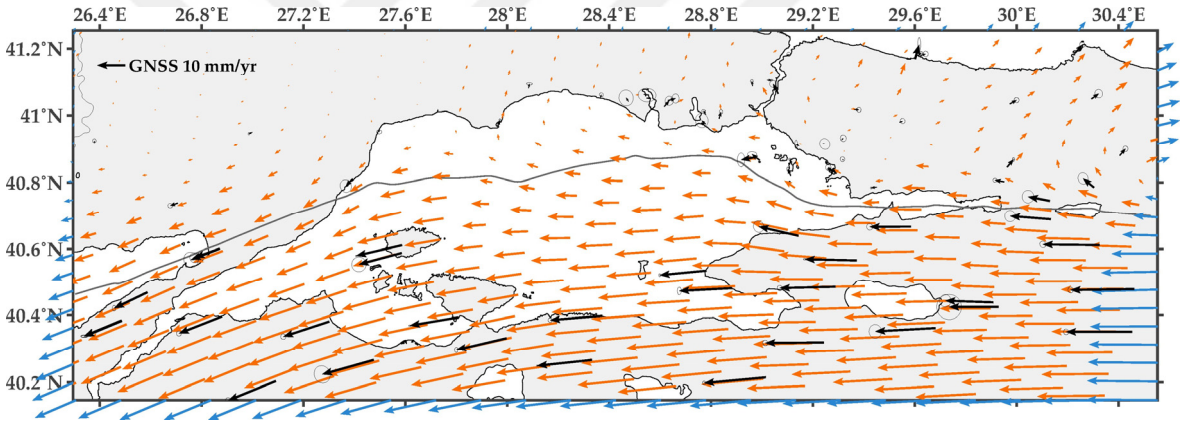

Figure 5.5. Bottom boundary conditions represented with orange vectors and side boundary conditions with blue vectors interpolated from Eurasia fixed GNSS data (Ergintav *et al.*, 2014) shown with black vectors.

The surface of the fault is likewise an inner boundary in our method, and the rate of fault slip is prescribed and enforced as a velocity boundary condition for the unlocked parts of the fault. On the other hand, the rate of slip for the locked parts of the fault is always set to 0 mm/yr throughout the analysis. At the beginning of the process, we experimented with two different ranges of values for the fault slip rates. When calculating the slip rates on the faults, Hergert and Heidbach (2010) relied on a finite element technique where the faults are freely sliding and estimated the fault slip rate along the faults in the whole of the Marmara region. Another study by Ergintav *et al.* (2014) employed GNSS velocity profiles

to find the rate of slip on MMF. According to findings by Ergintav *et al*. (2014), fault slip rates for the Princes' Islands section are estimated to be 15 mm/yr, whereas the slip rates for other sections range from 20–25 mm/yr. This is somewhat higher than Hergert and Heidbach's estimations of 15–18 mm/yr since they find higher slip rates on faults that are located south of the MMF. Our preliminary tests reveal that Ergintav *et al*. (2014)'s higher slip rate estimates match the data better, and these values are quite similar to the slip rate values of earlier studies by Meade *et al*. (2002).

We utilized the profile borders that were established by Ergintav *et al*. (2014) to impose the slip rates on each section, but we additionally separated the Central Marmara segment into more segments to understand the MMF's interseismic behavior in more depth.

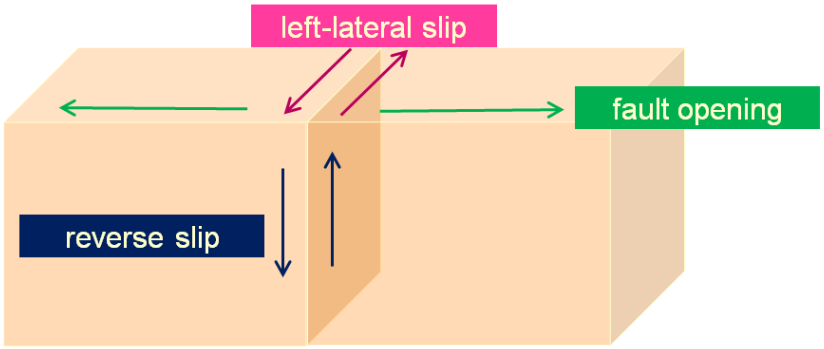

Figure 5.6. Fault slip sign conventions of PyLith, where left-lateral, reverse, and fault-opening movements have positive values.

Table 5.2. MMF segment slip rates and boundary locations employed for this study.

Segment	Name	West and East Boundaries (Lat°N–Lon°E)	Left-lateral (mm/yr)	Opening (mm/yr)
A	İzmit	40.72–29.20/40.70–30.53	-25	0
B	Princes' Islands	40.87–28.80/40.72–29.20	-15	6
C	Kumburgaz	40.87–28.49/40.87–28.80	-20	0
D	Central Marmara	40.80–28.04/40.87–28.49	-20	0
E	Western Marmara	40.77–27.41/40.80–28.04	-20	0
F	Ganos	40.46–26.30/40.77–27.41	-20	0

Figure 5.3c and Table 5.2 (see Figure 5.6 for sign conventions) show the imposed segment borders, which are set according to the relative strike of the fault geometry and provide the slip rates for each boundary.

5.6. The Elastic Properties of the Model Domain

We employ many alternative sets of material properties for the layers that are used in the modeling, all of which are provided in Table 5.3, so that we can examine how the velocity structure heterogeneity affects our results. All of our models are employing the same slip rates and the same 3-D fault geometry in this study.

As a starting point, we employ elastic homogeneous models that have average densities and velocities of P and S waves (Hergert *et al*., 2011) as a point of comparison to see whether heterogeneous features, such as basins, affect the accumulation of strain or interseismic coupling inferences. Table 5.3 (Bassin *et al*., 2000; Hergert *et al*., 2011) shows the values that were used for the heterogeneous models that have layers of the mantle, upper crust, lower crust, and sedimentary basins.

Table 5.3. The elastic properties of the materials employed in the homogeneous model and heterogeneous model layers (Bassin *et al*., 2000; Hergert *et al*., 2011; Rodriguez-Suarez, 2005).

Property	(HM) Homogeneous	(HT) 3-D Heterogeneous						
		Sedimentary Layer				*Upper Crust*	*Lower Crust*	*Mantle*
		Sediments (S)	*Soft Sediments (SS)*	*Overburden (O)*	*Hard Sediments (HS)*			
V_p (m/s)	5630.1	2701.0	2500.0	2800.0	4400.0	6100.0	6600.0	7385.5
V_s (m/s)	3250.5	1297.5	1200.0	1165.0	2500.0	3500.0	3800.0	4264.0
Density (kg/m^3)	2650.0	2200.0	2100.0	2400.0	2500.0	2750.0	2900.0	3300.0
E (GPa)	70.0	10.0	8.1667	9.0901	39.4260	84.5292	104.8626	150.0
v	0.25	0.35	0.3503	0.3953	0.2616	0.2546	0.2521	0.25

We make use of the 3-D basin model that was developed by Hergert and Heidbach (2010) and Hergert *et a*l. (2011). This model was derived from a number of studies of seismic surveys done in the Marmara Sea (Bécel *et al*., 2009, 2010; Carton *et al*., 2007; Laigle *et al*., 2008). The SRTM15 bathymetry and topography model developed by Olson *et al*. (2014) is used to build the 3-D topographic surface in our model. Both the boundaries of the upper-lower crust and the Moho, which have variable depth within the model domain, are derived from Kende *et al*. (2017), obtained from inversion of gravity anomalies.

Elastic parameters of the sedimentary basin were obtained from Hergert and Heidbach (2010)'s average values for Marmara Sea sediments. As shown in Table 5.3, we also experimented with different additional values depending on the sedimentary structure categories like overburden (Rodriguez-Suarez, 2005), soft sediments, and hard sediments (Bassin *et al*., 2000) to find out how this selection affects our findings.

5.7. The Measure of the Misfit

We do not try to solve for the fault surface coupling coefficients (Klein *et al*., 2017), taking into account the inadequate geodetic data resolution. Instead of finding these coefficients, we make the assumption that each fault section is either fixed at a locking depth that we optimize or is creeping at the plate rate. When testing the different locking depths for all fault sections, both homogeneous and heterogeneous elastic models are used. These models are abbreviated in the tables as HM and HT, respectively. Next, we compute the ground surface velocities at the GNSS stations. Then, we compare the misfits to the GNSS velocity data to find the model that fits the data best.

The distribution of locking depth throughout the MMF is optimized using a two-step process. Process one is to use the profile boundaries and segment orientations specified in Figure 5.3c and Table 5.2 to compute fault-parallel velocities, as done by Le Pichon *et al*. (2005) and Ergintav *et al*. (2014). Using Equation (5.1), we next compute the misfits based on fault-parallel velocities.

$$E_{RMS} = \sqrt{\frac{1}{nsta}\sum_{i=1}^{nsta}\frac{\left[d_p^i - p_p^i\right]^T\left[d_p^i - p_p^i\right]}{\left[\sigma_p^i\right]^2}} \tag{5.1}$$

Fault-parallel projections of velocity data and model estimates at the GNSS site i for each segment are shown as d_p^i and p_p^i in the equation, respectively. The 1–σ data uncertainty for the fault-parallel direction is denoted by σ_p^i. The profile method does not take into account the 3-D impacts of the fault geometry and hence has a tendency to fail at the segment edges or in areas where the interseismic fault behavior significantly varies.

First-order locking depth estimates for each segment are obtained using Equation (5.1). This method is also used to set the best-fitting locking depths of the İzmit and Ganos sections, which are shown in Figure 5.3c as segments A and F, that constitute the model's eastern and western boundaries, respectively. Since we know that these two sections are locked, we utilize this simple method to set locking depths for those sections. This lets us optimize fewer parameters during the grid search for the sections from B to E that lie below the Marmara Sea, as shown in Figure 5.3c.

To achieve the final best-fitting model, we conducted a grid search to determine the optimal locking depth for each segment that lies under the Marmara Sea. Due to the fact that we use a 3-D heterogeneous structure and fault model, we use Equation (5.2) to compute the misfits between the entire horizontal velocity data and model predictions as follows:

$$\chi_r^2 = \frac{1}{2nsta-1}\sum_{i=1}^{\text{nsta}}\begin{bmatrix} d_n^i - p_n^i & d_e^i - p_e^i \end{bmatrix}^T [C_d]^{-1}\begin{bmatrix} d_n^i - p_n^i & d_e^i - p_e^i \end{bmatrix}, \tag{5.2}$$

d^i represents the ith station's horizontal velocity data, p^i is the predicted horizontal model prediction, and

$$[C_d] = \begin{bmatrix} \sigma_E & \rho_{EN} \\ \rho_{EN} & \sigma_N \end{bmatrix}, \tag{5.3}$$

$[C_d]$ represents the data covariance matrix (for the values see Table A.1 in Appendix A). The east and north components of the horizontal vectors are denoted by the subscripts e and n, respectively.

6. FORWARD MODELING RESULTS FOR MARMARA GROUND DEFORMATION

6.1. A Constant Locking Depth Grid Search for the Main Marmara Fault

As a preliminary step in this part of our study, grid search of constant locking depths between 0 and 20 km are done throughout all MMF's segments in both homogeneous and 3-D heterogeneous media, as shown in Figures 6.1 and 6.2, respectively. Then, the best-fitting locking depth for each individual section is estimated.

Figure 6.3a displays the GNSS velocity data as well as the fault-perpendicular profiles and their boundaries. Figures 6.3b and 6.3c show fault-parallel model estimates of fixed locking depths between 0 and 20 km over the whole MMF, with calculations performed at 2.5 km depth intervals in both elastic 3-D homogeneous and heterogeneous structures. In addition, Figures 6.3d and 6.3e show the misfits of these profiles in both homogeneous and heterogeneous media. Profiles A and F, which correspond to the Gulf of İzmit and the Ganos sections, show clear evidence of considerable strain accumulation, as shown in Figure 6.3. Since the measurements are rather far from the MMF, as predicted, there is less constraint on segments under the Marmara Sea (Klein *et al*., 2017).

However, in order to get a preliminary assessment of the interseismic locking behavior, we computed the best-fitting locking depth for each segment by comparing the misfits shown in Figures 6.3d and 6.3e. Based on the misfits from east to west, the homogeneous model suggests locking depths of 5 km for sections between A and D, whereas the heterogeneous model suggests 7.5 km for sections A, B, and C and 10 km for D. When 3-D homogeneous and heterogeneous models are compared, it becomes clear since the sediments seem to localize strain to some extent and using a homogeneous half-space leads to an underestimation of the locking depth. Due to the distance of the coast on either side of the fault, it is difficult to impose any constraints on the interseismic behavior of segment D, which is the Central Marmara section. According to the findings of both the homogeneous and the heterogeneous models, the best explanation for the fault-parallel velocities in segment E is a fully creeping fault, including the Tekirdağ Basin, Western

High, and west of the Central Basin, while a locking depth of 7.5 km is shown to be the most appropriate for segment F, which is the Ganos section.

6.2. Models with Varying Locking Depths and the Best-Fitting Model

After completing the models with a fixed locking depth throughout the whole MMF, we move on to the models that have different locking depths in each segment to optimize the locking depth distribution beneath the Sea of Marmara. Because the İzmit and Ganos segments (segments A and F in Figure 6.3) clearly exhibit behavior that is very indicative of being locked, and the locking behavior is relatively well-constrained since these two segments have sufficient stations onland that are close to the fault. Hence, in order to decrease the number of parameters to explore, we set the locking depths for these two segments at 7.5 km, as derived by the fault-perpendicular profiles in the previous Section 6.1. Due to the complexities of the segments under the Marmara Sea from B to E, we carried out a grid search at 0, 5, and 10 km locking depths in order to find out which locking depths were best for these segments.

In this part of our study, we use Equation (5.2) to figure out the misfits from the horizontal geodetic velocities. It is a better approximation than Equation (5.1) because it takes into account the velocity vector orientations and it is not necessary to define profiles and associate GNSS stations with these profiles. This is especially problematic where the interseismic behavior and the fault geometry change significantly. To get a more sensitive misfit for the MMF's interseismic behavior under the Marmara Sea, we only used stations between the longitudes of 27.2°E and 29.2°E that were less than 20 km from the MMF. In order to minimize large coverage gaps, four additional stations (SELP, SVRI, MISL, and MADT) were included within 20-30 km of the MMF, resulting in a total of 21 sites. Table C.1 in Appendix C lists all 81 models and their misfits.

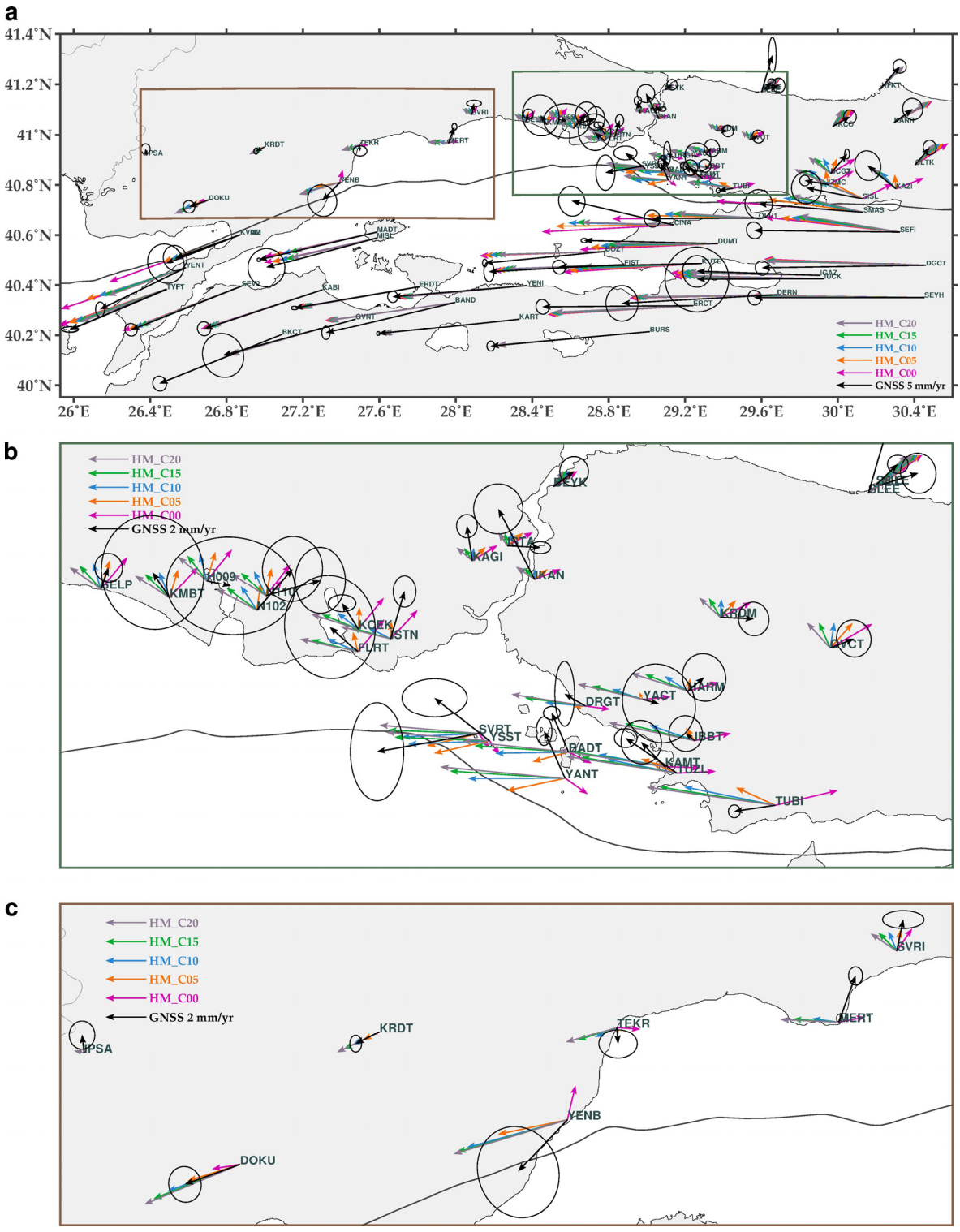

Figure 6.1. Model estimations at GNSS sites for fixed locking depths between 0 and 20 km in an elastic homogeneous medium, tested against GNSS velocities for (a) over the whole Marmara, (b) Central Marmara (the zoom-in on the green frame in (a)), and (c) Western Marmara (the zoom-in on the brown frame in (a)).

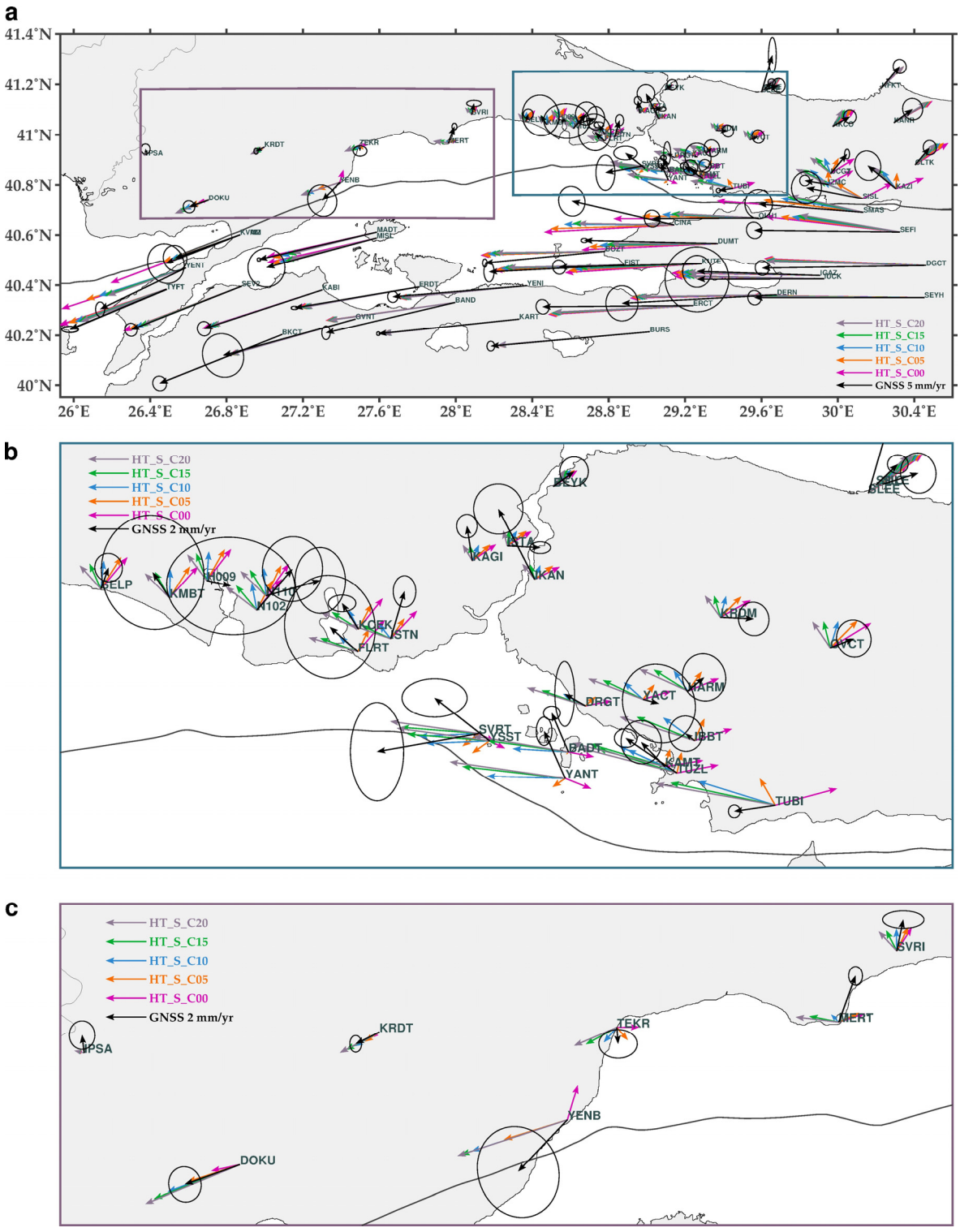

Figure 6.2. Model estimations at GNSS sites for fixed locking depths between 0 and 20 km in an elastic 3-D heterogeneous medium, tested against GNSS velocities for (a) over the whole Marmara, (b) Central Marmara (the zoom-in on the navy frame in (a)), and (c) Western Marmara (the zoom-in on the purple frame in (a)).

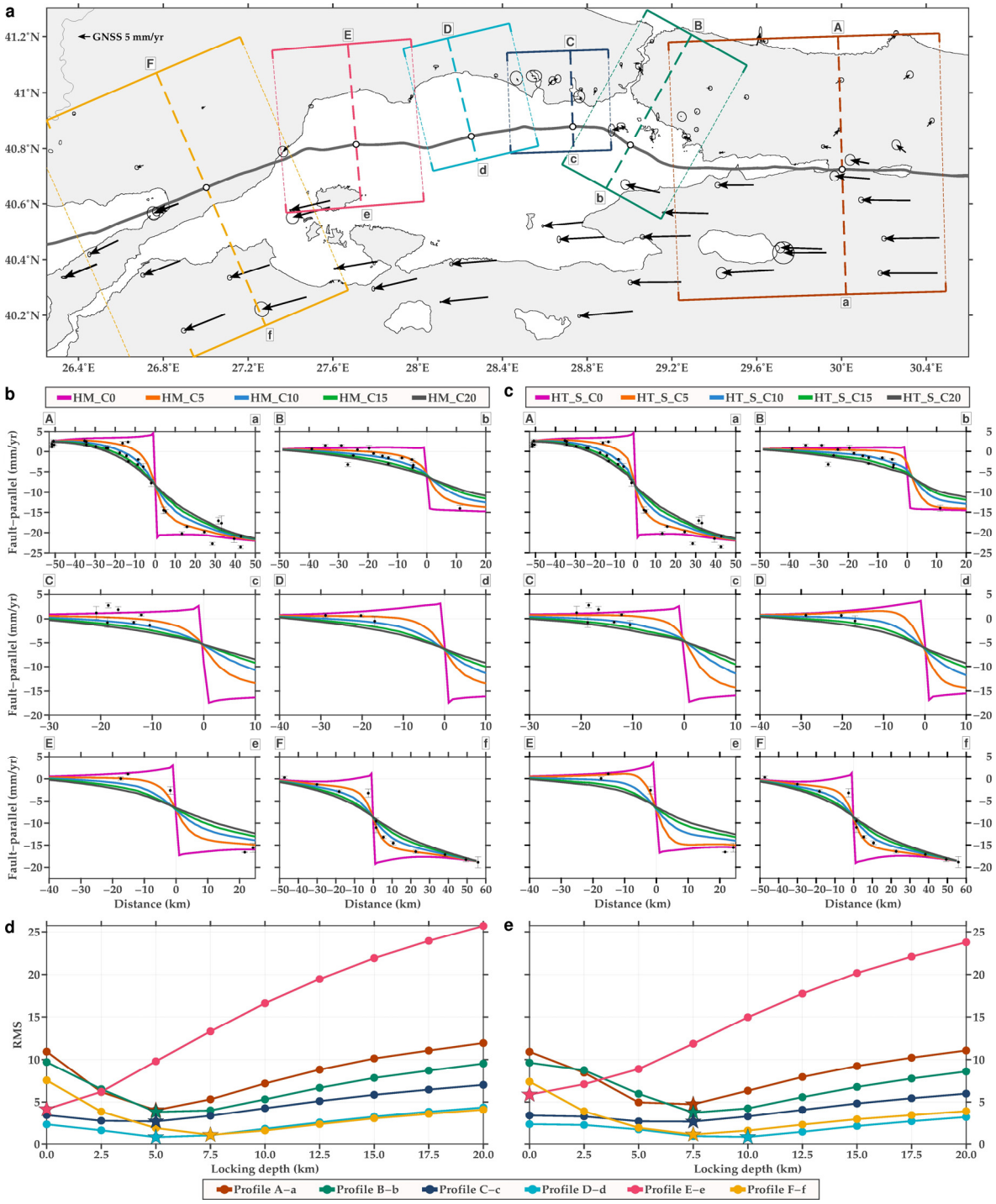

Figure 6.3. (a) Observed GNSS velocities shown by black arrows, profile boundaries indicated in a variety of colors for each segment, and GNSS stations that are in these profile zones, which are also listed in Table B.1 in Appendix B. (b) Fault-parallel GNSS velocities shown as black circles with error bars and model estimates along the profiles shown as solid lines for locking depths between 0 and 20 km in a homogeneous elastic medium and (c) in a 3-D heterogeneous elastic medium. (d) The weighted RMS misfits calculated within each profile zone using Equation (5.1), shown with the identical profile colors in (a) employing locking depths using a grid space of 2.5 km in a homogeneous structure and (d) in a 3-D heterogeneous structure.

The histogram distribution of χ_r^2 misfits ranging from 4.4 to 8.1 for the 21 sites that are located in close proximity to the MMF is shown in Figure 6.4a. On the basis of the misfit value distribution, we make the assumption that the 27 models with misfit values of less than 5.1 are those that fall within the first two bins of the histogram, which reflect the cluster of best-fitting models.

Figure 6.4b shows how the locking depths of 27 acceptable models are distributed throughout each segment. The pattern is similar to that derived previously from fault-perpendicular profiles, indicating that segment E of the Western Marmara portion is most likely to be unlocked. The remaining three sections under the Marmara Sea are more difficult to specify. Still, a 5–10 km locking depth is more realistic for Central High, which is segment D, than a scenario in which the fault is completely creeping. While section C seems to have fewer constraints, it is likely that the locking depth of the Princes' Islands, segment B, is 5 km.

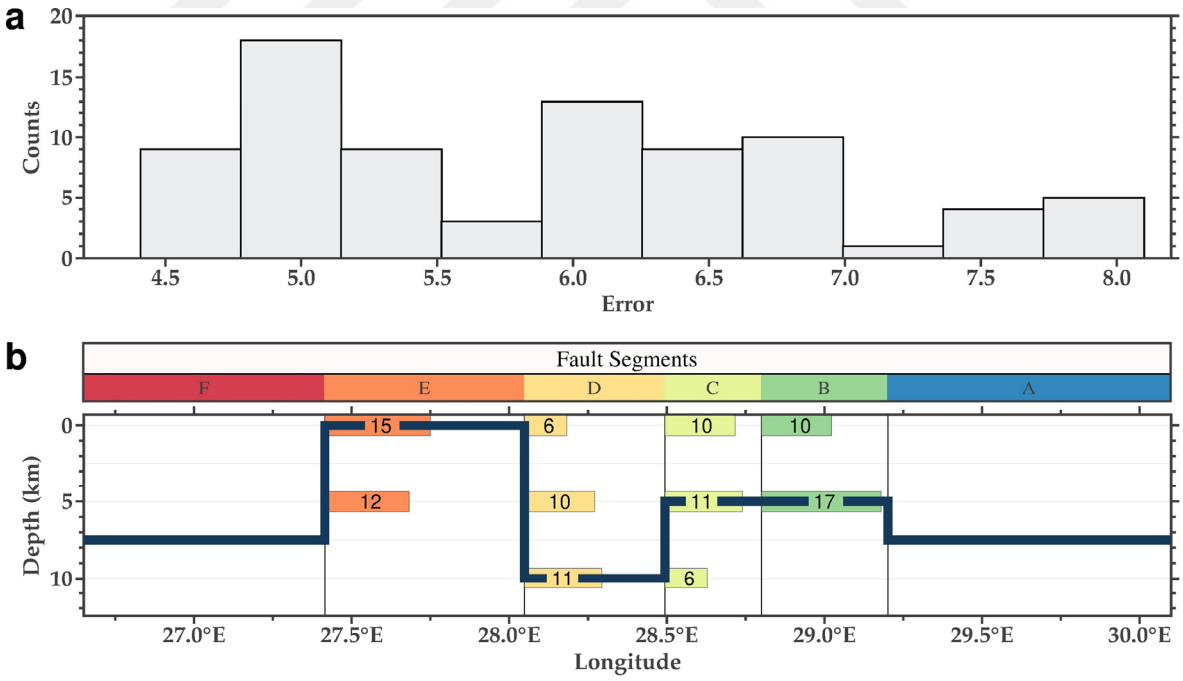

Figure 6.4. (a) Histogram distribution of χ_r^2 misfits from the locking depth grid search for the Marmara Sea segments B to E in Figure 5.3c based on 21 GNSS sites near the MMF. (b) The distribution of locking depths for 27 accepted $\chi_r^2 \leq 5.1$ models, represented by bars of the same color as the relevant segments, and the best-fitting locking depth for each section, shown by a thick navy line.

Figure C.1 in Appendix C displays the same analysis utilizing all 76 GNSS sites in the research region with the modified covariance matrices, whereas Figure C.2 displays the distribution of misfits using the covariance matrices that were originally reported. The results of accepted models and the best-fitting models both provide distributions of interseismic locking that are very similar to one another, as shown in Table C.1 in Appendix C. The differences in misfit values between the different interseismic models are lower when all stations are taken into account, which is the fundamental distinction. The main reason for this is that most stations are not situated within an adequate distance to the parts of the MMF under the Marmara Sea and are unable to detect changes in interseismic fault behavior.

We constructed 36 additional models using a 2.5-km grid around the best-fitting models for fault sections C to E to get the final best-fitting model shown in Table C.2 of Appendix C. According to the findings, segment C's locking depth is not well constrained but the locking depths of the other segments are constrained to some degree. The offshore acoustic data that was gathered over a 2.5-year period by Lange *et al*. (2019) also demonstrates that the fault along the Central High is locked at the surface, which runs along the border between sections C and D, giving additional proof that these are locked sections. The locking depth of section C is about the same as that of section B, mainly because it results in one of the smallest residuals and the findings of the submarine geodetic survey.

In Figure 6.4b, the thick navy line represents our final best-fitting model. Segments A to D of the MMF, stretching between İzmit and the east of the Central Basin, are locked. In the west, segment E of the Western Marmara is completely creeping, while segment F of the Ganos section is locked down to a depth of 7.5 km.

Considering that estimates for sections B and C are near to the average grid point, we computed the mean and standard deviation to provide an approximation of the uncertainty of locking depth estimates for these two segments. For sections B and C, the calculated mean and standard deviation are, respectively, 3.15±2.41 km and 4.26±3.78 km. Because of this, we infer that the estimations might be off by about 3 km.

In the Central and Eastern Marmara, it is harder to figure out the exact details of interseismic coupling, while the locking distribution can be more tightly constrained in the Western region of the Marmara. Based on the best-fitting models, it becomes clear that there is a low coupling to high coupling transition between the Western Marmara and Ganos segments.

In particular, our goal was to find the location of this transition point from the creeping section E of the Western Marmara segment to the locked section F of the Ganos segment. By moving the transition point along the fault by 5 km in a systematic manner, we were able to calculate the model estimates at the neighboring GNSS sites, as shown in Figure 6.5. The best-fitting transition from the Western Marmara segment to the Ganos segment happens precisely at the restraining bend at about 27.41°E longitude, shown in Figure 6.5 by the cyan circle, where the MMF curves 18° southward (Seeber *et al*., 2004). Figures 2.3a and 6.5 also show that this transition is marked by numerous earthquakes both on and off the MMF. This serves as further proof that there is a geometrical border between these two segments which is also characterized by a change in fault coupling behavior.

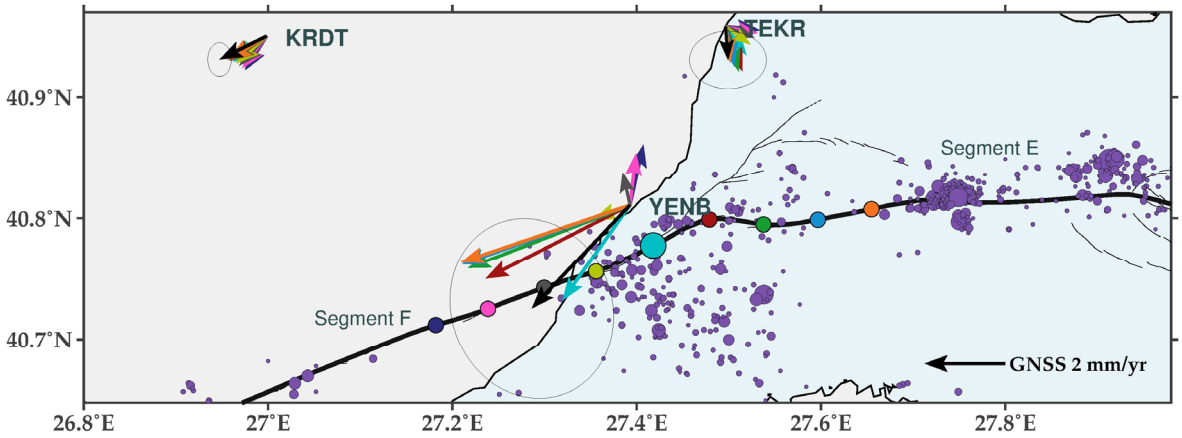

Figure 6.5. Optimization for the transition location between the fully creeping section E of the Western Marmara segment and the fully locked, extending down to a depth of 7.5 km, section F of the Ganos segment by comparing GNSS velocities displayed as black arrows against model estimates at neighboring GNSS stations, with the arrows of the same color as the relevant transition points, and the best-fitting transition point shown by a bigger cyan circle. The M ≥ 2 earthquake epicenters (Schmittbuhl *et al*., 2016b) are shown with purple circles. The black lines are the fault lines (Emre *et al*., 2013), whereas the bold black line is our model's MMF surface trace.

Figure 6.6 displays the best-fitting 3-D elastic interseismic model for homogeneous and heterogeneous media. When the 3-D heterogeneous structure is taken into account, the black sections illustrate the MMF's locked zones. The white lines represent the locking depth limits of the best-fitting model for an elastic medium that is homogeneous. We found that estimates of the locking depths made with a homogeneous elastic medium were lower than those made with a heterogeneous elastic medium. There is also a strong correlation between the creeping zone location and the distributions of repeating earthquakes and a high rate of seismicity, as shown in Figure 6.6.

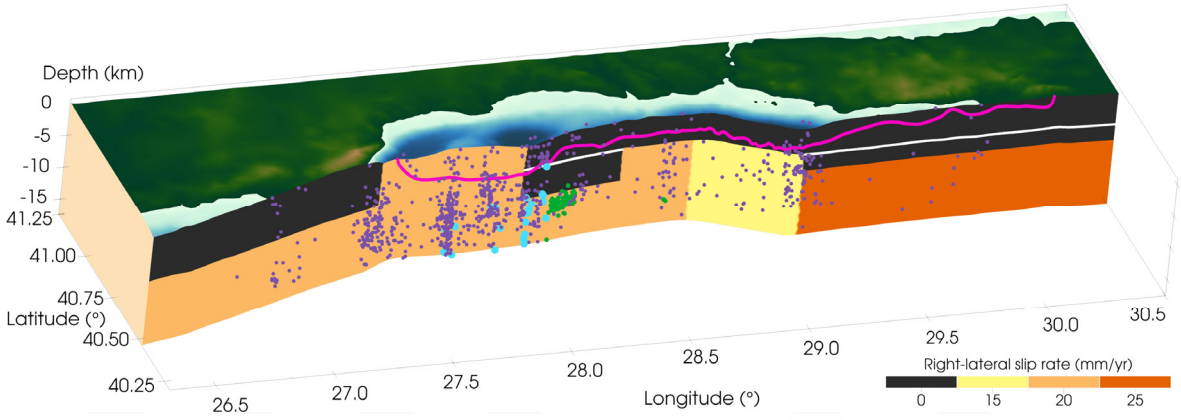

Figure 6.6. The 3-D Marmara Region model and MMF, along with the best-fitting locking depth distribution and interseismic slip rates. In our 3-D heterogeneous best-fitting model, the locked parts of the fault are shown in black, while the white lines show the base of the shallower locking depth estimations made with a homogeneous model. The pink line is where the bottom layer of sediments cuts through the MMF. Seismicity located within 5 km of the MMF is shown as purple circles (Schmittbuhl *et al*., 2016b), the 2019 Silivri earthquake series as green circles (Karabulut *et al*., 2021), and repeating earthquakes as cyan circles (Schmittbuhl *et al*., 2016a; Uchida *et al*., 2019).

Figure 6.7 shows a comparison between the residual vectors of our 3-D heterogeneous best-fitting model (HT_S_VB) and those of models with a fixed locking depth of 10 km (HT_S_C10) and 15 km (HT_S_C15) along the whole MMF. Figure 6.8 shows the same comparison but for the zoom-in on the Eastern Marmara, particularly the İstanbul region and its surroundings. When there is a variation in the locking behavior of the Ganos section and the Tekirdağ Basin, the Western Marmara residuals are much lower.

The Eastern Marmara's residuals are greater, which is most likely due to the fault's distance from onshore stations as well as the fact that GNSS data may have greater uncertainties than reported. Even nearby GNSS stations, particularly on the Princes' Islands, exhibit conflicting vectors. This cannot be explained by fault coupling alone.

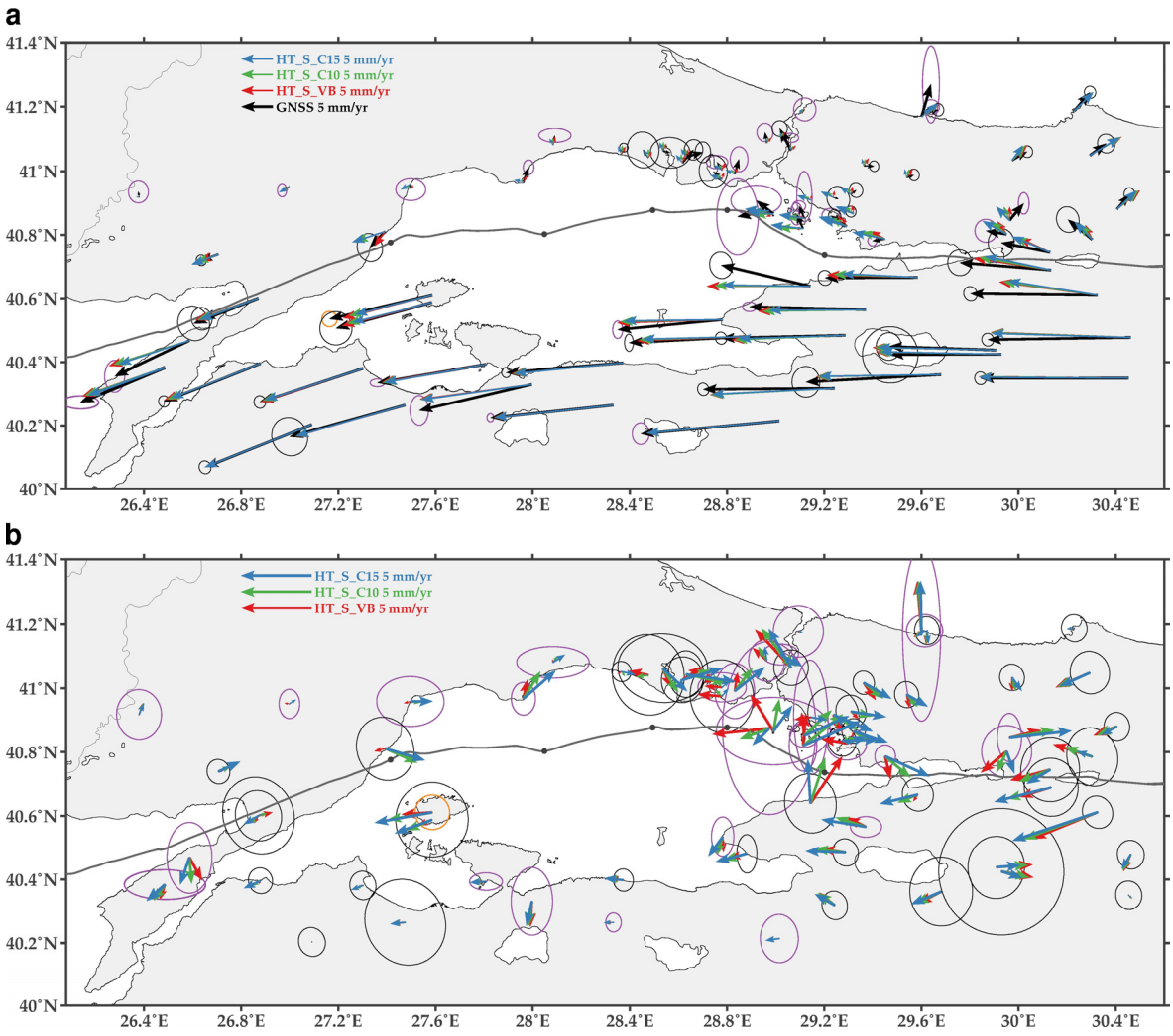

Figure 6.7. (a) Observed GNSS velocities (black arrows with error ellipses of 95%) in comparison to estimates made in heterogeneous media with the HT_S_VB best-fitting model (red arrows), HT_S_C10 fixed to a 10 km locking depth model (green arrows), and HT_S_C15 fixed to a 15 km locking depth model (blue arrows). The error ellipses in purple represent continuous stations with uncertainties multiplied by a factor of 2.5, while the error ellipse in orange represents a station with uncertainties multiplied by a factor of 5. (b) Residuals calculated by subtracting model estimates made with best-fitting locking (red), fixed at a 10 km locking (green), and a 15 km locking (blue) from GNSS velocities shown with 1-σ error ellipses.

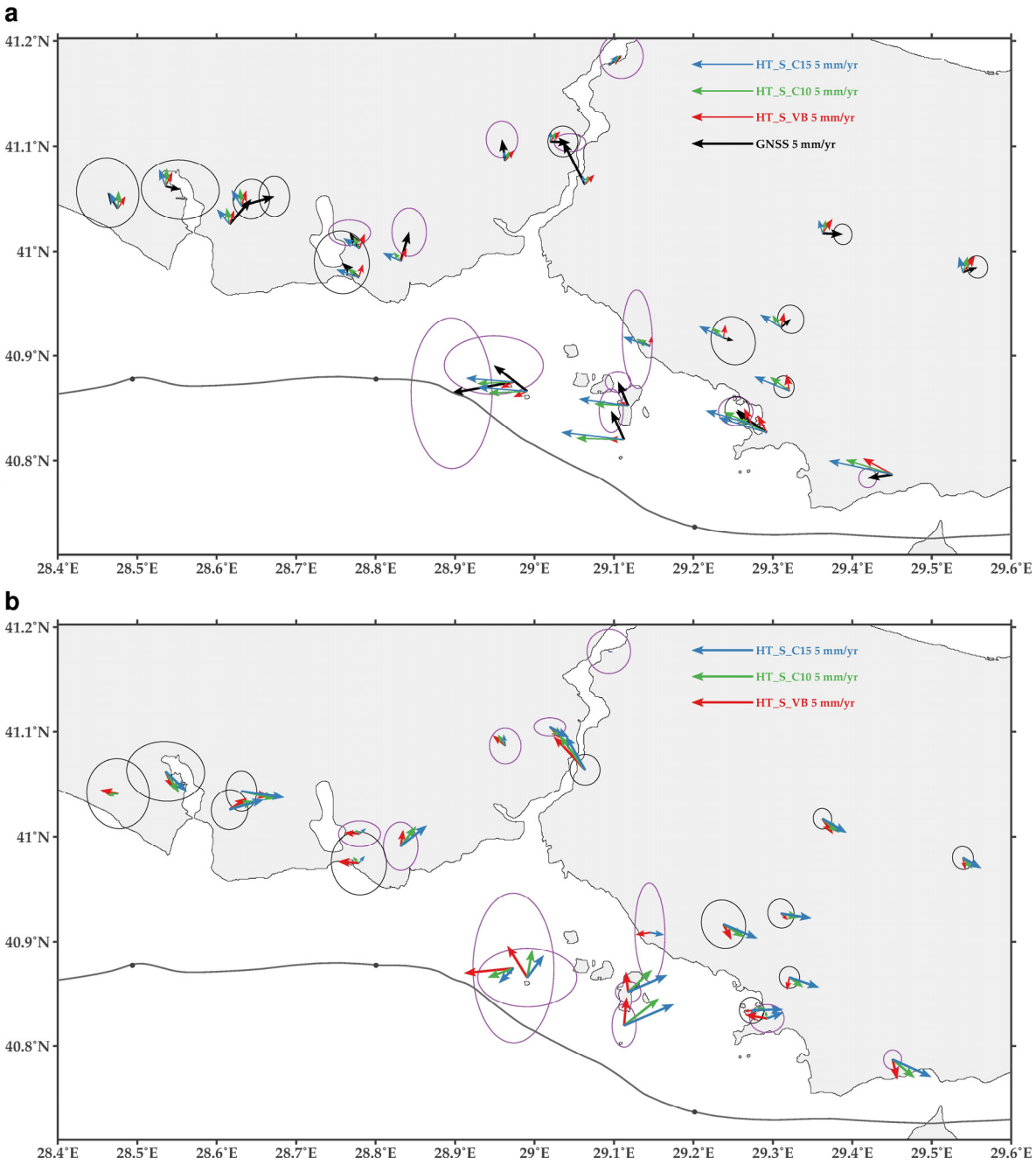

Figure 6.8. Zoom-in on the İstanbul region (a) observed GNSS velocities (black arrows with error ellipses of 95%) in comparison to estimates made in heterogeneous media with the HT_S_VB best-fitting model (red arrows), HT_S_C10 fixed to a 10 km locking depth model (green arrows), and HT_S_C15 fixed to a 15 km locking depth model (blue arrows). The error ellipses in purple represent continuous stations with uncertainties multiplied by a factor of 2.5, while the error ellipse in orange represents a station with uncertainties multiplied by a factor of 5. (b) Residuals calculated by subtracting model estimates made with best-fitting locking (red), fixed at a 10 km locking (green), and a 15 km locking (blue) from GNSS velocities shown with 1-σ error ellipses.

6.3. The Effect of the Sedimentary Basins and Fault Coupling on the Strain Rate Distribution

The presence of sedimentary basins may result in large variations in predictions of velocity and strain rate patterns even if the conclusions about interseismic motion do not dramatically vary. We computed the maximum shear at each mesh node by combining linearly the maximum and minimum eigenvalues of the strain rate tensor to figure out the conflicting impacts of the interseismic behavior and the deep sedimentary basins. In Equations (6.1) and (6.2), $\dot{\varepsilon}$ represents the maximum shear strain where $\lambda_{1,2}$ are eigenvalues of the strain rate tensor, ε_{ee} and ε_{nn} are the normal strains in the directions of east and north, respectively, and ε_{en} is shear strain acting on the ground surface.

$$\dot{\varepsilon}_{\mathrm{max}shear} = \frac{\lambda_1 - \lambda_2}{2} \tag{6.1}$$

$$\dot{\varepsilon}_{\mathrm{max}shear} = \sqrt{\left(\frac{\varepsilon_{ee} - \varepsilon_{nn}}{2}\right)^2 + (\varepsilon_{en})^2} \tag{6.2}$$

Figure 6.9 shows a comparison between the maximum shear strain rates of our best-fitting 3-D heterogeneous model (HT_S_VB) and those of models with a fixed locking depth of 10 km over the whole MMF in both homogeneous (HM_C10) and heterogeneous (HT_S_C10) mediums. Based on this comparison, it can be inferred that basins confine shear strain close to the fault under the Marmara Sea. Therefore, these basins must be incorporated to build an appropriate interseismic model.

Figure 6.10 shows a comparison between the calculated ground surface velocities of our best-fitting model (HT_S_VB) and the model with a fixed locking depth of 10 kilometers (HT_S_C10), both of which use the same 3-D heterogeneous structure. Most of the differences in ground velocities between these two models can be seen in the segments of Western Marmara and the Princes' Islands. On the other hand, the inland stations provide almost identical results for the remaining parts, which shows that these stations are relatively insensitive to interseismic coupling. This comparison clearly shows that unless we can measure interseismic strain rates beneath the sea, it is extremely challenging to put constraints on the fault behavior in the Central Marmara and Kumburgaz segments.

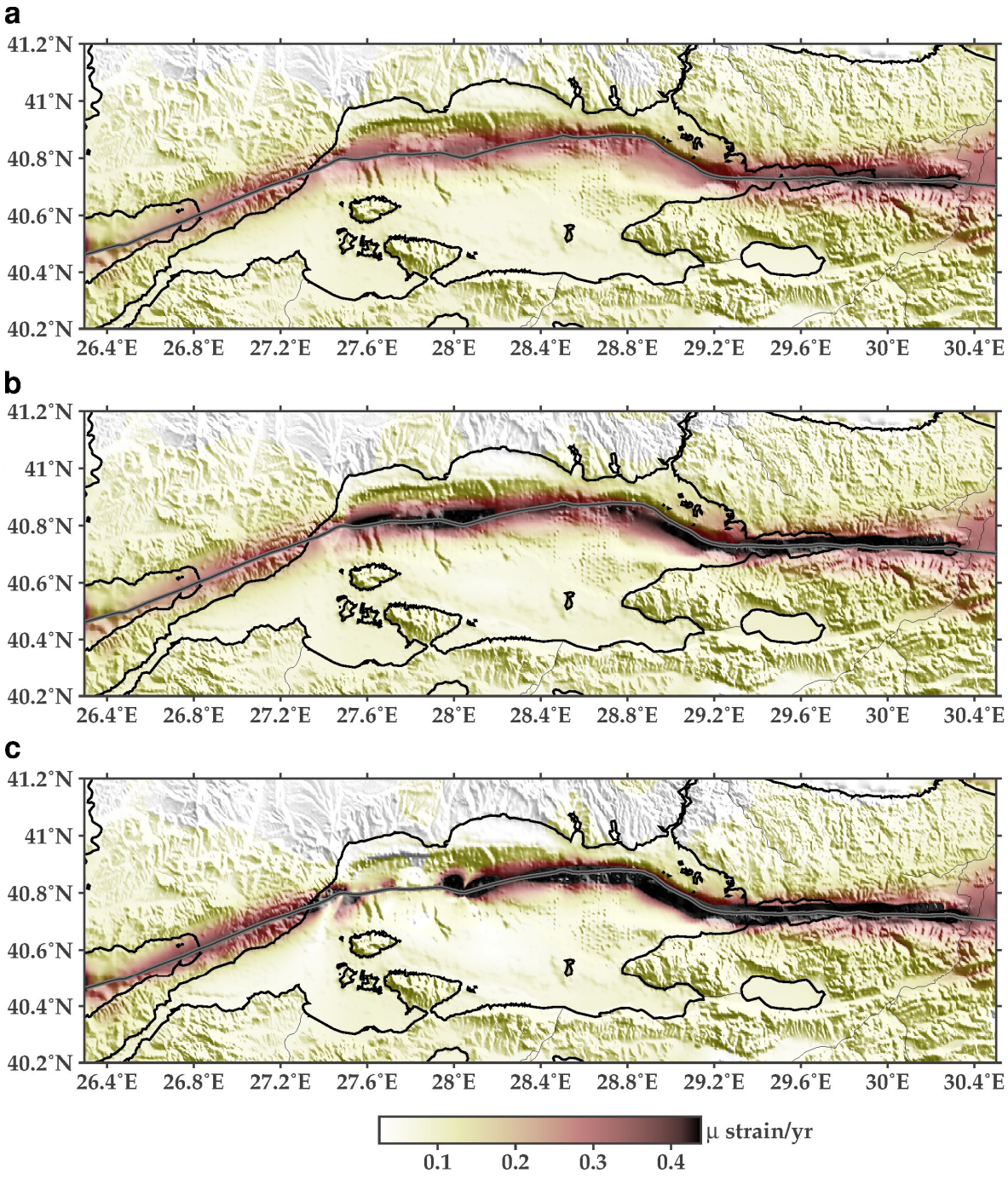

Figure 6.9. Ground surface maximum shear strain rate fields for (a) a homogeneous model with a fixed locking depth of 10 km (HM_C10), (b) a heterogeneous model with a fixed locking depth of 10 km (HT_S_C10), and (c) the heterogeneous best-fitting model (HT_S_VB).

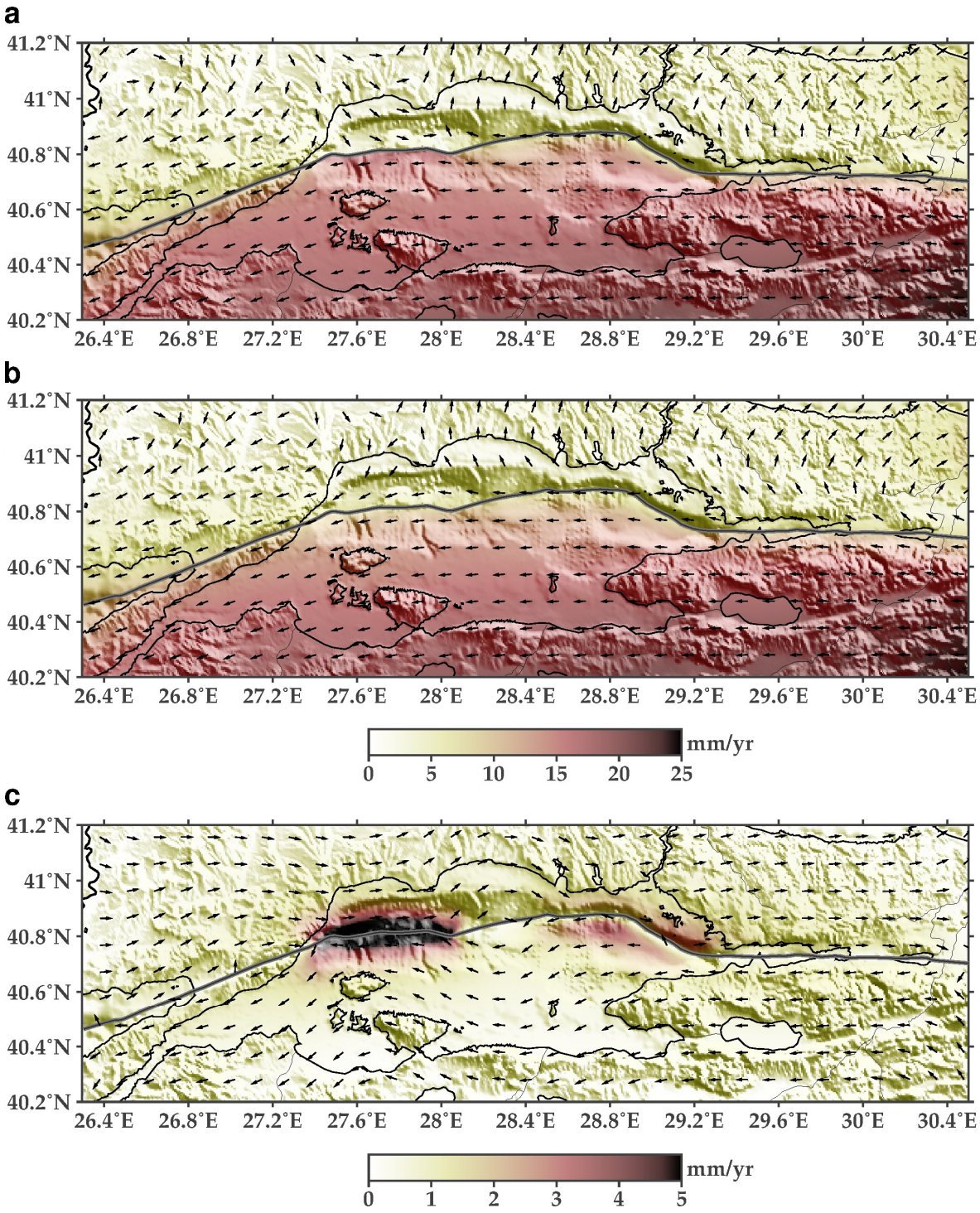

Figure 6.10. The ground surface velocities for the 3-D heterogeneous model with (a) the best-fitting locking depth (HT_S_VB) and (b) a fixed locking depth of 10 km (HT_S_C10). The colors and vectors show the magnitudes and directions, respectively. (c) The differences between these two models, HT_S_VB and HT_S_C10, with a saturation rate of 5 mm/yr.

6.4. A Comparison of Different Proposed Elastic Properties and Interseismic Locking Depths with the Best-Fitting Interseismic Model

In this part of the study, our best-fitting interseismic model employing the 3-D elastic heterogeneous structure is compared to several alternative scenarios of interseismic fault behavior proposed by the geodetic data or seismicity patterns, and elastic structures. As a point of reference, these models are also compared to models with the same locking throughout the whole fault. The scenarios that were analyzed are detailed in Table 6.1. Figure 6.11 displays the computed χ_r^2 misfits to the geodetic data for the 21 sites surrounding the MMF, while Figure 6.12 displays the misfits utilizing all of the available stations.

Table 6.1. Tested models named based on material compositions and locking depths (Yılmaz *et al*., 2022).

Model	Locking Type	3-D Material Structure	West-to-East Locking Depth of A-F Sections					
			F	E	D	C	B	A
HM_Vb	Best-fitting	Homogeneous	7.5	0.0	5.0	5.0	5.0	5.0
HT_HS_VB	Best-fitting	Heterogeneous Hard Sediments	7.5	0.0	10.0	5.0	5.0	7.5
HT_O_VB	Best-fitting	Heterogeneous Overburden	7.5	0.0	10.0	5.0	5.0	7.5
HT_SS_VB	Best-fitting	Heterogeneous Soft Sediments	7.5	0.0	10.0	5.0	5.0	7.5
HT_S_VB	Best-fitting	Heterogeneous Sediments	7.5	0.0	10.0	5.0	5.0	7.5
HT_LeP_VB	Best-fitting	Heterogeneous Soft sediments in the south Hard sediments in the north (Le Pichon *et al*., 2005)	7.5	0.0	10.0	5.0	5.0	7.5
HT_S_Sch	Schmittbuhl	Heterogeneous Sediments	See the blue curve in Figure 2.3b for the locking distribution (Schmittbuhl *et al*., 2016b).					
HT_S_Er	Ergintav	Heterogeneous Sediments	9.0	0.0	0.0	0.0	5.0	5.0
HM_CX	Constant	Homogeneous	X	X	X	X	X	X
HT_S_CX	Constant	Heterogeneous Sediments	X	X	X	X	X	X
HT_LeP_C10	Constant	Heterogeneous Soft sediments in the south Hard sediments in the north (Le Pichon *et al*., 2005)	10	10	10	10	10	10

"X" is the continuous locking depth that is present over the whole of the fault, and it can range anywhere between 0 and 20 km.

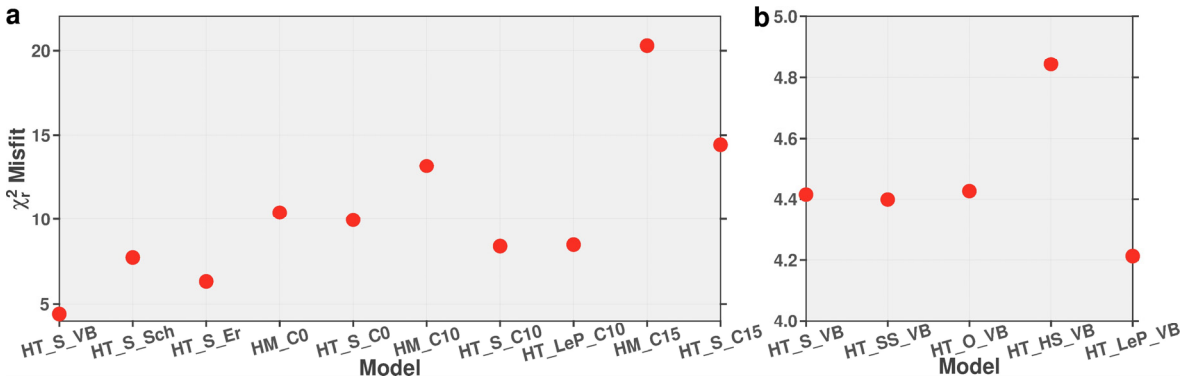

Figure 6.11. Geodetic misfits based on 21 GNSS sites near the MMF for the models (a) with different elastic properties of materials and locking depths and (b) with different sedimentary layer material properties (for model descriptions, see Table 6.1).

In the first step of our assessment, the misfits of the fixed locking depth models with homogeneous and heterogeneous 3-D elastic media were compared, and the results showed that the 3-D heterogeneous models provided better fits to the GNSS velocities in Figure 6.11a. The cases in which the fault is fully unlocked from İzmit all the way to the Ganos section (HT_S_C0; $\chi_r^2 = 9.95$) and the cases in which the entire MMF is completely locked down to a depth of 15 km (model HT_S_C15; $\chi_r^2 = 14.44$) both result in very high misfits and can be completely outruled. Although the fits are improved with a fixed locking depth of 10 km along the whole MMF (HT_S_C10; $\chi_r^2 = 8.40$), the model's performance is still significantly lower compared to that of our best-fitting model, which assumes that along the fault there is a variation in locking depths (model HT_S_VB; $\chi_r^2 = 4.41$).

Next, we check to see if the asymmetric sedimentary structure proposed by Le Pichon *et al.* (2003, 2005) provides enough explanation for the geodetic data on its own without any variations of the locking behavior. To construct models with a large contrast in rigidity across the fault, it is assumed that the sedimentary layers north of the main fault are composed of hard sediments and that the sedimentary layers south of the main fault are composed of the soft sediments specified in Table 5.3. For the sedimentary layers, this contrast means that there is about a 5-fold rigidity ratio across the fault. In spite of this being the highest rigidity contrast we can get utilizing realistic values for elastic sediments, it is still lower than the rigidity ratio of 10 proposed by Le Pichon *et al.* (2005), who also agree that a 10-fold rigidity ratio is quite large.

Model HT_LeP_C10 (χ_r^2 = 8.49), which has a rigidity ratio of about 5 for sedimentary basins across the fault and a locking depth fixed down to 10 km along the entire length of the MMF, close to the 10.5 km estimated value of Le Pichon *et al*. (2005), fits much less than our best-fitting interseismic locking model HT_S_VB (χ_r^2 = 4.41), particularly in the Western Marmara. This leads us to the conclusion that a plausible rigidity contrast by itself is not enough to explain the observed GNSS velocities.

In order to examine whether utilizing seismicity as an indicator for interseismic locking is an appropriate strategy, we examine the locking depth model suggested by Schmittbuhl *et al*. (2016b), shown with the blue curve in Figure 2.3b, and estimate the GNSS velocities using this model. The model HT_S_Sch (χ_r^2 = 7.74), which is based on Schmittbuhl *et al*. (2016b)'s locking distribution, does worse than our best-fitting geodetic model, but better than the fixed locking depth models. The locking variation pattern of Schmittbuhl *et al*. (2016b) is similar to that of our best-fitting geodetic model. However, the locking depths predicted by the seismicity are about 5 km deeper than those predicted by the geodetic model, resulting in lower geodetic data fits.

The last test is the model built based on the fault locking proposed by Ergintav *et al*. (2014). In this model, all the segments between the Ganos and Princes' Islands are unlocked (see Table 6.1 for model HT_S_Er). The misfit of this model (χ_r^2 = 6.31) is higher than that of the best-fitting model (χ_r^2 = 4.41), in which just the Western Marmara section is unlocked. Based on the results of this test, it seems that a shallow locked fault rather than a completely creeping fault is more likely to be found under the Eastern Central Basin and Kumburgaz segments, which are segments C and D, respectively.

Finally, we utilize four distinct kinds of sedimentary formations from Table 5.3 for our best-fitting locking depth model to see if the type of material has a big effect on geodetic misfits. In the misfit comparison shown in Figure 6.11b, the hard sedimentary HT_HS_VB model (χ_r^2 = 4.84) performs the worst. A somewhat better misfit than the symmetric models is produced when our previously acquired best-fitting locking depth model is combined with the asymmetric elastic model (model HT_LeP_VB, χ_r^2 = 4.21). This test reveals that interseismic behavior dominates the observed pattern. However, asymmetric strain buildup is a small contributor, with higher strain localized south of the

MMF. When all 76 GNSS sites in the Marmara area are taken into account in the test, it yields findings that are quite identical to those previously obtained (Figure 6.12).

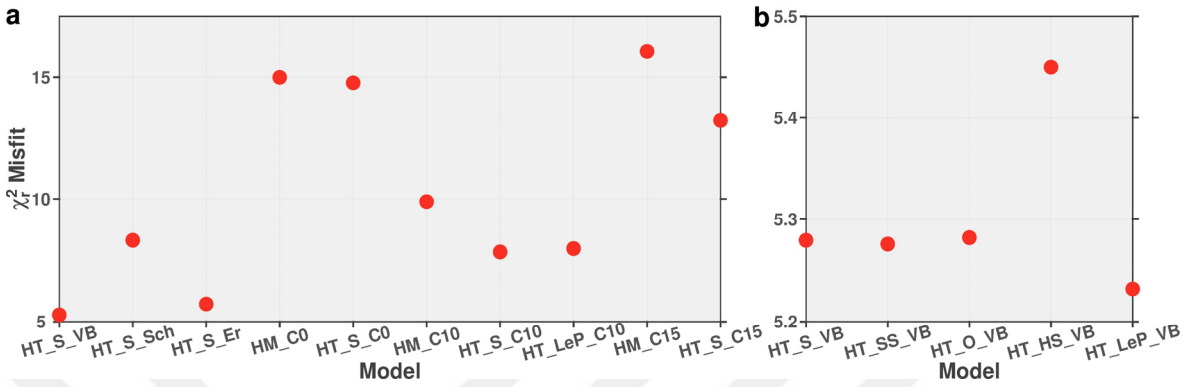

Figure 6.12. Geodetic misfits based on all 76 GNSS sites in the Marmara region for models (a) with different elastic properties of materials and locking depths and (b) with different sedimentary layer material properties (for model descriptions, see Table 6.1).

7. DISCUSSION

7.1. Interseismic Behavior and Structural Heterogeneity Along the Main Marmara Fault

In prior research, interseismic GNSS data sets that were very similar to the ones we utilized in this study were discussed in two different ways: one was in terms of the accumulation of asymmetric strain caused by deep sedimentary basins (Le Pichon *et al*., 2003, 2005), and the other was in terms of the interseismic locking behavior along the MMF (Bulut *et al*., 2019; Ergintav *et al*., 2014; Klein *et al*., 2017; Meade *et al*., 2002; Özbey *et al*., 2021). The results of geodetic surveys conducted offshore provided substantial proof of interseismic surface heterogeneity, although the impacts of deep basins on interseismic behavior were not well examined.

The goal of this section is to get a better understanding of the influence of both 3-D structures as well as heterogeneous interseismic coupling factors. This is done by comparing the ground surface strain rates obtained from homogeneous and 3-D heterogeneous models in which the fault is either fixed or has a variable locking. Figure 6.9 shows that the strain is localized south of the fault line near the Princes' Islands segment. This is because of both the fault bend that causes a restraining belt and the dips toward the south. Figure 2.3a also shows that the earthquakes are similarly localized south of the fault line in this region. On the other hand, the geodetic data, particularly in the Western Marmara, is insufficient to explain and evaluate the impacts of the basins since the on-land GNSS stations surrounding the segments further west of the Princes' Islands are not close enough to the fault. When the heterogeneous and homogeneous elastic models are compared, it is obvious that the models that incorporate basin effects result in a deeper locking depth, indicating that the heterogeneous structure influences the locking depth. Although it is not feasible to place strict limitations on the interseismic fault behavior in order to get a full coupling map, our findings demonstrate that the data, particularly in the Western Marmara, is well explained by the interseismic locking behavior.

When evaluating interseismic behavior, Ergintav *et al*. (2014) and Le Pichon *et al*. (2005) described profiles differently. This was mostly due to the Marmara Island GNSS stations, which impose constraints to the south of the fault. According to Le Pichon *et al*. (2005), the station MISL on Marmara Island belongs to the Western Marmara profile and supports the idea of asymmetric strain buildup, whereas stations MADT and MISL are both considered part of the Ganos segment profile by Ergintav *et al*. (2014), who evaluate them as evidence that the Ganos segment is locked.

A more effective approach is to consider the GNSS velocities as being a result of the deformation of a continuum with a heterogeneous elastic structure and 3-D fault geometry. This is because the medium itself is a continuum that has heterogeneities and the Marmara Island is located in close proximity to both the Western Marmara and Ganos sections of the MMF. The fit of our model to the Western Marmara stations is much improved, as shown in Figure 6.7. In this model, the fault is locked all along the Ganos section but is unlocked under the Tekirdağ Basin, Western High, and the west of the Central Basin. For the Princes' Islands and Kumburgaz segments, the fault coupling is harder to constrain (Figures 6.7 and 6.8). Our interseismic model with creep under the Western High and coupling under the Central High is compatible with the findings of Sakic *et al*. (2016), Lange *et al*. (2019), and Yamamoto *et al*. (2019) from submarine geodetic deployments and exhibits a very similar pattern.

Due to insufficient resolution, it is also crucial to highlight that we do not try to find the coefficients of the interseismic coupling on the fault surface. Yamamoto *et al*. (2019) observed creep at half the plate velocity, which is around 10 mm/yr for the Western Marmara stretch of the fault, where we found that this segment is fully unlocked. We find it more useful to concentrate on the interseismic behavior at the larger scales in our research than to employ surface measurements as a restriction.

Our fully elastic model ignores time-dependent or inelastic effects, which might be another element contributing to a complicated long-term velocity pattern, particularly in unconsolidated sediments. Throughout their 10 to 20-year observation time frame, however, continually measuring GNSS stations exhibit relatively consistent velocities with negligible temporal fluctuations, excluding seasonal signals (Ergintav *et al*., 2014). Even

though those inelastic effects might cause permanent deformation, it is expected that they are extremely minor in a seismic cycle and that the majority of the strain builds up elastically near the fault.

7.2. Interseismic Coupling, Distribution of Seismicity, and Repeating Earthquakes along the MMF

Recent studies indicate that seismic activity along the MMF is distributed heterogeneously (e.g., Schmittbuhl *et al*., 2016b), which is thought to be caused by interseismic coupling. As shown in Figure 2.3, the İzmit and Ganos sections have low seismicity along the MMF, whereas parts under the Marmara Sea have greater rates. Both the M_w 7.4 İzmit and M_w 7.2 Düzce earthquakes that occurred in 1999, which exhibited supershear rupture velocities (Bouchon *et al*., 2001; Konca *et al*., 2010), broke the section of low interseismic activity in the region. On the contrary, the M_w 6.9 North Aegean earthquake that occurred in 2014, which exhibited a slow rupture velocity of 1.5 km/s (Konca *et al*., 2018) and a very long source duration of 40–50 s and a source length of 90 km compared to its magnitude, ruptured further west of the Ganos segment and broke the section of high interseismic activity in the region.

Historical earthquakes (Ambraseys, 2002; Baştürk *et al*., 2017; Dikbaş *et al*., 2018; Meghraoui *et al*., 2012), which give additional evidence for the MMF's varying interseismic locking behavior, demonstrate that the Ganos and İzmit portions produce major earthquakes more frequently than the part of the fault under the Marmara sea.

In Figure 6.6, the relationship between high seismicity rate and low fault coupling along the major fault is rather noteworthy. When a heterogeneous medium is used, the locking depth is estimated to be deeper. This makes the locked parts of the fault more consistent with the absence of seismicity. Even so, based on geodetic data for the locked segments, the best-fitting locking depths are estimated to be between 5 and 7.5 km. This is substantially lower than the background seismicity estimates of 10 to 15 km. Geometrically complicated segment borders also cause considerable seismicity, making the seismicity patterns more complex. In this regard, the seismicity near the major fault appears to be caused by both interseismic behavior and geometrical complexity.

Furthermore, repeaters documented in various studies (e.g., Schmittbuhl *et al*., 2016a; Uchida *et al*., 2019) are situated inside the zone in which the fault is predicted to be creeping. This is shown in Figure 6.6, which depicts the correlation between the presence of repeaters (Harris, 2017) and interseismic creep. Our findings lead us to the conclusion that the seismicity rate along the MMF and the repeaters in the Marmara Sea are probably related to the interseismic fault behavior.

7.3. Interseismic Behavior and Focal Mechanisms Along the MMF

In Figure 7.1, a comparison is made between the dilatational strain rates, which are the summation of the elements on the diagonal of the horizontal strain rate tensor, at a given locking depth of 10 km throughout the whole MMF, both in a homogeneous (HM_C10) and heterogeneous (3-D) medium (HT_S_C10), as well as the one that was derived employing the interseismic best-fitting locking model in a heterogeneous 3-D elastic medium (HT_S_VB). In this dilatation figure, the red zones with positive values show regimes of extension, while the blue zones with negative values show regimes of compression. Compared to a model with fixed interseismic locking throughout the fault and a homogeneous elastic structure, heterogeneity in velocity structure and fault coupling results in a more complicated strain buildup near the fault.

When the crust is homogeneous and the locking is fixed at a depth of 10 km, the amount of dilatation that occurs is negligible (Figure 7.1a). The incorporation of the 3-D heterogeneity causes an increase in extensional strain rates in the Çınarcık Basin as well as a minor increase in complexity at the Ganos Bend (Figure 7.1b). Analyzing the effect of the heterogeneous fault coupling, the Western Marmara segment's right-lateral movement causes dilatations at the creeping zone's edges (Figure 7.1c).

We analyzed whether the estimated dilatational strains caused by changes in interseismic coupling are compatible with the earthquake focal mechanisms in those zones to find out if they can be trusted. The one-week-long 2019 Silivri earthquake series (Durand *et al*., 2020; Irmak *et al*., 2021; Karabulut *et al*., 2021) north of the MMF, especially, showed that the region's stress regime was more complicated than expected, as illustrated in Figure 2.3. According to most definitions, the Marmara Sea Region is either a

pull-apart system (Armijo *et al*., 2002) or a shear zone with substantial extension (e.g., Rangin *et al*., 2004). In Figure 7.1c, all of the modeled earthquakes that occurred in 2019 in the Silivri region featured considerable thrust components, which demonstrated compression in this zone.

Figures 7.1a and 7.1b show the dilatational strains caused by a complex MMF geometry with a fixed locking, which cannot explain the observed compression in the Silivri region. In Figure 7.1c, we evaluate whether focal mechanism changes in high dilatation zones can be related to interseismic MMF behavior. We collect the 2019 Silivri earthquake focal mechanisms from Karabulut *et al*. (2021), while additional focal mechanisms for the other zones of the Marmara Region come from Pinar *et al*. (2003) and Öztürk *et al*. (2015).

The focal mechanism patterns of the region are rather complicated. As a result, in order to simplify, we compute the best-fitting focal mechanisms representing each zone by adding the moment tensors of all the earthquakes and then obtaining the best-fitting double-couple mechanism, which is shown in Figure 7.1c with the black beach balls. Furthermore, we use an iterative technique developed for stress inversion by Vavryčuk (2014) to derive the orientations of regional stresses (Table 7.1) that result from these focal mechanisms. This approach does this by focusing on the differentiation of the primary and auxiliary fault planes and then solving for the orientations of stresses under the assumption that the stress tensor has a trace of zero.

Table 7.1. Principal stress axes for each Marmara seismotectonic zone obtained by stress inversion of the M > 2.5 earthquake focal mechanisms.

Seismotectonic Zone	N	σ_1		σ_2		σ_3	
		Azimuth	Plunge	Azimuth	Plunge	Azimuth	Plunge
North of Ganos	9	294.4160	79.6616	145.0217	8.9232	54.2063	5.1787
South of Ganos	27	299.3301	12.2092	124.1286	77.7492	29.5452	0.9941
Silivri	12	151.6107	13.6096	248.6879	26.9714	37.5750	59.2727
South of Çınarcık	37	137.2571	88.3640	301.9643	1.5781	31.9762	0.4313

A comparison between the ground surface dilatational strain rates, which were computed using the best-fitting interseismic model, and the earthquake focal mechanisms in the high dilatation rate zones is shown in Figure 7.1c. Additionally, Figure 7.2 displays slices taken from the depths of 5 and 10 km. The zone of compression that is located at the northeast edge of the creeping segment matches the compression seen during the 2019 Silivri earthquakes north of the main fault. We could not find any earthquakes southeast of the creeping segment that we could use to evaluate in relation to the observed dilatations. In contrast to the eastern tip of the creeping segment, the western tip is characterized by extension in the north of the Ganos Bend and compression in the south. While the pattern of earthquakes occurring in the southern portion of the region is complicated, those occurring north of the MMF match the estimated extension of the interseismic creep.

The calculated patterns of strain rate that are caused by the interseismic heterogeneous coupling are completely compatible with the changes in focal mechanisms on each side of the MMF as well as variations in the orientations of stresses. The predicted extension of the Çınarcık Basin, which can be attributed to both asymmetric geometries of fault and basin, is also compatible with the earthquake mechanisms that are present in this region. In addition, the inversions of stresses display changes that are in agreement with the strain rate perturbations that were calculated using the interseismic best-fitting model.

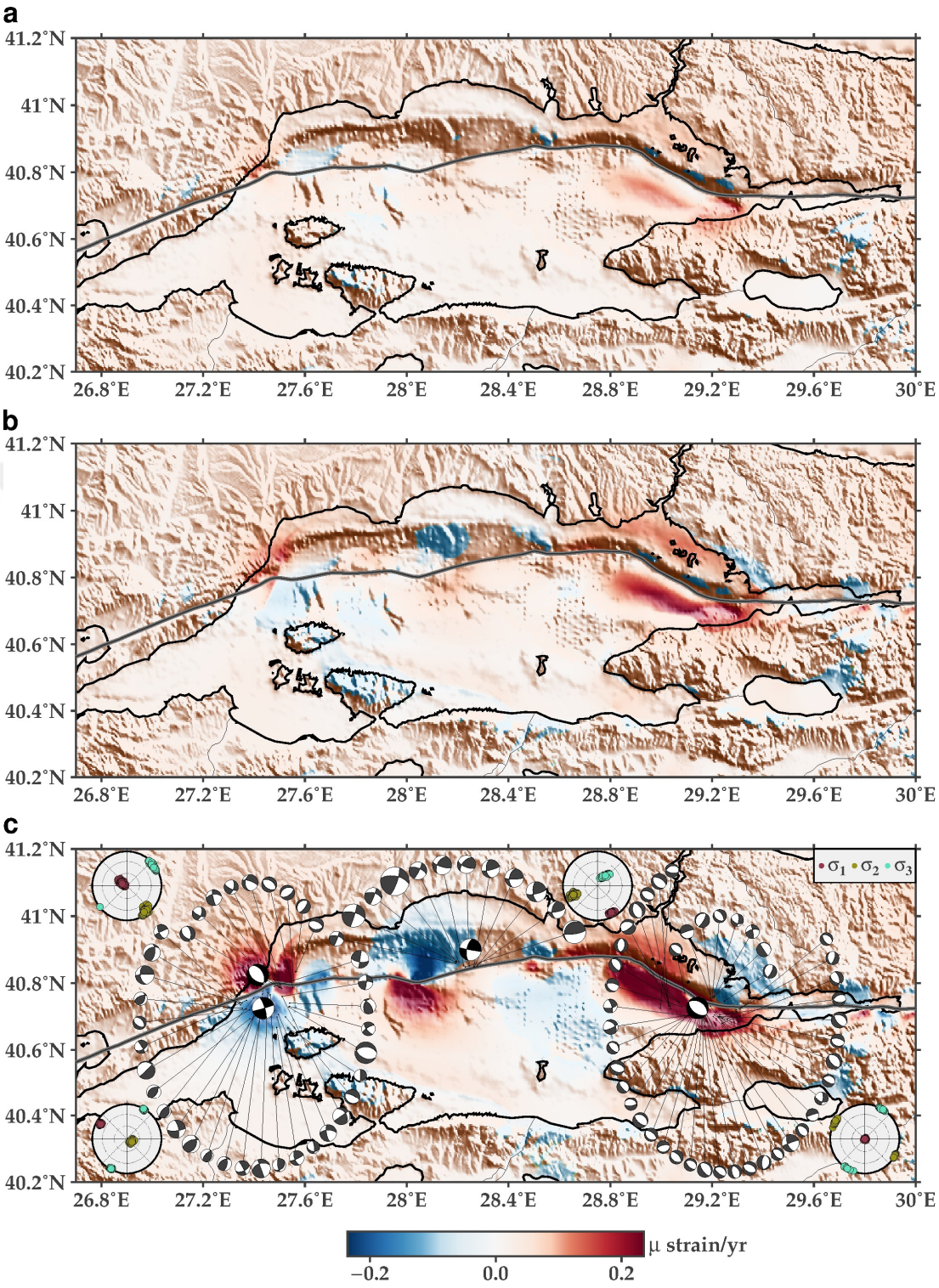

Figure 7.1. Ground surface dilatation rate fields for (a) a homogeneous model with a fixed locking depth of 10 km (HM_C10), (b) a heterogeneous model with a fixed locking depth of 10 km (HT_S_C10), and (c) the heterogeneous best-fitting model (HT_S_VB). Dark gray focal mechanisms indicate off-fault $M_w > 2.5$ earthquakes, whereas black ones suggest double-couple moment tensors that are best fitted for each region. Each zone's principal stress directions are also displayed.

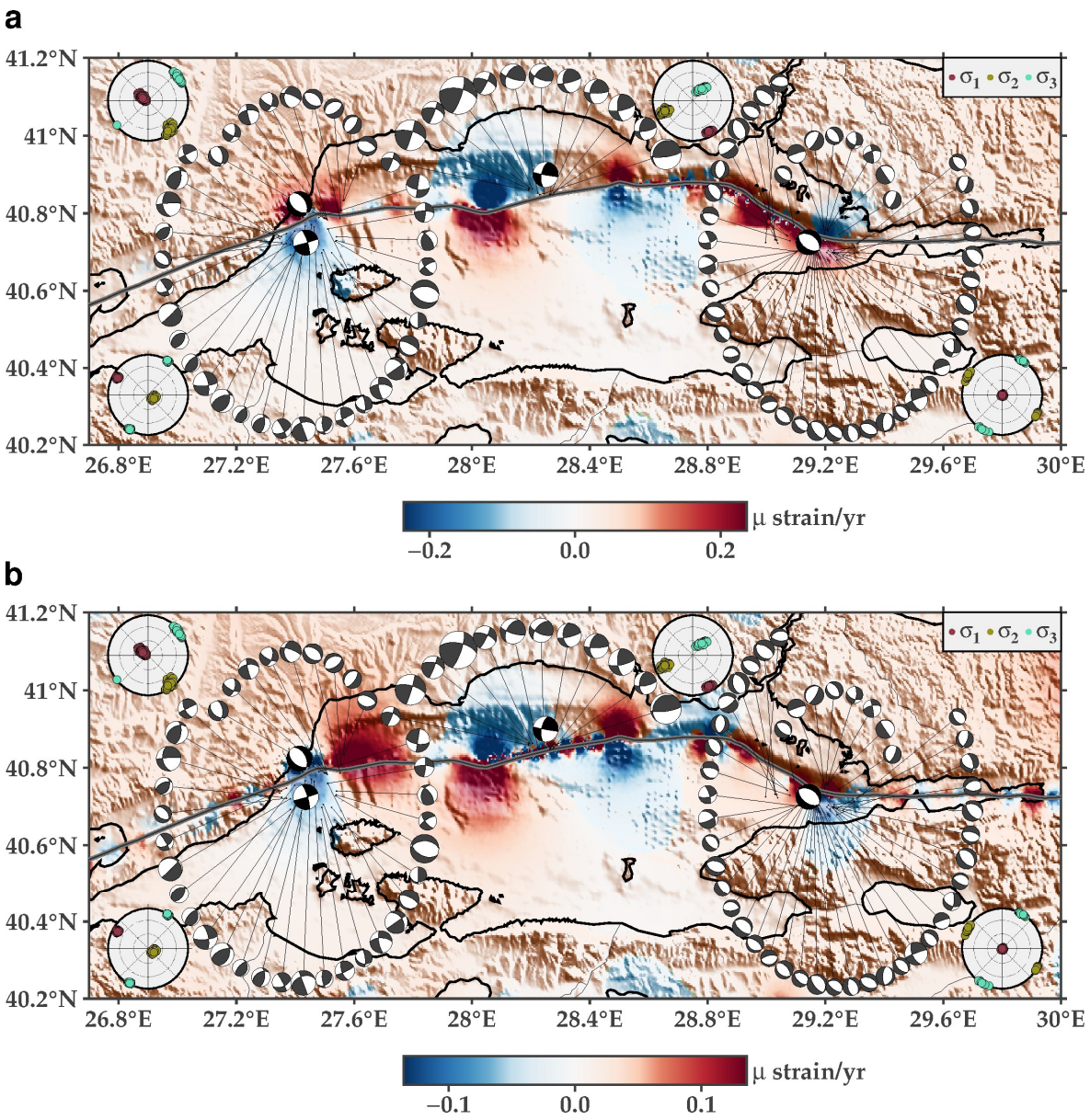

Figure 7.2. Dilatation rate fields for the 3-D heterogeneous best-fitting elastic model (HT_S_VB) at (a) 5 km and (b) 10 km depths.

8. CONCLUSIONS

In the thesis, a realistic FEM model was built to examine the ground deformation and strain buildup caused by the MMF in the Marmara region, as well as to better understand the dominant fault behavior and the lithosphere's rheological characteristics that best explain the deformation. The FEM technique's execution steps, including the preparation stages, are also described, which enables a more detailed analysis of the problem domain by overcoming the inherent limitations of the half-space assumption and allowing the deployment of a 3-D heterogeneous model that takes into account both topography and material heterogeneities. A grid search for fault segment locking depths is performed to extract the distribution of the locking depths beneath the MMF in the Sea of Marmara, which results in a better match for the majority of stations between the observed GNSS measurements and the computed deformation. When compared to the models with a constant fault locking depth, it is concluded that the model with a variable fault locking depth generates a better misfit.

Within the scope of this research, as well as modeling the MMF's interseismic locking, we also focused on the role of basins. We examined to see if the GNSS velocities recorded in the Marmara Sea can be explained by the asymmetric and heterogeneous accumulation of strain as a result of the deep basins. Alternatively, we tested whether employing homogeneous models influences our perceptions of interseismic behavior. Our findings lead us to the conclusion that the presence of these basins has an impact on interseismic strain accumulation. Specifically, we find that employing a heterogeneous structure results in somewhat deeper estimations of locking depths by approximately 2 to 3 km when compared to using a homogeneous structure. On the other hand, the observed GNSS velocity patterns cannot be explained just by the heterogeneous structures alone, but rather interseismic coupling heterogeneities are also needed to explain the observed data, even though the basins have an effect on the pattern of strain accumulation.

In particular, in Eastern Marmara, it is difficult to determine the precise characteristics of the MMF’s locking behavior, as indicated by previous studies (e.g., Klein *et al*., 2017). On the other hand, the present GNSS data imposes some restrictions on the

Western Marmara, which has a fully creeping zone under the Tekirdağ and Central Basins. This eliminates the probability that the two segments are similarly locked. In addition, the transition between this creeping stretch of the fault and the locked section below Ganos is strongly confined and corresponds well with the Ganos Bend, which is a seismic and geometrical complexity along the MMF.

Further, we analyzed to see whether or not the estimated strain rates from interseismic behavior could also be verified by the known earthquake focal mechanisms. Our model is very compatible with the earthquake series that occurred in 2019 in the Silivri region, which demonstrates the presence of considerable compression north of the fault in the Eastern Central Basin. The loading of the fault's creeping segment to the west could provide an explanation for the region's substantial compression. The stress variations around the Ganos Bend to the north and south of the MMF also correspond to variations in interseismic loading caused by the creeping section of the fault.

In agreement with earlier studies of subsurface geodesy, the interseismic coupling pattern identified in this study demonstrates a creep fault behavior under the Western High and a locked fault behavior under the Central High. Furthermore, we hypothesize that the seismic activity along the major faults, especially the pattern of repeating earthquakes, is a reasonable proxy for the creeping segment interseismic behavior, which causes additional background seismicity like the repeaters. Our results show that the differences in seismicity behavior of the individual segments are mostly in line with the interseismic behavior with respect to the locking of the fault.

Our model also shows that the difference between a homogeneously locked versus variable locking model only leads to measurable velocity differences near the Ganos bend. For the other segments, the coast is too far to differentiate between various possibilities. In future research, more focus needs to be given to submarine geodesy and ocean bottom seismometers to better understand the seismic coupling in greater detail. Since available data is frequently sparse and undersampled, a correct interpretation of complex deformation and comprehension of the complex locking depth distribution may be obtained by integrating various data, such as InSAR and land/seafloor geodetic data, to gain sufficient resolution over the entire seismogenic region.

REFERENCES

Aagaard, B. T., M. G. Knepley, and C. A. Williams, 2013, "A domain decomposition approach to implementing fault slip in finite-element models of quasi-static and dynamic crustal deformation", *Journal of Geophysical Research: Solid Earth*, 118(6), pp. 3059–3079, https://doi.org/10.1002/jgrb.50217.

Aagaard, B. T., M. G. Knepley, and C. A. Williams, 2017a, "PyLIth v2.2.1. Computational Infrastructure of Geodynamics".

Aagaard, B. T., M. G. Knepley, and C. A. Williams, 2017b, "PyLith User Manual, Version 2.2.0. Computational Infrastructure for Geodynamics", Retrived from: https://geodynamics.org/cig/software/github/pylith/v2.2.0/pylith-2.2.0_manual.pdf.

Alpar, B. and C. Yaltırak, 2002, "Characteristic features of the North Anatolian Fault in the eastern Marmara region and its tectonic evolution", *Mar. Geol.*, 190, pp. 329–350, PII:S0025-3227(0002)00353-00355.

Ambraseys, N., 2002, "The seismic activity of the Marmara Sea region over the last 2000 years", *Bulletin of the Seismological Society of America*, 92(1), pp. 1–18, https://doi.org/10.1785/0120000843.

Ambraseys, N. N., and J. A. Jackson, 2000, "Seismicity of the Sea of Marmara (Turkey) since 1500", *Geophysical Journal International*, 141(3), pp. F1–F6, https://doi.org/10.1046/j.1365-246X.2000.00137.x.

Armijo, R., B. Meyer, A. Hubert, and A. Barka, 1999, "Westward propagation of the North Anatolian fault into the northern Aegean: timing and kinematics", *Geology*, 27, pp. 267–270.

Armijo, R., B. Meyer, S. Navarro, G. King, and A. Barka, 2002, "Asymmetric slip partitioning in the Sea of Marmara pull-apart: A clue to propagation processes of the north Anatolian Fault?", *Terra Nova*, 14(2), pp. 80–86, hhttps://doi.org/10.1046/j.1365-3121.2002.00397.x.

Armijo, R., N. Pondard, B. Meyer, G. Uçarkuş, B.M.d. Lepinay, J. Malavieille, S.Dominguez, M.-A. Gustcher, S. Schmidt, C. Beck, N. Çagatay, Z. Çakir, C. Imren, K. Eriş, B. Natalin, S. Özalaybey, L. Tolun, I. Lefevre, L. Seeber, L. Gasperini, C. Rangin, O.Emre, and K. Sarikavak, 2005, "Submarine fault scarps in the Sea of Marmara pullapart (North Anatolian Fault): Implications for seismic hazard in Istanbul", *Geochemistry Geophysics Geosystems*, v. 6, p. Q06009, https://doi.org/10.1029/2004GC000896

Barka, A., 1992, "The North Anatolian Fault Zone", *Annales Tectonicae*, Vol. 6, pp. 164-195.

Barka, A., 1996, "Slip distribution along the North Anatolian fault associated with the large earthquakes of the period 1939 to 1967", *Bulletin of the Seismological Society of America*, 86(5), pp. 1238–1254, https://doi.org/10.1785/BSSA0860051238.

Barka, A., H. S. Akyüz, E. Altunel, G. Sunal, Z. Çakir, A. Dikbas, B. Yerli, R. Armijo, B. Meyer, J. B. De Chabalier, T. Rockwell, J. R. Dolan, R. Hartleb, T. Dawson, S. Christofferson, A. Tucker, T. Fumal, R. Langridge, H. Stenner, W. Lettis, J. Bachhuber, and W. Page, 2002, "The Surface Rupture and Slip Distribution of the 17 August 1999 İzmit Earthquake (M 7.4), North Anatolian Fault", *Bulletin of the Seismological Society of America*, 92(1), pp. 43–60, https://doi.org/10.1785/0120000841.

Bassin, C., G. Laske, and G. Masters, 2000, "The current limits of resolution for surface wave tomography in North America", *Eos, Transactions American Geophysical Union*, Vol. 81, p. F897.

Baştürk, N. B., N. M. Özel, Y. Altınok, and T. Y. Duman, 2017, "Türkiye ve yakın çevresi için geliştirilmiş tarihsel dönem (MÖ 2000 - MS 1900-) deprem katalogu", *Türkiye Sismotektonik Haritası Açıklama Kitabı*, Maden Tetkik ve Arama Genel Müdürlüğü, Özel Yayınlar Serisi, Vol. 34, pp. 239.

Bécel, A., M. Laigle, B. de Voogd, A. Hirn, A. Taymaz, A. Galvé, H. Shimamura, Y. Murai, J-C. Lépine, M. Sapin, and S. Özalaybey, 2009, "Moho, crustal architecture and deep deformation under the North Marmara Trough, from the SEISMARMARA Leg 1 offshore–onshore reflection–refraction survey", *Tectonophysics*, 467(1–4), pp. 1–21, https://doi.org/10.1016/j.tecto.2008.10.022.

Bécel, A., M. Laigle, B. de Voogd, A. Hirn, T. Taymaz, S. Yolsal-Cevikbilen, and H. Shimamura, 2010, "North Marmara Trough architecture of basin infill, basement and faults, from PSDM reflection and OBS refraction seismics", *Tectonophysics*, 490(1–2), pp. 1–14, https://doi.org/10.1016/j.tecto.2010.04.004.

Bird, P., 2003, "An updated digital model of plate boundaries", *Geochemistry, Geophysics, Geosystems*, 4(3), https://doi.org/10.1029/2001GC000252.

Bohnhoff, M., F. Bulut, G. Dresen, P. E. Malin, T. Eken, and M. Aktar, 2013, "An earthquake gap south of Istanbul", *Nature Communications*, 4, 1999, https://doi.org/10.1038/ncomms2999.

Bouchon, M., M. P. Bouin, H. Karabulut, M. N. Toksöz, M. Dietrich, and A. J. Rosakis, 2001, "How fast is rupture during an earthquake? New insights from the 1999 Turkey Earthquakes", *Geophysical Research Letters*, 28(14), pp. 2723–2726, https://doi.org/10.1029/2001gl013112.

Bulut, F., B. Aktuğ, C. Yaltırak, A. Doğru, and H. Özener, 2019, "Magnitudes of future large earthquakes near Istanbul quantified from 1500 years of historical earthquakes, present-day microseismicity and GPS slip rates", *Tectonophysics*, 764, pp. 77–87, https://doi.org/10.1016/j.tecto.2019.05.005.

Bürgmann, R., D. Schmidt, R. Nadeau, M. d'Alessio, E. Fielding, D. Manaker, T. McEvilly, and M. Murray, 2000, "Earthquake potential along thenorthern Hayward Fault, California", *Science*, 289(5482), pp. 1178–1182, https://doi.org/10.1126/science.289.5482.1178.

Carton, H., S. C. Singh, A. Hirn, S. Bazin, B. de Voogd, A. Vigner, A. Ricolleau, S. Cetin, N. Ocakoglu, F. Karakoc, and V. Sevilgen, 2007, "Seismic imaging of the three-dimensional architecture of the Çınarcık Basin along the North Anatolian Fault", *Journal of Geophysical Research*, 112(B6), http://doi.org/10.1029/2006jb004548.

Cormier, M.-H, L. Seeber, C. M. G. McHugh, A. Polonia, N. Çagatay, Ö. Emre, L. Gasperini, N. Görür, G. Bortoluzzi, E. Bonatti, W. B. F. Ryan, K. R. Newman, 2006, "North Anatolian Fault in the Gulf of Izmit (Turkey): Rapid vertical motion in response to minor bends of a nonvertical continental transform", *Journal of Geophysical Research: Solid Earth*, 111(B4), https://doi.org/10.1029/2005JB003633.

Delouis, B., D. Giardini, P. Lundgren, and J. Salichon, 2002, "Joint inversion of InSAR, GPS, teleseismic, and strong-motion data for the spatial and temporal distribution of earthquake slip: Application to the 1999 Izmit mainshock", *Bulletin of the Seismological Society of America*, 92(1), pp. 278–299, https://doi.org/10.1785/0120000806.

Dikbaş, A., H. S. Akyüz, M. Meghraoui, M. Ferry, E. Altunel, C. Zabcı, R. Langridge, C. Ç. Yalçıner, 2018, "Paleoseismic history and slip rate along the Sapanca-Akyazı segment of the 1999 İzmit earthquake rupture (Mw = 7.4) of the North Anatolian Fault (Turkey)", *Tectonophysics*, 738–739, pp. 92–111, https://doi.org/10.1016/j.tecto.2018.04.019.

Durand, V., S. Bentz, G. Kwiatek, G. Dresen, C. Wollin, O. Heidbach, P. Martínez-Garzòn, F. Cotton, M. Nurlu, and M. Bohnhoff, 2020, "A Two-Scale Preparation Phase Preceded an Mw 5.8 Earthquake in the Sea of Marmara Offshore Istanbul, Turkey", *Seismological Research Letters*, 91(6), pp. 3139–3147, https://doi.org/10.1785/0220200110.

Emre, Ö., T. Y. Duman, S. Özalp, H. Elmacı, Ş. Olgun, and F. Şaroğlu, 2013, "Active Fault Map of turkey with Explanatory Text", *General Directorate of Mineral Research and Exploration Special Publication Series*, Vol. 30.

Ergintav, S., R. E. Reilinger, R. Çakmak, M. Floyd, Z. Cakir, U. Doğan, R. W. King, S. McClusky, and H. Özener, 2014, "Istanbul's earthquake hot spots: Geodetic constraints on strain accumulation along faults in the Marmara seismic gap", *Geophysical Research Letters*, 41(16), pp. 5783–5788, https://doi.org/10.1002/2014GL060985.

Fialko, Y., 2006, "Interseismic strain accumulation and the earthquake potential on the southern San Andreas fault system", *Nature*, 441, pp. 968–971, https://doi.org/10.1038/nature04797.

Gasperini, L., A. Polonia, G. Bortoluzzi, P. Henry, X. Le Pichon, M. Tryon, N. Çağatay, L. Géli, 2011a, "How far did the surface rupture of the 1999 İzmit earthquake reach in Sea of Marmara?", *Tectonics*, 30(1), https://doi.org/10.1029/2010TC002726.

Gasperini, L., A. Polonia, M. N. Çağatay, G. Bortoluzzi, and V. Ferrante, 2011b, "Geological slip rates along the North Anatolian Fault in the Marmara region", Tectonics, 30, TC6001, doi:10.1029/2011TC002906.

Gasperini, L., M. Stucchi, V. Cedro, M. Meghraoui, G. Ucarkus, and A. Polonia, 2021, "Active fault segments along the north Anatolian Fault system in the Sea of Marmara: Implication for seismic hazard", *Mediterranean Geoscience Reviews*, 3(1), pp. 29–44, https://doi.org/10.1007/s42990-021-00048-7.

Harris, R. A., 2017, "Large earthquakes and creeping faults", *Reviews of Geophysics*, 55(1), pp. 169–198, https://doi.org/10.1002/2016RG000539.

Hergert, T., and O. Heidbach, 2010, "Slip-rate variability and distributed deformation in the Marmara Sea fault system", *Nature Geoscience*, 3(2), pp. 132–135, https://doi.org/10.1038/ngeo739.

Hergert, T., O. Heidbach, A. Bécel, and M. Laigle, 2011, “Geomechanical model of the Marmara Sea region-I. 3-D contemporary kinematics”, *Geophysical Journal International*, 185(3), pp. 1073–1089, https://doi.org/10.1111/j.1365-246X.2011.04991.x.

Hori, T., A. Pinar, O. Necmioglu, M. Hori, and A. Nishizawa, 2017, “Special issue “the next Marmara earthquake: Disaster mitigation, recovery, and early warning” 4. Seismology the next Marmara earthquake: Disaster mitigation, recovery and early warning", *Earth Planets and Space*, 69(1), https://doi.org/10.1186/s40623-017-0648-9.

Irmak, T. S., S. Yolsal-Çevikbilen, T. Eken, B. Doğan, C. Erman, E. Yavuz, H. Alçık, P. Gaebler, A. Pınar, T. Taymaz, 2021, “Source characteristics and seismotectonic implications of the 26 September 2019 Mw 5.7 Silivri high-Kumburgaz basin earthquake and evaluation of its aftershocks at the north Anatolian Fault zone (central Marmara Sea, NW Turkey)”, *Geophysical Journal International*, 227(1), pp. 383–402, https://doi.org/10.1093/gji/ggab233.

Karabulut, H., S. E. Güvercin, F. Eskiköy, A. Ö. Konca, and S. Ergintav, 2021, “The moderate size 2019 September Mw 5.8 Silivri earthquake unveils the complexity of the Main Marmara Fault shear zone”, *Geophysical Journal International*, 224(1), pp. 377–388, https://doi.org/10.1093/gji/ggaa469.

Kende, J., P. Henry, G. Bayrakci, M. S. Özeren, and C. Grall, 2017, “Moho depth and crustal thinning in the Marmara Sea region from gravity data inversion”, *Journal of Geophysical Research: Solid Earth*, 122(2), pp. 1381–1401, https://doi.org/10.1002/2015JB012735.

Klein, E., Z. Duputel, F. Masson, H. Yavasoglu, and P. Agram, 2017, “Aseismic slip and seismogenic coupling in the Marmara Sea: What can we learn from onland geodesy?”, *Geophysical Research Letters*, 44(7), pp. 3100–3108, https://doi.org/10.1002/2017GL072777.

Konca, A. O., S. Cetin, H. Karabulut, R. Reilinger, U. Dogan, S. Ergintav, Z. Cakir, and E. Tari, 2018, "The 2014, MW6.9 North Aegean earthquake: Seismic and geodetic evidence for coseismic slip on persistent asperities", *Geophysical Journal International*, 213(2), pp. 1113–1120, https://doi.org/10.1093/gji/ggy049.

Konca, A. O., S. Leprince, J. P. Avouac, and D. V. Helmberger, 2010, "Rupture process of the 1999 Mw 7.1 duzce earthquake from joint analysis of SPOT, GPS, InSAR, strong-motion, and teleseismic data: A supershear rupture with variable rupture velocity", *Bulletin of the Seismological Society of America*, 100(1), pp. 267–288, https://doi.org/10.1785/0120090072.

Kurtuluş, C., and M.M. Canbay, 2007, "Tracing the middle strand of the North Anatolian Fault Zone through the southern Sea of Marmara based on seismic reflection studies", *Geo-Mar Lett.*, 27, pp. 27–40, doi:10.1007/s00367-006-0050-2.

Laigle, M., A. Becel, B. de Voogd, A. Hirn, T. Taymaz, and S. Ozalaybey, 2008, "A first deep seismic survey in the Sea of Marmara: Deep basins and whole crust architecture and evolution", *Earth and Planetary Science Letters*, 270(3–4), pp. 168–179, https://doi.org/10.1016/j.epsl.2008.02.031.

Lange, D., H. Kopp, J. Y. Royer, P. Henry, Z. Çakir, F. Petersen, P. Sakic, V. Ballu, J. Bialas, M. S. Özeren, S. Ergintav, and L. Géli, 2019, "Interseismic strain build-up on the submarine North Anatolian fault offshore Istanbul", *Nature Communications*, 10(1), 3006, https://doi.org/10.1038/s41467-019-11016-z.

Le Pichon, X., and J. Angelier, 1979, "The hellenic arc and trench system: A key to the neotectonic evolution of the eastern mediterranean area", *Tectonophysics*, 60(1–2), pp. 1–42, https://doi.org/10.1016/0040-1951(79)90131-8.

Le Pichon, X., N. Chamot-Rooke, C. Rangin, and A. M. C. Sengör, 2003, "The North Anatolian Fault in the Sea of Marmara", *Journal of Geophysical Research: Solid Earth*, 108(B4), https://doi.org/10.1029/2002jb001862.

Le Pichon, X., A. M. C. Şengör, E. Demirbağ, C. Rangin, C. İmren, R. Armijo, N. Görür, N. Çağatay, B. Mercier De Lepinay, B. Meyer, R. Saatçiler, and B. Tok, 2001, "The active main Marmara Fault", *Earth and Planetary Science Letters*, 192(4), pp. 595–616, https://doi.org/10.1016/S0012-821X(01)00449-6.

Le Pichon, X., C. Kreemer, and N. Chamot-Rooke, 2005, "Asymmetry in elastic properties and the evolution of large continental strike-slip faults", *Journal of Geophysical Research: Solid Earth*, 110(B3), https://doi.org/10.1029/2004JB003343.

Liu, Y-K., Z. E. Ross, E. S. Cochran, and N. Lapusta, 2022, "A unified perspective of seismicity and fault coupling along the San Andreas Fault", *Science advances*, Vol. 8, https://doi.org/10.1126/sciadv.abk1167.

McClusky, S., S. Balassanian, A. Barka, C. Demir, S. Ergintav, I. Georgiev, O. Gurkan, M. Hamburger, K. Hurst, H.-G. Kahle, K. Kastens, G. Kekelidze, R. W. King, V. Kotzev, O. Lenk, S. Mahmoud, A. Mishin, M. Nadariya, A. Ouzounis, D. Paradissis, Y. Peter, M. Prilepin, R. E. Reilinger, I. Sanli, H. Seeger, A. Tealeb, M. N. Toksöz, and G. Veis 2000, "Global Positioning System constraints on plate kinematics and dynamics in the eastern Mediterranean and Caucasus", *Journal of Geophysical Research: Solid Earth*, 105(B3), pp. 5695–5719, https://doi.org/10.1029/1999jb900351.

McHugh, C. M. G., L. Seeber, M-H. Cormier, J. Dutton, N. Çağatay, A. Polonia, W. B. F. Ryan, and N. Gorur, 2006, "Submarine earthquake geology along the North Anatolia Fault in the Marmara Sea, Turkey: a model for transform basin sedimentation", *Earth Planet Sci Lett.*, Vol. 248, pp. 661–684, https://doi.org/10.1016/j.epsl.2006.05.038.

McKenzie, D., 1972, "Active tectonics of the Mediterranean region", *Geophysical Journal of the Royal Astronomical Society*, 30(2), pp. 109–185, https://doi.org/10.1111/j.1365-246X.1972.tb02351.x.

Meade, B. J., B. H. Hager, S. C. McClusky, R. E. Reilinger, S. Ergintav, O. Lenk, A. Barka, and H. Özener, 2002, "Estimates of seismic potential in the Marmara Sea

region from block models of secular deformation constrained by Global Positioning System measurements", *Bulletin of the Seismological Society of America*, 92(1), pp. 208–215, https://doi.org/10.1785/0120000837.

Meghraoui, M., M. E. Aksoy, H. S. Akyüz, M. Ferry, A. Dikbaş, and E. Altunel, 2012, "Paleoseismology of the north Anatolian Fault at güzelköy (Ganos segment, Turkey): Size and recurrence time of earthquake ruptures west of the Sea of Marmara", *Geochemistry, Geophysics, Geosystems*, 13(4), https://doi.org/10.1029/2011GC003960.

Nadeau, R., W. Foxall, and T. McEvilly, 1995, "Clustering and periodic recurrence of microearthquakes on the San Andreas Fault at Parkfield, California", *Science*, Vol. 267(5197), pp. 503–507, https://doi.org/10.1126/science.267.5197.503.

Olson, C. J., J. J. Becker, and D. T. Sandwell, 2014, "A new global bathymetry map at 15 arcsecond resolution for resolving seafloor fabric: SRTM15_PLUS", *AGU Fall Meeting Abstracts*, Vol. 1, pp. OS34A–03.

Özbey, V., M. S. Özeren, P. Henry, E. Klein, G. Galgana, H. Karabulut, D. Lange, and R. McCaffrey, 2021, "Kinematics of the Marmara region: A fusion of continuum and block models", *Mediterranean Geoscience Reviews*, 3(1), https://doi.org/10.1007/s42990-021-00051-y.

Öztürk, Y. K., N. M. Özel, and A. D. Özbakir, 2015, "States of local stresses in the Sea of Marmara through the analysis of large numbers of small earthquakes", *Tectonophysics*, 665, pp. 37–57, https://doi.org/10.1016/j.tecto.2015.09.027.

Parke, J. R., R. S. White, D. McKenzie, T. A. Minshull, J. M. Bull, I. Kuşçu, J. M. Bull, N. Görür, and C. Şengör, 2002, "Interaction between faulting and sedimentation in the Sea of Marmara, western Turkey", *Journal of Geophysical Research: Solid Earth*, 107(B11), https://doi.org/10.1029/2001jb000450.

Parsons, T., 2004, "Recalculated probability of M ≥ 7 earthquakes beneath the Sea of Marmara, Turkey", *Journal of Geophysical Research: Solid Earth*, 109(B5), https://doi.org/10.1029/2003JB002667.

Pinar, A., K. Kuge, and Y. Honkura, 2003, "Moment tensor inversion of recent small to moderate sized earthquakes: Implications for seismic hazard and active tectonics beneath the Sea of Marmara", *Geophysical Journal International*, 153(1), pp. 133–145, https://doi.org/10.1046/j.1365-246X.2003.01897.x.

Pondard, N., R. Armijo, G. C. P. King, B. Meyer, and F. Flerit, 2007, "Fault interactions in the Sea of Marmara pull-apart (north Anatolian Fault): Earthquake clustering and propagating earthquake sequences", *Geophysical Journal International*, 171(3), pp. 1185–1197, https://doi.org/10.1111/j.1365-246X.2007.03580.x.

Rangin, C., X. Le Pichon, E. Demirbag, and C. Imren, 2004, "Strain localization in the Sea of Marmara: Propagation of the north Anatolian Fault in a now inactive pull-apart", *Tectonics*, 23(2), https://doi.org/10.1029/2002TC001437.

Reilinger, R., S. McClusky, P. Vernant, S. Lawrence, S. Ergintav, R. Cakmak, H. Ozener, F. Kadirov, I. Guliev, R. Stepanyan, M. Nadariya, G. Hahubia, S. Mahmoud, K. Sakr, A. ArRajehi, D. Paradissis, A. Al-Aydrus, M. Prilepin, T. Guseva, E. Evren, A. Dmitrotsa, S. V. Filikov, F. Gomez, R. Al-Ghazzi, and G. Karam, 2006, "GPS constraints on continental deformation in the Africa-Arabia-Eurasia continental collision zone and implications for the dynamics of plate interactions", *Journal of Geophysical Research: Solid Earth*, 111(B5), https://doi.org/10.1029/2005JB004051.

Reilinger, R. E., S. Ergintav, R. Burgmann, S. McClusky, O. Lenk, A. Barka, O. Gurkan, L. Hearn, K. L. Feigl, R. Cakmak, B. Aktug, H. Ozener, and M. N. Toksöz, 2000, "Coseismic and postseismic fault slip for the 17 august 1999, M = 7.5, Izmit, Turkey earthquake", *Science*, 289, pp. 1519–1524, https://doi.org/10.1126/science.289.5484.1519.

Rodriguez-Suarez, C., 2005, “Sea-bottom shear-wave velocities and mode conversions”, *Revista Brasileira de Geofísica*, 23(1), https://doi.org/10.1590/S0102-261X2005000100007.

Sakic, P., H. Piété, V. Ballu, J. Y. Royer, H. Kopp, D. Lange, F. Petersen, M. S. Özeren, S. Ergintav, L. Geli, P. Henry, and A. Deschamps, 2016, “No significant steady state surface creep along the North Anatolian Fault offshore Istanbul: Results of 6 months of seafloor acoustic ranging”, *Geophysical Research Letters*, 43(13), pp. 6817–6825, https://doi.org/10.1002/2016GL069600.

Savage, J. C., and R. O. Burford, 1973, “Geodetic determination of relative plate motion in central California”, *Journal of Geophysical Research*, 78(5), pp. 832–845, https://doi.org/10.1029/jb078i005p00832.

Schmittbuhl, J., H. Karabulut, O. Lengliné, and M. Bouchon, 2016a, “Long-lasting seismic repeaters in the Central Basin of the main Marmara Fault”, *Geophysical Research Letters*, 43(18), pp. 9527–9534, https://doi.org/10.1002/2016GL070505.

Schmittbuhl, J., H. Karabulut, O. Lengliné, and M. Bouchon, 2016b, “Seismicity distribution and locking depth along the Main Marmara Fault, Turkey”, *Geochemistry, Geophysics, Geosystems*, 17(3), pp. 954–965, https://doi.org/10.1002/2015GC006120.

Seeber, L., O. Emre, M. H. Cormier, C. C. Sorlien, C. M. G. McHugh, A. Polonia, N. Ozer, and N. Cagatay, 2004, “Uplift and subsidence from oblique slip: The Ganos–Marmara bend of the North Anatolian Transform, western Turkey”, *Tectonophysics*, 391(1–4), pp. 239–258, https://doi.org/10.1016/j.tecto.2004.07.015.

Stein, R. S., A. A. Barka, and J. H. Dieterich, 1997, “Progressive failure on the North Anatolian fault since 1939 by earthquake stress triggering”, *Geophysical Journal International*, 128(3), pp. 594–604, https://doi.org/10.1111/j.1365-246X.1997.tb05321.x.

Şengör, A. M. C., C. Grall, C. İmren, X. Le Pichon, N. Görür, P. Henry, H. Karabulut, and M. Siyako, 2014, "The geometry of the North Anatolian transform fault in the Sea of Marmara and its temporal evolution: Implications for the development of intracontinental transform faults", *Canadian Journal of Earth Sciences*, 51(3), pp. 222–242, https://doi.org/10.1139/cjes-2013-0160.

Şengör, A. M. C., O. Tüysüz, C. İmren, M. Sakınç, H. Eyidoğan, N. Görür, X. Le Pichon, and C. Rangin, 2005, "The North Anatolian fault: A new look", *Annual Review of Earth and Planetary Sciences*, 33(1), pp. 37–112, https://doi.org/10.1146/annurev.earth.32.101802.120415.

Uchida, N., D. Kalafat, A. Pinar, and Y. Yamamoto, 2019, "Repeating earthquakes and interplate coupling along the western part of the North Anatolian Fault", *Tectonophysics*, 769, 228185, https://doi.org/10.1016/j.tecto.2019.228185.

Uçarkuş, G., Z. Çakır, and R. Armijo, 2011, "Western Termination of the Mw 7.4, 1999 İzmit Earthquake Rupture: Implications for the Expected Large Earthquake in the Seaof Marmara", *Turkish Journal of Earth Sciences,* Vol. 20, pp. 379–394, doi:10.3906/yer-0911-72.

Vavryčuk, V., 2014, "Iterative joint inversion for stress and fault orientations from focal mechanisms", *Geophysical Journal International*, 199(1), pp. 69–77, https://doi.org/10.1093/gji/ggu224.

Wesnousky, S.G., 2006, "Predicting the endpoints of earthquake ruptures", *Nature*, Vol. 444(7117), pp. 358–360.

Yaltırak, C., and B. Alpar, 2002a, "Kinematics and evolution of the northern branch of the North Anatolian Fault (Ganos Fault) between the Sea of Marmara and the Gulf of Saros", *Mar. Geol.*, 190, pp. 351–366.

Yaltırak, C., and B. Alpar, 2002b, “Evolution of the middle strand of the North Anatolian Fault and shallow seismic investigation of the southeastern Marmara Sea (Gemlik Bay)”, *Mar. Geol.*, 190, pp. 307–327.

Yamamoto, R., M. Kido, Y. Ohta, N. Takahashi, Y. Yamamoto, A. Pinar, D. Kalafat, H. Özener, and Y. Kaneda, 2019, “Seafloor geodesy revealed partial creep of the north Anatolian Fault submerged in the Sea of Marmara”, *Geophysical Research Letters*, 46(3), pp. 1268–1275, https://doi.org/10.1029/2018GL080984.

Yılmaz, Z., A. Ö. Konca, and S. Ergintav, 2022, “The Effect of the 3-D Structure on Strain Accumulation and the Interseismic Behavior Along the North Anatolian Fault in the Sea of Marmara”, *Journal of Geophysical Research: Solid Earth*, 127(3), e2021JB022838, https://doi.org/https://doi.org/10.1029/2021JB022838.

APPENDIX A: LIST OF GNSS STATIONS

Table A.1. Initial dataset of GNSS stations within the study area (Ergintav *et al*., 2014), where t_1 and t_2 denote the first and end data usage periods, F denotes the survey or continuous site with horizontal velocities, 1−σ uncertainties, and correlation coefficients.

No	Site	F	Longitude (°E)	Latitude (°N)	V_E	V_N	σ_E	σ_N	ρ_{EN}	t_1	t_2
					(mm/yr)						
1	AKCO	s	29.97311	41.03354	2.40	1.36	0.36	0.38	-0.039	1999.674	2011.377
2	AVCI	s	28.72735	40.98681	0.95	0.04	1.21	1.29	-0.054	1998.768	2003.375
3	BGNT	s	26.57014	40.93244	2.11	-2.28	0.34	0.36	-0.037	2002.934	2011.377
4	BKCT	s	27.09140	40.20343	-17.04	-6.81	0.39	0.42	-0.076	2002.934	2011.377
5	CINA	s	29.14313	40.63947	-14.23	3.33	0.75	0.86	-0.062	1994.736	2011.377
6	CLTK	s	30.40452	40.88001	2.03	2.40	0.37	0.41	-0.038	2003.755	2011.377
7	DERN	s	29.68138	40.36165	-21.55	-1.17	0.91	0.99	-0.008	1994.736	2011.377
8	DGCT	s	30.46175	40.47786	-22.79	-0.35	0.39	0.42	-0.044	2003.755	2011.377
9	DOKU	s	26.70645	40.73927	-2.73	-0.96	0.33	0.35	-0.051	1994.736	2011.37
10	ERCT	s	29.24320	40.31874	-20.95	-0.16	0.37	0.41	-0.076	2002.934	2011.377
11	FIST	s	28.88184	40.48057	-18.80	-0.98	0.29	0.56	-0.014	1997.734	2011.377
12	FLRT	s	28.77894	40.97483	-1.39	1.24	0.92	1.05	-0.037	2009.4	2013.466
13	GVNT	s	27.47555	40.26550	-18.42	-5.06	1.17	1.24	-0.085	2008.377	2011.377
14	H009	s	28.53580	41.06188	1.19	-0.26	1.30	0.99	-0.039	2009.4	2013.466
15	HARM	s	29.31022	40.92680	0.80	0.68	0.44	0.48	-0.056	2003.853	2010.395
16	IBBT	s	29.32082	40.86602	-0.44	0.35	0.34	0.36	-0.024	2003.853	2011.377
17	IGAZ	s	29.90800	40.43800	-17.13	0.58	0.82	0.90	0.006	1994.736	2011.377
18	IKAN	s	29.06362	41.06359	-1.81	3.50	0.50	0.51	-0.007	1994.736	1999.674
19	IUCK	s	29.92894	40.42473	-17.70	-0.05	1.81	1.83	-0.005	1994.736	2004.421
20	KABI	s	27.30124	40.38099	-16.43	-5.35	0.38	0.41	-0.046	1994.736	2011.377
21	KAMT	s	29.27328	40.83435	-1.18	1.21	0.41	0.44	-0.036	2003.853	2011.377
22	KANR	s	30.29356	41.04825	2.60	1.89	0.57	0.61	-0.048	1997.734	2011.377
23	KAZI	s	30.30341	40.78522	-3.90	3.20	0.74	0.84	-0.085	1999.674	2011.377
24	KFKT	s	30.22937	41.18680	2.51	2.97	0.37	0.40	-0.042	2003.755	2011.377

Table A.1. Initial dataset of GNSS stations within the study area (Ergintav *et al*., 2014), where t_1 and t_2 denote the first and end data usage periods, F denotes the survey or continuous site with horizontal velocities, 1−σ uncertainties, and correlation coefficients. (cont.)

No	Site	F	Longitude (°E)	Latitude (°N)	V_E	V_N	σ_E	σ_N	ρ_{EN}	t_1	t_2
					(mm/yr)						
25	KMBT	s	28.47585	41.04091	-0.84	1.27	1.04	1.16	-0.042	2009.4	2013.466
26	KRDM	s	29.36247	41.01709	1.65	-0.08	0.31	0.34	-0.046	1997.734	2011.377
27	KUTE	s	29.28794	40.48473	-19.84	-0.46	0.37	0.40	-0.069	1997.734	2011.377
28	KVAM	s	26.87128	40.60081	-9.05	-3.26	0.67	0.73	-0.062	2002.934	2007.381
29	KVM2	s	26.87139	40.60069	-10.33	-4.00	1.04	1.12	-0.095	1994.736	2011.377
30	MAER	s	27.96001	40.97062	4.15	2.47	1.31	1.34	-0.027	1994.736	1999.411
31	MISL	s	27.58554	40.58778	-15.31	-4.11	1.05	1.09	0.003	1996.682	1999.411
32	N101	s	28.61529	40.99573	1.00	-1.18	1.20	1.31	0.100	2007.658	2011.377
33	N102	s	28.61627	41.02578	1.77	2.05	0.61	0.66	0.024	2007.658	2013.466
34	N103	s	28.68389	41.03013	-2.10	3.55	0.49	1.33	-0.008	2007.658	2013.466
35	N104	s	28.65969	40.98540	0.58	0.42	0.51	0.56	-0.062	2007.658	2013.466
36	N107	s	28.67185	41.05651	-3.92	1.13	1.07	1.28	-0.007	2007.658	2011.377
37	N108	s	28.65249	41.02162	2.41	4.43	1.09	1.26	-0.017	2007.658	2010.395
38	N110	s	28.63109	41.04334	2.69	0.77	0.51	0.67	-0.009	2007.658	2013.466
39	OLU1	s	29.58524	40.66713	-14.79	-0.08	0.45	0.48	-0.045	1997.734	2011.377
40	OLU2	s	29.58529	40.66713	-14.79	-0.08	0.45	0.48	-0.045	1998.768	2003.375
41	OVCT	s	29.53923	40.97974	1.17	0.46	0.35	0.38	-0.048	2002.934	2011.377
42	SEFI	s	30.32520	40.61164	-20.26	0.23	0.44	0.47	-0.089	1998.768	2011.377
43	SELP	s	28.36533	41.05183	0.38	1.06	0.28	0.29	-0.036	1996.724	2011.377
44	SEV2	s	26.87973	40.39581	-15.39	-6.01	0.35	0.37	-0.050	1999.411	2011.377
45	SEYH	s	30.45336	40.35061	-23.62	-0.01	0.38	0.41	-0.038	1997.734	2011.377
46	SILE	s	29.62324	41.17945	1.78	0.56	0.36	0.41	-0.040	1996.724	2011.377
47	SISL	s	30.13025	40.74533	-7.82	1.52	0.85	0.93	0.003	1994.736	2003.375
48	SMAS	s	30.13404	40.68972	-14.57	1.17	0.78	0.84	-0.017	1994.736	2011.377
49	YACT	s	29.23786	40.91671	0.79	-0.21	0.74	0.80	-0.089	2003.853	2008.377
50	YENB	s	27.39281	40.81074	-2.44	-2.56	0.83	0.91	-0.092	1994.736	1999.411

Table A.1. Initial dataset of GNSS stations within the study area (Ergintav *et al*., 2014), where t_1 and t_2 denote the first and end data usage periods, F denotes the survey or continuous site with horizontal velocities, 1−σ uncertainties, and correlation coefficients. (cont.)

No	Site	F	Longitude (°E)	Latitude (°N)	V_E	V_N	σ_E	σ_N	ρ_{EN}	t_1	t_2
					(mm/yr)						
51	YENI	s	28.37327	40.39790	-18.68	-1.53	0.29	0.32	-0.034	1996.724	2011.377
52	AVCT	c	28.72386	40.98867	-4.68	2.59	0.51	0.27	-0.002	2002.174	2013.451
53	BAD1	c	29.11790	40.85212	-0.83	1.94	0.17	0.14	-0.002	2002.316	2013.489
54	BADT	c	29.11792	40.85214	-0.83	1.94	0.17	0.14	-0.002	2001.147	2002.316
55	BAND	c	27.99671	40.33123	-17.95	-4.19	0.24	0.39	-0.003	2008.739	2011.281
56	BEYK	c	29.09352	41.17672	1.03	0.75	0.29	0.30	0.001	2008.974	2013.401
57	BOZT	c	28.78204	40.53439	-16.73	-1.62	0.13	0.23	-0.001	2000.772	2013.489
58	BURS	c	29.01523	40.21425	-22.09	-2.00	0.22	0.28	-0.005	2008.739	2011.281
59	DRGT	c	29.14526	40.90880	-1.03	0.59	0.20	0.66	-0.019	2004.327	2011.04
60	DUMT	c	29.37190	40.56553	-18.57	0.44	0.18	0.12	-0.002	1999.585	2013.489
61	ERDT	c	27.80795	40.39322	-17.31	-2.90	0.19	0.10	-0.001	2002.508	2013.47
62	IPSA	c	26.37978	40.91753	-0.10	0.89	0.26	0.29	-0.003	2008.854	2011.281
63	ISTA	c	29.01934	41.10445	1.64	-0.09	0.21	0.12	-0.001	1999.944	2013.999
64	ISTN	c	28.83164	40.99096	0.69	2.35	0.23	0.32	-0.004	2008.739	2011.281
65	IZMC	c	29.95094	40.80198	-3.29	0.55	0.29	0.30	-0.003	2008.739	2011.281
66	KAGI	c	28.96320	41.08632	-0.27	1.72	0.21	0.24	-0.004	2008.917	2013.311
67	KART	c	28.33257	40.26526	-19.61	-2.03	0.09	0.11	-0.001	2000.898	2013.489
68	KCEK	c	28.77975	41.00275	-0.81	1.28	0.28	0.17	-0.002	2008.917	2013.311
69	KRDT	c	26.99851	40.95073	-1.17	-0.58	0.12	0.17	-0.003	2004.299	2013.475
70	MADT	c	27.58694	40.61135	-16.39	-3.82	0.10	0.10	-0.001	1999.5	2013.489
71	MER1	c	27.96175	40.96693	0.83	2.30	0.14	0.19	-0.003	2000.955	2013.489
72	MERT	c	27.96171	40.96690	0.83	2.30	0.14	0.19	-0.003	1999.538	2000.952
73	SILC	c	29.61332	41.17900	1.07	1.02	0.21	0.19	-0.003	2008.919	2013.311
74	SLEE	c	29.60068	41.16873	1.50	5.17	0.22	1.01	-0.001	2008.766	2011.281
75	SVRI	c	28.08340	41.08022	0.32	1.55	0.42	0.18	-0.003	2008.917	2013.311
76	SVRT	c	28.97351	40.87471	-5.05	-0.90	0.54	1.00	-0.003	2011.834	2013.489

Table A.1. Initial dataset of GNSS stations within the study area (Ergintav *et al*., 2014), where t_1 and t_2 denote the first and end data usage periods, F denotes the survey or continuous site with horizontal velocities, 1−σ uncertainties, and correlation coefficients. (cont.)

No	Site	F	Longitude (°E)	Latitude (°N)	V_E	V_N	σ_E	σ_N	ρ_{EN}	t_1	t_2
					(mm/yr)						
77	TEKR	c	27.49650	40.95834	0.06	-0.82	0.39	0.29	-0.004	2008.739	2011.281
78	TUBI	c	29.45069	40.78672	-2.03	-0.30	0.12	0.13	-0.000	1998.347	2013.993
79	TUZL	c	29.29245	40.82650	-2.54	1.73	0.23	0.19	-0.004	2008.917	2013.311
80	TYF1	c	26.48568	40.38407	-13.43	-5.54	0.47	0.17	-0.005	2005.626	2013.489
81	TYFT	c	26.48698	40.38310	-13.43	-5.54	0.47	0.17	-0.005	2004.31	2005.681
82	UCG2	c	29.96240	40.84552	2.28	2.70	0.14	0.28	-0.002	2000.764	2013.489
83	UCGT	c	29.96229	40.84566	2.28	2.70	0.14	0.28	-0.002	1999.626	2000.428
84	YANT	c	29.11272	40.81972	-1.05	2.35	0.16	0.29	-0.003	2004.387	2013.489
85	YENT	c	26.58727	40.46833	-11.92	-5.69	0.26	0.41	0.000	2005.626	2013.489
86	YSST	c	28.99087	40.86578	-2.73	2.14	0.66	0.39	-0.001	2011.834	2013.489

APPENDIX B: LIST OF GNSS STATIONS USED IN PROFILES

Table B.1. GNSS stations used in the profiles of the 6 MMF segments.

Profile	Stations
A-a	YACT, ERCT, KAMT, KUTE, TUZL, HARM, IBBT, KRDM, DUMT, TUBI, OVCT, OLU1,SLEE, SILC, SILE, DERN, IGAZ, IUCK, IZMC, UCG2, AKCO, SISL, SMAS, KFKT, KANR, KAZI, SEFI, CLTK, SEYH, DGCT
B-b	KAGI, SVRT, YSST, ISTA, IKAN, BEYK, YANT, BADT, CINA, DRGT, YACT, KAMT, TUZL, HARM, IBBT, KRDM
C-c	KMBT, H009, N102, N110, FLRT, KCEK, ISTN
D-d	SVRI, SELP, KMBT
E-e	YENB, TEKR, MISL, MADT, MERT
F-f	IPSA, TYFT, YENT, DOKU, KVAM, KVM2, SEV2, KRDT, BKCT, KABI, GVNT

APPENDIX C: A COMPARISON OF χ_r^2 MISFITS

Table C.1. The comparison of χ_r^2 misfits from the 0, 5 and 10 km locking depth grid search for the Marmara Sea segments B to E in Figure 5.3c using all available 76 GNSS sites with the modified covariance matrices ($\chi_r^2{}_1$), originally reported covariance matrices ($\chi_r^2{}_2$) and using 21 GNSS close to the MMF with the modified covariance matrices ($\chi_r^2{}_3$).

No	E	D	C	B	$\chi_r^2{}_1$	$\chi_r^2{}_2$	$\chi_r^2{}_3$
1	0	10	0	5	5.27	18.9	4.41
2	0	10	5	5	5.28	18.9	4.42
3	5	10	0	5	5.32	19.5	4.6
4	5	10	5	5	5.33	19.5	4.61
5	0	5	5	5	5.34	19.2	4.7
6	0	5	0	5	5.34	19.2	4.75
7	0	10	0	0	5.38	19.3	4.64
8	5	5	5	5	5.38	19.7	4.84
9	0	10	5	0	5.38	19.3	4.63
10	5	5	0	5	5.38	19.7	4.89
11	0	0	5	5	5.39	19.3	4.88
12	0	0	0	5	5.4	19.4	4.95
13	0	10	10	5	5.4	19.3	4.76
14	5	0	5	5	5.42	19.8	5.01
15	5	10	0	0	5.43	19.9	4.82
16	5	0	0	5	5.43	19.9	5.07
17	0	5	10	5	5.44	19.4	4.96
18	5	10	5	0	5.44	19.9	4.83
19	0	5	5	0	5.44	19.6	4.91
20	0	5	0	0	5.45	19.6	4.96
21	5	10	10	5	5.46	19.9	4.96
22	0	0	10	5	5.47	19.6	5.1
23	5	5	10	5	5.48	20	5.11
24	5	5	5	0	5.48	20.1	5.05

Table C.1. The comparison of χ_r^2 misfits from the 0, 5 and 10 km locking depth grid search for the Marmara Sea segments B to E in Figure 5.3c using all available 76 GNSS sites with the modified covariance matrices ($\chi_r^2{}_1$), originally reported covariance matrices ($\chi_r^2{}_2$) and using 21 GNSS close to the MMF with the modified covariance matrices ($\chi_r^2{}_3$). (cont.)

No	E	D	C	B	$\chi_r^2{}_1$	$\chi_r^2{}_2$	$\chi_r^2{}_3$
25	0	0	5	0	5.48	19.7	5.08
26	5	5	0	0	5.49	20.1	5.1
27	0	0	0	0	5.5	19.8	5.15
28	0	10	10	0	5.51	19.7	4.99
29	5	0	10	5	5.51	20.1	5.24
30	5	0	5	0	5.52	20.2	5.21
31	0	5	10	0	5.53	19.8	5.16
32	5	0	0	0	5.53	20.3	5.27
33	5	10	10	0	5.56	20.3	5.19
34	0	0	10	0	5.57	20	5.3
35	5	5	10	0	5.58	20.4	5.31
36	5	0	10	0	5.61	20.5	5.44
37	10	5	0	5	5.67	22.7	5.83
38	10	5	5	5	5.67	22.7	5.81
39	10	0	5	5	5.68	22.7	5.89
40	10	0	0	5	5.69	22.7	5.93
41	10	10	0	5	5.7	23	5.87
42	10	10	5	5	5.71	23	5.9
43	10	5	5	0	5.77	23.1	6.01
44	10	5	0	0	5.77	23.1	6.04
45	10	5	10	5	5.78	23	6.12
46	10	0	5	0	5.78	23.1	6.08
47	10	0	10	5	5.79	23	6.16
48	10	0	0	0	5.79	23.1	6.13
49	10	10	0	0	5.8	23.4	6.1
50	10	10	5	0	5.82	23.4	6.12
51	10	10	10	5	5.85	23.5	6.31

Table C.1. The comparison of χ_r^2 misfits from the 0, 5 and 10 km locking depth grid search for the Marmara Sea segments B to E in Figure 5.3c using all available 76 GNSS sites with the modified covariance matrices ($\chi_r^2{}_1$), originally reported covariance matrices ($\chi_r^2{}_2$) and using 21 GNSS close to the MMF with the modified covariance matrices ($\chi_r^2{}_3$). (cont.)

No	E	D	C	B	$\chi_r^2{}_1$	$\chi_r^2{}_2$	$\chi_r^2{}_3$
52	10	5	10	0	5.88	23.4	6.33
53	10	0	10	0	5.88	23.4	6.36
54	0	10	0	10	5.89	22.4	6.23
55	0	10	5	10	5.91	22.4	6.23
56	5	10	0	10	5.95	23	6.42
57	10	10	10	0	5.96	23.9	6.53
58	5	10	5	10	5.96	23	6.43
59	0	5	0	10	5.97	22.8	6.59
60	0	5	5	10	5.97	22.7	6.55
61	5	5	0	10	6.01	23.3	6.73
62	5	5	5	10	6.01	23.3	6.69
63	0	0	5	10	6.02	22.9	6.74
64	0	0	0	10	6.03	23	6.8
65	0	10	10	10	6.04	22.7	6.55
66	5	0	5	10	6.06	23.4	6.87
67	5	0	0	10	6.06	23.5	6.93
68	0	5	10	10	6.07	23	6.78
69	5	10	10	10	6.09	23.4	6.75
70	0	0	10	10	6.11	23.1	6.93
71	5	5	10	10	6.12	23.5	6.92
72	5	0	10	10	6.15	23.6	7.07
73	10	5	0	10	6.3	26.3	7.68
74	10	5	5	10	6.3	26.3	7.66
75	10	10	0	10	6.32	26.5	7.69
76	10	0	0	10	6.32	26.3	7.78
77	10	0	5	10	6.32	26.3	7.74
78	10	10	5	10	6.34	26.5	7.72

Table C.1. The comparison of χ_r^2 misfits from the 0, 5 and 10 km locking depth grid search for the Marmara Sea segments B to E in Figure 5.3c using all available 76 GNSS sites with the modified covariance matrices ($\chi_r^2{}_1$), originally reported covariance matrices ($\chi_r^2{}_2$) and using 21 GNSS close to the MMF with the modified covariance matrices ($\chi_r^2{}_3$). (cont.)

No	E	D	C	B	$\chi_r^2{}_1$	$\chi_r^2{}_2$	$\chi_r^2{}_3$
79	10	5	10	10	6.42	26.5	7.94
80	10	0	10	10	6.43	26.5	7.99
81	10	10	10	10	6.49	26.9	8.1

Table C.2. The comparison of χ_r^2 misfits for the 7 best models from the grid search of locking depths of Marmara Sea segments B to E in Figure 5.3c and 36 additional models with a 2.5 km grid size for segments C to E around the best-fitting models using all available 76 GNSS stations with the modified covariance matrices ($\chi_r^2{}_1$), originally reported covariance matrices ($\chi_r^2{}_2$) and using 21 GNSS close to the MMF with the modified covariance matrices ($\chi_r^2{}_3$).

No	F	E	D	C	B	A	$\chi_r^2{}_1$	$\chi_r^2{}_2$	$\chi_r^2{}_3$
1	7.5	0	10	2.5	5	7.5	5.27	18.9	4.4
2	7.5	0	10	0	5	7.5	5.27	18.9	4.41
3	7.5	0	10	5	5	7.5	5.28	18.9	4.42
4	7.5	2.5	10	2.5	5	7.5	5.28	19.1	4.44
5	7.5	2.5	10	0	5	7.5	5.28	19.1	4.45
6	7.5	0	7.5	2.5	5	7.5	5.29	19	4.5
7	7.5	0	7.5	0	5	7.5	5.29	19	4.51
8	7.5	0	12.5	0	5	7.5	5.29	19	4.44
9	7.5	0	12.5	2.5	5	7.5	5.29	19	4.44
10	7.5	0	7.5	5	5	7.5	5.29	19	4.49
11	7.5	2.5	10	5	5	7.5	5.29	19.1	4.45
12	7.5	2.5	7.5	2.5	5	7.5	5.29	19.2	4.53
13	7.5	2.5	7.5	0	5	7.5	5.3	19.2	4.54
14	7.5	2.5	7.5	5	5	7.5	5.3	19.1	4.52
15	7.5	2.5	12.5	0	5	7.5	5.3	19.2	4.49
16	7.5	2.5	12.5	2.5	5	7.5	5.3	19.2	4.48

Table C.2. The comparison of χ_r^2 misfits for the 7 best models from the grid search of locking depths of Marmara Sea segments B to E in Figure 5.3c and 36 additional models with a 2.5 km grid size for segments C to E around the best-fitting models using all available 76 GNSS stations with the modified covariance matrices ($\chi_r^2{}_1$), originally reported covariance matrices ($\chi_r^2{}_2$) and using 21 GNSS close to the MMF with the modified covariance matrices ($\chi_r^2{}_3$). (cont.)

No	F	E	D	C	B	A	$\chi_r^2{}_1$	$\chi_r^2{}_2$	$\chi_r^2{}_3$
17	7.5	0	12.5	5	5	7.5	5.31	19	4.47
18	5	0	10	5	5	7.5	5.31	18.4	4.36
19	7.5	2.5	12.5	5	5	7.5	5.32	19.2	4.52
20	5	0	7.5	2.5	5	7.5	5.32	18.5	4.45
21	7.5	5	10	0	5	7.5	5.32	19.5	4.6
22	7.5	5	10	5	5	7.5	5.33	19.5	4.61
23	7.5	0	5	5	5	7.5	5.34	19.2	4.7
24	7.5	0	5	0	5	7.5	5.34	19.2	4.75
25	7.5	0	7.5	2.5	2.5	7.5	5.36	19.3	4.65
26	10	0	10	5	5	7.5	5.37	19.8	4.53
27	10	0	7.5	2.5	5	7.5	5.38	19.9	4.61
28	7.5	0	10	10	5	7.5	5.4	19.3	4.76
29	7.5	0	7.5	2.5	7.5	7.5	5.53	20.6	5.35
30	7.5	0	10	5	5	5	5.54	20	5.71
31	7.5	0	7.5	2.5	5	5	5.56	20.1	5.81
32	7.5	0	10	7.5	7.5	7.5	5.58	20.6	5.39
33	5	5	5	5	5	5	5.67	20.3	6.05
34	7.5	7.5	7.5	7.5	7.5	7.5	5.78	22.6	6.11
35	7.5	0	7.5	2.5	5	10	6.09	22.3	3.85
36	7.5	0	10	5	5	10	6.09	22.2	3.77
37	10	10	10	10	10	10	7.85	33.4	8.41
38	2.5	2.5	2.5	2.5	2.5	2.5	9.15	33.3	8.59
39	12.5	12.5	12.5	12.5	12.5	12.5	10.5	46.3	11.4
40	15	15	15	15	15	15	13.2	59.1	14.4
41	0	0	0	0	0	0	14.8	47.2	9.96
42	17.5	17.5	17.5	17.5	17.5	17.5	15.6	70.4	17.3
43	20	20	20	20	20	20	18	81.1	19.9

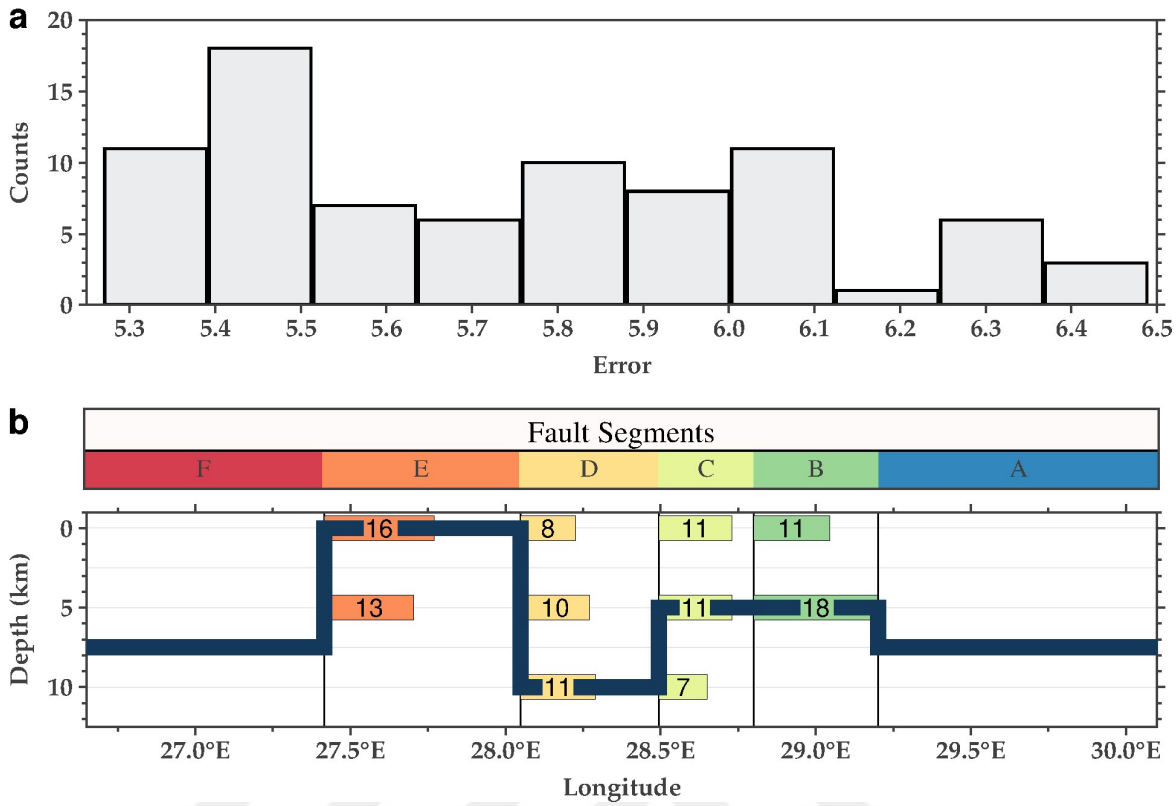

Figure C.1. (a) Histogram distribution of χ_r^2 misfits from the locking depth grid search for the Marmara Sea segments B to E in Figure 5.3c based on all 76 GNSS sites in the Marmara region with covariance matrices multiplied by 2.45 for continuous ones. (b) The distribution of locking depths for 29 accepted $\chi_r^2 \leq 5.5$ models, represented by bars of the same color as the relevant segments, and the best-fitting locking depth for each section, shown by a thick navy line.

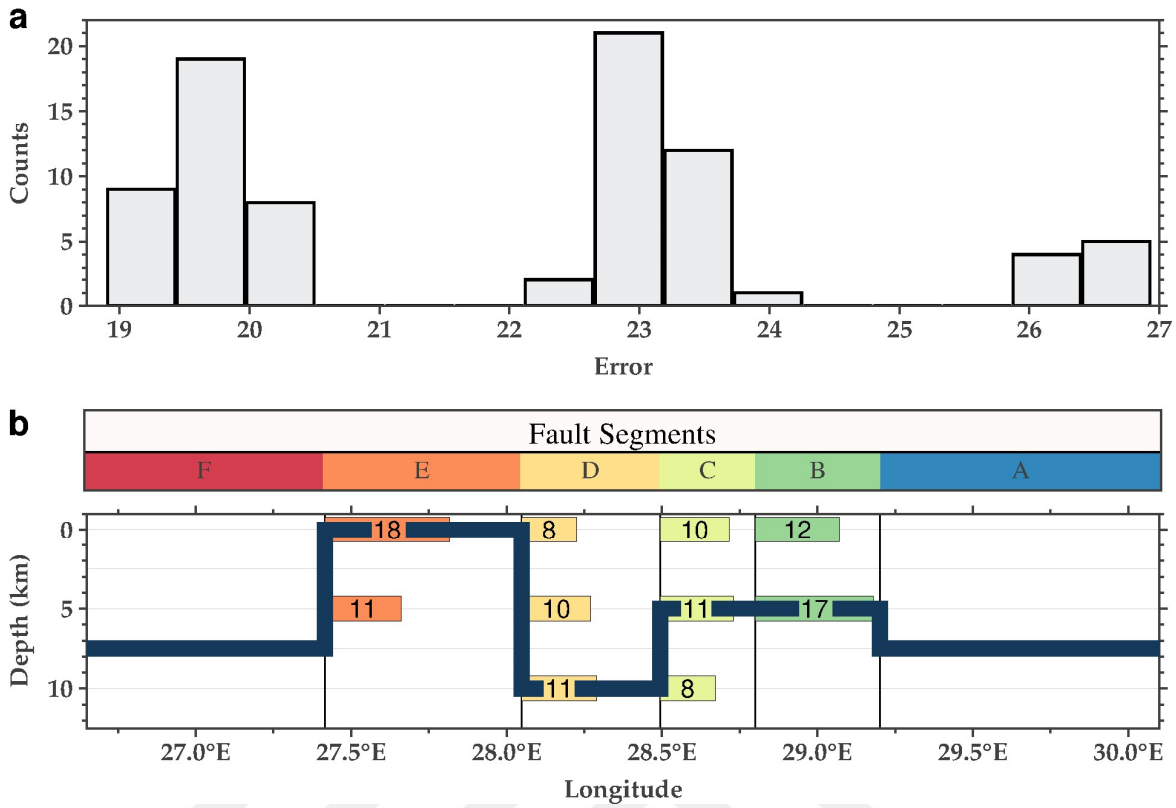

Figure C.2. (a) Histogram distribution of χ_r^2 misfits from the locking depth grid search for the Marmara Sea segments B to E in Figure 5.3c based on all 76 GNSS sites in the Marmara region. (b) The distribution of locking depths for 29 accepted $\chi_r^2 \leq 20$ models, represented by bars of the same color as the relevant segments, and the best-fitting locking depth for each section, shown by a thick navy line.